



Photodegradation Processes in Active Layer Materials for Organic Solar Cells

From Fundamental Understanding to Mitigation Guidelines

Suraj Prasad

Faculty of Health, Science and Technology

Physics

DOCTORAL THESIS | Karlstad University Studies | 2026:19

Photodegradation Processes in Active Layer Materials for Organic Solar Cells

From Fundamental Understanding to Mitigation Guidelines

Suraj Prasad

Photodegradation Processes in Active Layer Materials for Organic Solar Cells - From Fundamental Understanding to Mitigation Guidelines

Suraj Prasad

DOCTORAL THESIS

Karlstad University Studies | 2026:19

urn:nbn:se:kau:diva-108929

ISSN 1403-8099

ISBN 978-91-7867-684-2 (print)

ISBN 978-91-7867-685-9 (pdf)

<https://doi.org/10.59217/uax3063>

© The author

Distribution:
Karlstad University
Faculty of Health, Science and Technology
Department of Engineering and Physics
SE-651 88 Karlstad, Sweden
+46 54 700 10 00

Print: Universitetstryckeriet, Karlstad 2026

Fall in love with some activity, and do it! Nobody ever figures out what life is all about, and it doesn't matter. Explore the world. Nearly everything is really interesting if you go into it deeply enough. Work as hard and as much as you want to on the things you like to do the best. Don't think about what you want to be, but what you want to do. Keep up some kind of a minimum with other things so that society doesn't stop you from doing anything at all.

~Richard P. Feynman

Abstract

Organic solar cells (OSCs) have achieved a record power conversion efficiency (PCE) of over 20%. However, ensuring their long-term operational stability remains a significant challenge for commercial production. In this thesis, we used a combination of spectroscopy and microscopy techniques, including UV-vis absorption spectroscopy, Fourier-transform infrared (FTIR) spectroscopy, photoluminescence (PL) spectroscopy, atomic force microscopy (AFM), synchrotron-based X-ray and ultraviolet photoelectron spectroscopy (XPS and UPS), and near-edge X-ray absorption fine structure (NEXAFS) spectroscopy, to investigate degradation products formed in the photoactive layer upon exposure to AM 1.5 light in air. We also studied the degradation of the electrical performance of OSC devices by J-V, EQE, and photo-CELIV.

The first part of this thesis investigates the photodegradation mechanism of state-of-the-art photoactive materials used in OSCs. Thin films of PBDB-T, Y5, PF5-Y5, and PYT were intentionally degraded under AM 1.5 illumination in air. The results indicate that the BDT-T unit in PBDB-T and PF5-Y5 accelerates photobleaching, whereas its replacement with thiophene significantly improves the photostability of PYT. Further studies on PM6 and Y6, both as neat films and in blends, revealed distinct degradation pathways under controlled illumination. By employing long-wavelength band-pass filter illumination that selectively excites the acceptor, electron-transfer-induced superoxide formation was suppressed, and remaining degradation occurs due to singlet oxygen via energy transfer.

The second part focuses on the effect of photodegradation on the photovoltaic performance of OSCs. The effect of processing solvents (chloroform and chlorobenzene) on the morphology of the active layer and on the performance and stability of PM6:Y6 OSCs was examined. AFM images show that chlorobenzene-processed films exhibit higher surface roughness. NEXAFS spectroscopy further reveals that Y6 adopts a random orientation in chlorobenzene-processed PM6:Y6

blends, whereas chloroform processing induces a preferential face-on molecular orientation. Despite these morphological differences, device performance degrades at similar rates. Finally, incorporating 20 vol% PC₇₀BM into PTQ10:Y6 blends reduces the formation rate of new carbonyl groups and improves photostability, decreasing efficiency loss from 82% of the original efficiency in binary devices to 74% in ternary devices after 80 minutes of continuous AM 1.5 illumination in air.

Overall, this work provides insights into molecular- and device-level degradation pathways in high-performance OSC systems and identifies structural and compositional strategies to mitigate photooxidation processes. The findings contribute to the fundamental understanding needed to improve the long-term operational stability of OSCs.

Keywords: Organic solar cells, non-fullerene acceptor, conjugated polymer, photodegradation, photostability, electron transfer, energy transfer, molecular orientation

Sammanfattning

Organiska solceller (OSC) har uppnått rekordhöga verkningsgrader (PCE) på över 20 %. Att säkerställa deras långsiktiga stabilitet under drift är dock fortfarande en utmaning och en nödvändighet för kommersiell produktion. I denna avhandling har en kombination av spektroskopi- och mikroskopitekniker används, bland annat UV-vis absorptionsspektroskopi, Fourier-transform infrarödspektroskopi (FTIR), fotoluminescensspektroskopi (PL), atomkraftsmikroskopi (AFM), synkrotronbaserad röntgen- och ultraviolet fotoelektron-spektroskopi (XPS och UPS) samt röntgenabsorptionsspektroskopi (NEXAFS), för att undersöka vilka nedbrytningsprodukter som bildas i det fotoaktiva lagret efter belysning med AM 1.5-ljus i luft. Vi studerade även degradering av den elektriska prestandan hos organiska solceller med hjälp av J-V-mätningar, EQE och foto-CELIV.

Den första delen i avhandlingen behandlar nedbrytningsmekanismerna under belysning hos några fotoaktiva material som används i högeffektiva OSC. Tunna filmer av PBDB-T, Y5, PF5-Y5 och PYT degraderades avsiktligt under AM 1.5-belysning i luft. Resultaten visar att BDT-T-enheten i PBDB-T och PF5-Y5 påskyndar fotoblekning, medan ersättning av denna enhet med tiofen förbättrar fotostabiliteten hos PYT avsevärt. Ytterligare studier av PM6 och Y6, både som rena filmer och i blandningar, påvisade distinkta nedbrytningsvägar under kontrollerad belysning. Genom att använda bandpassfilter för ljus med långa våglängder som selektivt exciterar acceptorn undertrycktes nedbrytningen genom elektronöverföring och bildning av en superoxid, och kunde generering av singlet-syre via energiöverföring identifieras som den dominerande nedbrytningsmekanismen.

Den andra delen fokuserar på hur nedbrytning under belysning påverkar den fotovoltaiska prestandan hos OSC. Vi undersökte effekten som valet av lösningsmedel (kloroform och klorbensen) för tillverkning har på det aktiva lagrets morfologi samt på prestanda och stabilitet hos PM6:Y6 OSC. AFM-bilder visar att

klorbensenprocessade filmer uppvisar en råare yta. NEXAFS-spektroskopi visar dessutom att Y6 antar en slumpmässig orientering i klorbensenprocessade PM6:Y6 filmer, medan tillverkning från kloroformlösning inducerar en preferentiell face-on orientering av Y6. Trots dessa morfologiska skillnader bryts enheternas prestanda ner i liknande takt. Slutligen minskar en tillsats av 20 vol% PC₇₀BM i PTQ10:Y6-blandningar bildningshastigheten av nya karbonylgrupper och förbättrar fotostabiliteten. Detta reducerar förlusten i verkningsgrad från 82 % av den ursprungliga värdet för den binära blandningen till 74 % för den ternära blandningen efter 80 minuters kontinuerlig AM 1.5-belysning i luft.

Sammanfattningsvis ger det här arbete insikter i molekylära och solcellsrelaterade nedbrytningsprocesser i högpresterande OSC-system och identifierar strukturella och materialkemiska strategier för att motverka fotooxidationsprocesser. Resultaten bidrar till den grundläggande förståelse som krävs för att förbättra den långsiktiga driftsstabiliteten hos organiska solceller.

Nyckelord: Organiska solceller, icke-fullerenacceptor, konjugerad polymer, fotodegradering, fotostabilitet, elektronöverföring, energiöverföring, molekylorientering

Acknowledgments

I would like to express my sincere and heartfelt gratitude to my main supervisor, Ellen Moons, who introduced me to the fascinating field of organic photovoltaics and helped me appreciate the beauty of the underlying physics. Her guidance, encouragement, and support have been invaluable throughout my PhD journey, especially during challenging times. I am deeply grateful for the trust and freedom she gave me to explore different research directions and develop my own ideas. I greatly appreciate her patience, the time she generously devoted to discussions, and her willingness to listen and help me overcome research challenges. Her support has played a crucial role in shaping both my research and my personal growth. I am also sincerely thankful to my co-supervisor, Moyses Araujo, for his consistent support and for the many constructive discussions that helped refine my ideas and move the work forward. His thoughtful feedback and willingness to engage with details have been invaluable during my PhD journey. I consider myself fortunate to have supervisors with immense positive energy who provided continuous motivation throughout my candidature, and I am deeply grateful to them.

I would also like to thank my current and former PhD examiners, Hanmin Zhang and Lars Johansson, for your support and guidance. It has always been a pleasure to discuss science with you, and I will carry that inspiration with me throughout my research career.

I would also like to thank Leif Ericsson for his continuous support and for the many valuable discussions throughout my projects. I cannot fully express how much your guidance has meant to me throughout my PhD journey. I am especially grateful for the significant time you spent with me in the laboratory, teaching me various experimental techniques and broadening my understanding through discussions on a wide range of scientific topics. I would like to thank Cleber Marchiori for his scientific support and insightful discussions. I am also grateful to Jan van Stam and Andrea Muntean for the nice discussions during the meeting and

for reviewing my thesis. I would like to thank Patricia Mendez and Mikael Andersén for their support and contributions during this period.

I would like to thank my collaborators, Ergang Wang and Zewdneh Genene at Chalmers University of Technology, Sweden, for providing the chemicals. I also thank Andreas Opitz at Humboldt University of Berlin, Germany, for his support with the synchrotron measurements. I am grateful to the synchrotron facilities and beamline scientists for their continuous support during day and night measurements: Stephan Appelfeller and Alexei Preobrajenski at the FlexPES beamline, MAX IV Laboratory, Lund, Sweden; and Ewa Partyka-Jankowska and Marcin Zając at the PIRX beamline, National Synchrotron Radiation Centre SOLARIS, Kraków, Poland, for their assistance with the UPS, XPS, and NEXAFS measurements.

Many thanks also go to my current and former lab SOLA members at Karlstad University: Saurabh, Ishita, Leticia, André, Shahna, Asirin, Mateus, Symon, Shivam, Leandro, Paulo, and Paweł for their help in the lab. I am also grateful to my colleagues, Seema, Lorena, Majid, Ayush, Anutsek, Athulya, Christian, Andreas, Stefan, and others in the Department of Engineering and Physics for inspiring Fika discussions that provided intellectual and personal support.

I would like to thank Marcus Berg, Thijs Jan Holleboom, Markus Rinio, Krister Svensson, Mahdi Mohajeri, and Reza Sirjani for the teaching courses and for the opportunity to take on teaching duties. The teaching experience shaped my development in important ways, especially by strengthening my critical thinking and communication skills. I truly enjoyed teaching and sharing knowledge with students, and I also learned so much from them during those teaching days. I am grateful to Mikael Grehk, Daniel Johansson, Cecilia Kåwe, Elisabeth Wessling, Stina Røjder Berglund, Malin Ornstein, Malin Krokström, Leena Hagsmo, Carina Olsson, and Elena Kullinger for their support and assistance over these years.

During this time, I have made incredible friends: Ibbe, Sebastian, Freysteinn, and Johnnie, and I am grateful to be part of the FFFF group. I hope we will continue sharing food, laughter, and fun for a long time to come. I would like to thank my friends Rajan, Laxmi, Rashik, Sudiksha, Sokkalingam, Faizan, Surendra, Vishnu, and my Swedish friends for organizing all the events during this time.

Beyond my studies, I discovered the joy of sports and outdoor activities. Sports have become an important and meaningful part of my life, and I did not realize how much I would enjoy them until I started. I would also like to acknowledge my swimming teacher, who taught me how to swim, a skill that has given me great confidence and happiness, to the point that I can now stay in the water for hours. I am also grateful to my energetic friends from the badminton sessions at KAUIF for the great times and the welcoming atmosphere. I would like to thank Mihai Patrascu and Muse Merache for their enthusiasm and energy, which introduced me to the world of hiking. Exploring these passions with them has been one of the most rewarding experiences of my life, and I look forward to continuing these adventures for years to come.

Finally, I would like to express my heartfelt gratitude to my fiancée, Suman, for her love, encouragement, and unwavering support throughout this journey. I am deeply grateful to my family for their constant guidance and support over the years. This accomplishment would not have been possible without all of you. Thank you for being part of this journey and for making it possible.

Karlstad, Sweden, March 16th, 2026

Suraj Prasad

List of publications

The following papers are included in this thesis:

- I. Effect of molecular structure on the photochemical stability of acceptor and donor polymers used in organic solar cells.
Suraj Prasad, Zewdneh Genene, Cleber F. N. Marchiori, Shivam Singh, Leif K. E. Ericsson, Ergang Wang, C. Moyses Araujo, and Ellen Moons.
Materials Advances, 2024, 5, 7708–7720.
DOI: <https://doi.org/10.1039/D4MA00447G>

- II. Photostability of Y-type electron acceptor molecules and related copolymer.
Suraj Prasad, Zewdneh Genene, Cleber F. N. Marchiori, Leif K. E. Ericsson, Ergang Wang, C. Moyses Araujo, and Ellen Moons.
Proc. SPIE 12660, Organic, Hybrid, and Perovskite Photovoltaics XXIV, 1266002 (1 October 2023).
DOI: <https://doi.org/10.1117/12.2679517>

- III. The role of the donor in the light-induced degradation of Y6 non-fullerene acceptors in PM6:Y6 blend films.
Suraj Prasad, C. Moyses Araujo, and Ellen Moons.
Journal of Materials Chemistry C, 2026,14, 3954-3965
DOI: <https://doi.org/10.1039/D5TC03779D>

- IV. Effect of solvent on the light-induced degradation in air of PM6:Y6 blend films and solar cells.
Suraj Prasad, C. Moyses Araujo, and Ellen Moons.
Submitted to Materials Advances

- V. The photostability of PTQ10:Y6 organic solar cells and the impact of added PC₇₀BM.
Suraj Prasad, C. Moyses Araujo, and Ellen Moons. (Manuscript)

My contribution to the publications

- I. I carried out all the experimental work, including sample preparation and UV-vis, FTIR, and AFM measurements. I also participated in X-ray and ultraviolet photoelectron spectroscopy measurements at the in-house facility and analyzed the results in discussion with the co-authors. I was responsible for writing the first draft of the manuscript and contributed to its revision and finalization.
- II. I carried out all the experimental work, including sample preparation and UV-vis and FTIR measurements. I also participated in X-ray photoelectron spectroscopy measurements at the in-house facility, analyzed the results in discussion with the co-authors, and contributed to the revision and finalization of the manuscript.
- III. I carried out all the experimental work, including sample preparation and UV-vis, FTIR, and AFM measurements, participated as part of the team in X-ray and Ultraviolet Photoelectron Spectroscopy at the synchrotron facility at Max IV Laboratory in Sweden, and analyzed the results in discussion with coauthors. I was responsible for writing the first draft of the manuscript and contributed to its revision and finalization.
- IV. I carried out all the experimental work, including sample preparation, device fabrication, and UV-vis, FTIR, and AFM measurements, participated as part of the team in Near Edge X-Ray Absorption Fine Structure Spectroscopy at the synchrotron facility at Max IV Laboratory in Sweden and at SOLARIS in Poland, and analyzed the results in discussion with coauthors. I was responsible for writing the first draft of the manuscript and contributed to its revision and finalization.
- V. I carried out all the experimental work, including sample preparation, device fabrication, and UV-vis, FTIR, and AFM measurements, analyzed the results in discussion with coauthors, and was responsible for writing the first draft of the manuscript and contributed to its revision and finalization.

List of Figures

- Figure 1.1: Energy consumption pie chart by energy source.
- Figure 1.2: Block diagram of different generations of solar cells.
- Figure 1.3: The record efficiency chart for best photovoltaics from the National Renewable Energy Laboratory (NREL).
- Figure 1.4: Schematic of OSC illustrating some of the degradation processes.
- Figure 2.1: The sp , sp^2 , and sp^3 hybrid orbitals.
- Figure 2.2: Formation of σ and π in sp^2 hybridization for the ethene molecule.
- Figure 2.3: Schematic representation of the electronic structure of a sp^2 hybridized orbital.
- Figure 2.4: Schematic representation of electron transfer and energy transfer processes in the donor-acceptor blend, illustrating the formation of superoxide radicals (O_2^-) and singlet oxygen (1O_2).
- Figure 3.1: The two different device architectures (a) conventional and (b) inverted.
- Figure 3.2: The different processes involved during the operation of organic solar cells (a) photon absorption, (b) exciton diffusion and charge transfer state formation, (c) charge separation, and (d) charge transport and collection, as well as the loss mechanisms (e-g) based on photogenerated charge carriers.
- Figure 3.3: Jablonski diagram for an organic molecule with different electronic levels, S_0 , S_1 , S_2 , and T_1 . The S_0 is the ground state, S_1 and S_2 are the first and second excited states, and T_1 is the triplet state. The arrow indicates the absorption and recombination processes.
- Figure 3.4: Schematic of the energy level diagram from the exciton formation to the charge separation state. Here, S_0 and S_1 are the ground state and first excited state. The symbol k represents the rate constant for processes such as LE (local exciton), CT (charge transfer), and CS (charge separation), and ΔG is the Gibbs energy.
- Figure 3.5: The device configurations of organic photovoltaic cells.

- Figure 3.6: The current-voltage characteristics of the solar cell under dark and illuminated conditions, where J_{SC} is the short-circuit density, V_{OC} is the open-circuit voltage, J_{mpp} is the current density, and V_{mpp} is the voltage at the maximum power point.
- Figure 3.7: Schematic representation of a lifetime chart for the stability of organic solar cells.
- Figure 4.1: Molecular structure of PBDB-T.
- Figure 4.2: Molecular structure of PM6.
- Figure 4.3: Molecular structure of PTQ10.
- Figure 4.4: Molecular structure of Y5.
- Figure 4.5: Molecular structure of Y6.
- Figure 4.6: Molecular structure of PF5-Y5.
- Figure 4.7: Molecular structure of PYT.
- Figure 4.8: The process of spin coating (a) solution deposition, (b) thinning, (c) drying, and (d) thin film deposited.
- Figure 4.9: The electronic transitions from the ground state to the higher excited state (left). The absorption spectrum of PBDB-T and PF5-Y5 (right). The symbol represents the ground state σ , π as bonding orbitals, n as non-bonding orbitals, and the excited state σ^* , π^* as antibonding orbitals.
- Figure 4.10: Schematic illustration of the ultraviolet-visible absorption spectrometer.
- Figure 4.11: Illustration of different modes of vibration for a triatomic molecule: (a) Stretching modes, (b) in-plane modes, and (c) out-of-plane modes.
- Figure 4.12: Schematic of FTIR spectrometer.
- Figure 4.13: Schematic of AFM setup.
- Figure 4.14: Lennard-Jones potential curve. There are several different types of modes being used in AFM: contact mode, intermittent contact/tapping mode, and non-contact mode.
- Figure 4.15: Schematic of the photoluminescence measurement system.
- Figure 4.16: Schematic layout of a synchrotron and highlights several key components. Electrons are first generated and subsequently

accelerated before being injected into the storage ring. As the electrons circulate, synchrotron radiation is produced whenever their trajectory is deflected, either by bending magnets or by dedicated insertion devices installed in the straight sections of the ring.

- Figure 4.17: Schematic of UPS and XPS process.
- Figure 4.18: Schematic representation of the XPS system and the C 1s spectra of PF5-Y5.
- Figure 4.19: Schematic illustration of the molecular energy levels and the transitions from core levels into antibonding and continuum states. The corresponding NEXAFS spectrum arising from these transitions is shown on the right-hand side of the figure.
- Figure 4.20: Schematic of the different NEXAFS measurement techniques in different modes.
- Figure 4.21: Angular dependent NEXAFS spectra at the carbon K-edge of a PF5-Y5 film processed from chlorobenzene solutions. The angle given in the legend is the angle of incidence of the X-ray with respect to the sample surface.
- Figure 4.22: C1s NEXAFS spectra in TEY mode of TQ1, N2200, and TQ1:N2200 (2:1) films after different photodegradation times in air (0 min, 30 min, 2 hr, and 11 hr).
- Figure 4.23: The sample holder with spin-coated thin films of PM6:Y6 on a Si/SiOX substrate for NEXAFS measurements done at the FlexPES beamline at MAXIV, Lund.
- Figure 4.24: Schematic representation of the conventional device architecture of an organic solar cell.
- Figure 4.25: Schematic of the fabricated device inside a quartz-window device holder.
- Figure 4.26: Equivalent circuit diagram of the solar cell under illumination, represented by a single-diode model including both series and shunt resistances.
- Figure 4.27: Schematic of the illuminated J–V measurement setup for organic solar cells under a solar simulator.

- Figure 4.28: Schematic of external quantum efficiency setup.
- Figure 4.29: Schematic representation of the Photo-CELIV measurement, adapted from PAIOS (Fluxim).
- Figure 5.1: The graphical summary of papers I and II.
- Figure 5.2: The graphical summary of paper III.
- Figure 5.3: The graphical summary of paper IV.
- Figure 5.4: The graphical summary of paper V.

List of abbreviations and acronyms

AFM	Atomic force microscopy
AM 1.5	Air mass 1.5 spectrum
BHJ	Bulk heterojunction
CdTe	Cadmium telluride
CIGS	Copper indium gallium selenide
CS	Charge separation
CT	Charge transfer
D/A	Donor/Acceptor
D18	Poly[(2,6-(4,8-bis(5-(2-ethylhexyl-3-fluoro)thiophen-2-yl)-benzo[1,2-b:4,5-b']dithiophene))-alt-5,5'-(5,8-bis(4-(2-butyl-octyl)thiophen-2-yl)dithieno[3',2':3,4;2'',3'':5,6]benzo[1,2-c][1,2,5]thiadiazole)]
DF-PCIC	2,2'-((2Z,2'Z)-(((2,5-difluoro-1,4-phenylene)bis(4,4-bis(2-ethylhexyl)-4H-cyclopenta[2,1-b:3,4-b']dithiophene-6,2-diyl))bis(methanylylidene))bis(3-oxo-2,3-dihydro-1H-indene-2,1-diylidene))dimalononitrile
EQE	External quantum efficiency
ETL	Electron transport layer
FF	Fill factor
FTIR	Fourier transform infrared
HOMO	Highest occupied molecular orbital
HTL	Hole transport layer
IDTBR	(5Z,5'Z)-5,5'-((7,7'-(4,4,9,9-tetraoctyl-4,9-dihydro-s-indaceno[1,2-b:5,6-b']dithiophene-2,7 diyl)bis(benzo[c][1,2,5]thiadiazole-7,4-diyl))bis(methanylylidene))bis(3-ethyl-2-thioxothiazolidin-4-one)
IT-4F	3,9-bis(2-methylene-((3-(1,1-dicyanomethylene)-6,7-difluoro)-indanone))-5,5,11,11-tetrakis(4-hexylphenyl)-dithieno[2,3-d:2',3'-d']-s-indaceno[1,2-b:5,6-b']dithiophene

ITIC	3,9-bis(2-methylene-(3-(1,1-dicyanomethylene)-indanone))-5,5,11,11-tetrakis(4-hexylphenyl)-dithieno[2,3-d:2',3'-d']-s-indaceno[1,2-b:5,6-b']dithiophene
ITO	Indium tin oxide
J _{sc}	Short-circuit current density
LBL	Layer by layer
LE	Local exciton
LUMO	Lowest unoccupied molecular orbital
NEXAFS	Near-Edge X-ray Absorption Fine Structure
NFA	Non-fullerene acceptor
P3HT	Poly(3-hexylthiophene-2,5-diyl)
PBDB-T	Poly[(2,6-(4,8-bis(5-(2-ethylhexyl)thiophen-2-yl)-benzo[1,2-b:4,5-b']dithiophene))-alt-(5,5-(1',3'-di-2-thienyl-5',7'-bis(2-ethylhexyl)benzo[1',2'-c:4',5'-c']dithiophene-4,8-dione)]
PDINO	3,3'-(1,3,8,10-Tetraoxoanthra[2,1,9-def:6,5,10-d'e'f']diisoquinoline-2,9(1H,3H,8H,10H)-diyl)bis(N,N-dimethylpropan-1-amine oxide)
PEDOT:PSS	Poly(3,4-ethylene dioxythiophene)/poly(styrene sulfonate)
PEI	Polyethylenimine
PEIE	Ethoxylated polyethylenimine
PF5-Y5	Poly[(2,2'-((2Z,2'Z)-((12,13-bis(2-ethylhexyl)-3,9-diundecyl-12,13dihydro[1,2,5]thiadiazolo[3,4e]thieno[2'',3'':4',5']thieno[2',3':4,5]pyrrolo[3,2-g]thieno[2',3':4,5]thieno[3,2-b]-indole-2,10-diyl)bis(methanylylidene))bis(3-oxo-2,3-dihydro-1H-indene-2,1-diylidene))dimalononitrile-alt-2,6-(4,8-bis(5-(2-ethylhexyl-3-hexyl)thiophen-2-yl)-benzo[1,2-b:4,5-b']dithiophene))]
PhotoCELIV	Photo Charge Extraction by Linearly Increasing Voltage
P _{inc}	Incident power
PM6	Poly[[4,8-bis[5-(2-ethylhexyl)-4-fluoro-2-thienyl]benzo[1,2-b:4,5-b']dithiophene-2,6-diyl]-2,5-thiophenediyl[5,7-bis(2-

	ethylhexyl)-4,8-dioxo-4H,8H-benzo[1,2-c:4,5-c']dithiophene-1,3-diyl]-2,5-thiophenediyl]
P_{\max}	Peak power
PSMA	Polymerized small molecule acceptor
PTQ10	Poly [[6,7-difluoro[(2-hexyldecyl)oxy]-5,8-quinoxalinediyl]-2,5-thiophenediyl]]
PYT	Poly[(2,2'-((2Z,2'Z)-((12,13-bis(2-octyldodecyl)-3,9-diundecyl-12,13dihydro[1,2,5]thiadiazolo[3,4e]thieno[2'',3'':4',5']thieno[2',3':4,5]pyrrolo[3,2-g]thieno[2',3':4,5]thieno[3,2-b]-indole-2,10-diyl)bis(methanylylidene))bis(3-oxo-2,3-dihydro-1H-indene-2,1-diylidene)) dimalononitrile-alt-2,5-thiophene)]
SMA	Small molecule acceptor
UPS	Ultraviolet photoelectron spectroscopy
V_{oc}	Open-circuit voltage
XPS	X-ray photoelectron spectroscopy
Y5	2,2'-((2Z,2'Z)-((12,13-bis(2-ethylhexyl)-3,9-diundecyl-12,13-dihydro[1,2,5]thiadiazolo[3,4e]thieno[2'',3'':4',5']thieno[2',3':4,5]pyrrolo[3,2-g]thieno[2',3':4,5]thieno[3,2-b]indole-2,10-diyl)bis(methanylylidene))bis(3-oxo-2,3-dihydro1H-indene-2,1-diylidene))dimalononitrile
Y6	2,2'-((2Z,2'Z)-((12,13-Bis(2-ethylhexyl)-3,9-diundecyl-12,13-dihydro-[1,2,5]thiadiazolo[3,4-e]thieno-[2'',3'':4',5']thieno[2',3':4,5]pyrrolo[3,2-g]thieno-[2',3':4,5]thieno[3,2-b]indole-2,10-diyl)bis(methanylylidene))-bis(5,6-difluoro-3-oxo-2,3-dihydro-1H-indene-2,1-diylidene))dimalononitrile

Contents

1. Introduction	1
1.1 Solar cells.....	2
1.2 Different types of solar cells.....	3
1.2.1 First-generation solar cell.....	5
1.2.2 Second-generation solar cell.....	5
1.2.3 Third-generation solar cell.....	6
1.3 Motivation.....	8
1.4 Outline of the thesis	9
2. Organic semiconductors	11
2.1 Conjugated molecules	12
2.2 Morphology	15
2.2.1 Photochemical stability.....	16
2.2.2 Morphological stability	21
3 Organic solar cells.....	23
3.1 Working principle	23
3.1.1 Photon absorption and Frenkel exciton formation	24
3.1.2 Exciton diffusion and CT state formation	25
3.1.3 Formation of charge separation state.....	26
3.1.4 Charge transport and collection.....	27
3.1.5 Recombination.....	28
3.2 Device configuration.....	30
3.2.1 Single-layer device configuration	30
3.2.2 Bilayer device configuration.....	31
3.2.3 Bulk heterojunction device configuration	31
3.3 Solar cell parameters.....	31
3.3.1 Open-circuit voltage (V_{oc}).....	32
3.3.2 Short-circuit current density (J_{sc}).....	33
3.3.3 Fill factor (FF).....	33
3.4 Stability and lifetime of OSCs.....	34
3.4.1 Light and oxygen.....	35
3.4.2 Interfacial instability.....	36
4 Materials and experimental techniques.....	38

4.1	Materials	38
4.1.1	Polymer PBDB-T donor.....	38
4.1.2	Polymer PM6 donor	39
4.1.3	Polymer PTQ10 donor.....	39
4.1.4	Small molecule acceptor Y5.....	40
4.1.5	Small molecule acceptor Y6.....	41
4.1.6	Polymer PF5-Y5 acceptor.....	41
4.1.7	Polymer PYT acceptor	42
4.2	Experimental techniques.....	43
4.2.1	Film preparation	43
4.2.2	Ultraviolet-visible-NIR absorption spectroscopy.....	44
4.2.3	Fourier Transform Infrared Spectroscopy	46
4.2.4	Atomic force microscopy.....	49
4.2.5	Photoluminescence Spectroscopy	51
4.2.6	Synchrotron radiation	52
4.2.7	Photoelectron spectroscopy	55
4.2.8	Near-Edge X-Ray Absorption Fine Structure (NEXAFS) spectroscopy	57
4.3	Device fabrication.....	62
4.3.1	Deposition of charge transport, active layer, and metal electrode.	63
4.4	Device characterization.....	65
4.4.1	I-V measurements	65
4.4.2	IPCE measurements	66
4.4.3	Photo-CELIV measurements.....	67
5.	Summary of papers.....	69
6.	Conclusions	74
7.	Outlook.....	76

Chapter 1

Introduction

Energy plays a crucial role in our modern society, influencing daily life, technological advancement, transportation systems, environmental sustainability, and the overall economic framework.¹⁻³ In a broader context, energy consumption primarily depends on two key factors: the global population and the global Gross Domestic Product.⁴ It is expected that the global population will surpass 9.8 billion by 2050 and reach approximately 11.2 billion by 2100.⁵ The current world's energy consumption is ~19 TW.⁴ Considering population growth and rising global energy demand, total energy consumption is expected to approximately double between 2020 and 2050.^{6,7} Fossil fuels, including coal, oil, and natural gas, remain the dominant sources of energy worldwide. Although many nations are reducing their coal use, oil and gas consumption continue to expand rapidly.⁸ However, reliance on these energy sources contributes significantly to carbon dioxide (CO₂) emissions and environmental degradation.⁹

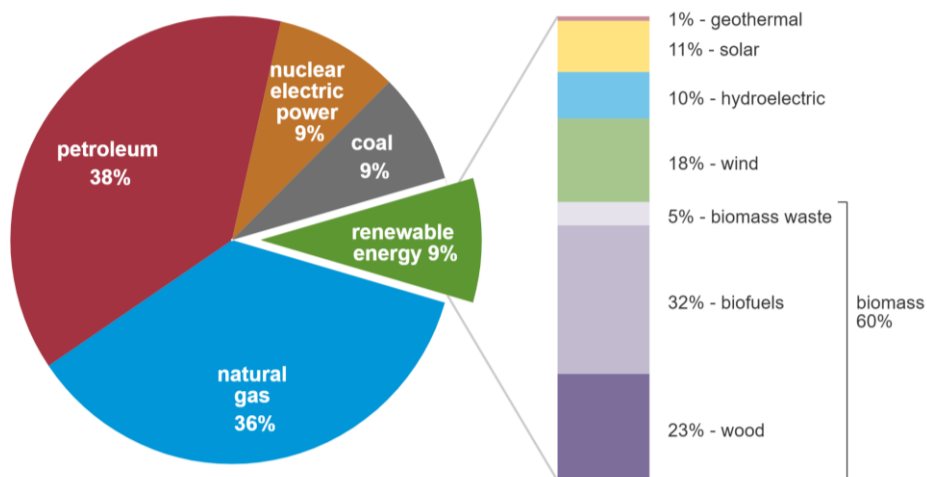


Figure 1.1: Energy consumption pie chart by energy source.¹⁰

According to the United Nations Environment Programme,¹¹ if this trend continues, planet-warming greenhouse gas emissions are expected to rise to 75

billion tonnes per year by 2050, leading to profound effects on daily life and environmental conditions, including human health, agricultural productivity, climate stability, global warming, ecosystem balance, and biodiversity.¹² Moreover, fossil fuels are finite resources, and their depletion poses a significant challenge to long-term energy security.¹³ In contrast, renewable energy serves as a sustainable alternative to conventional energy sources by harnessing natural resources such as solar, hydropower, geothermal, wind, and biomass to generate electricity, as illustrated in Figure 1.1.¹⁰ Energy generation from renewable sources is not only environmentally sustainable compared to fossil fuels but also provides a viable long-term solution for meeting global energy demands.¹⁴

Sunlight is a fundamental source of renewable energy that can be harvested both directly and indirectly. Overall, approximately 120,000 terawatts (TW) of solar radiation reach Earth's surface. It directly powers technologies such as solar water heaters and photovoltaic (PV) panels for electricity generation. Indirectly, solar radiation drives atmospheric circulation, creating wind that powers turbines for electricity generation. It also fuels the hydrological cycle by driving seawater evaporation, which leads to precipitation and downstream water flow, an essential process for hydroelectric power production. The flowing water turns turbines, converting kinetic energy into electrical energy and providing a renewable, sustainable power source. Additionally, sunlight enables plant growth through photosynthesis, which converts biomass into bioenergy, a renewable energy source. Developing efficient technologies to harness and convert sunlight into electricity could meet global energy demands well into the future.

1.1 Solar cells

The direct conversion of sunlight into electricity is achieved using solar cells, which operate based on the principle of the photoelectric effect observed by Heinrich Hertz.¹⁵ Edmond Becquerel demonstrated electricity generation when an electrolytic cell was exposed to light.¹⁶ In 1905, Albert Einstein provided a groundbreaking explanation of this phenomenon by introducing the concept of photons, thereby laying the theoretical foundation for quantum mechanics.¹⁷ For

this discovery, he was awarded the Nobel Prize in Physics in 1921.¹⁸ A major advancement in photovoltaic technology occurred at Bell Laboratories in 1954, with the development of the first silicon solar cell, which had a power conversion efficiency (PCE) of approximately 6%.¹⁹ Over a few decades, silicon PV technology has witnessed remarkable advancements, leading to improved efficiency, durability, and affordability. Among the various PV technologies, crystalline silicon (c-Si) modules have emerged as the most widely adopted and commercially dominant, holding the largest share of the global photovoltaic market.²⁰⁻²² The fabrication of Si-based photovoltaic modules requires substantial energy input and incurs high production costs. To address these limitations, various thin-film technologies have been developed, including amorphous silicon (a-Si:H),^{23,24} cadmium telluride (CdTe),^{25,26} copper indium gallium selenide (CIGS),^{27,28} dye-sensitized solar cells (DSSCs),^{29,30} perovskite solar cells (PSCs),^{31,32} and organic solar cells (OSCs).³³⁻³⁵ These technologies have attracted significant attention in the photovoltaic research and industrial sectors due to their potential to reduce costs, enable greater material flexibility, and enhance photovoltaic performance.³⁶⁻³⁸ A detailed discussion of the different generations of solar cells is presented in the subsequent section.

1.2 Different types of solar cells

The different generations of solar cells are shown in Figure 1.2.

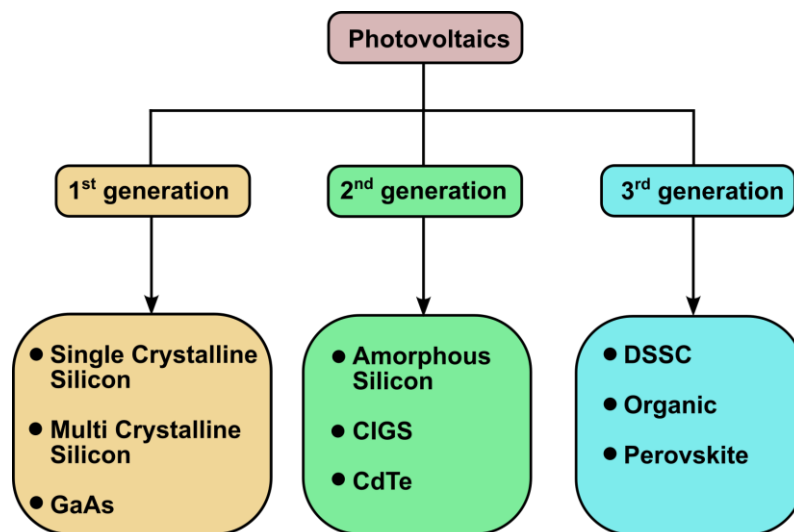


Figure 1.2: Block diagram of different generations of solar cells.

Best Research-Cell Efficiencies

NATIONAL LABORATORY OF THE ROCKIES

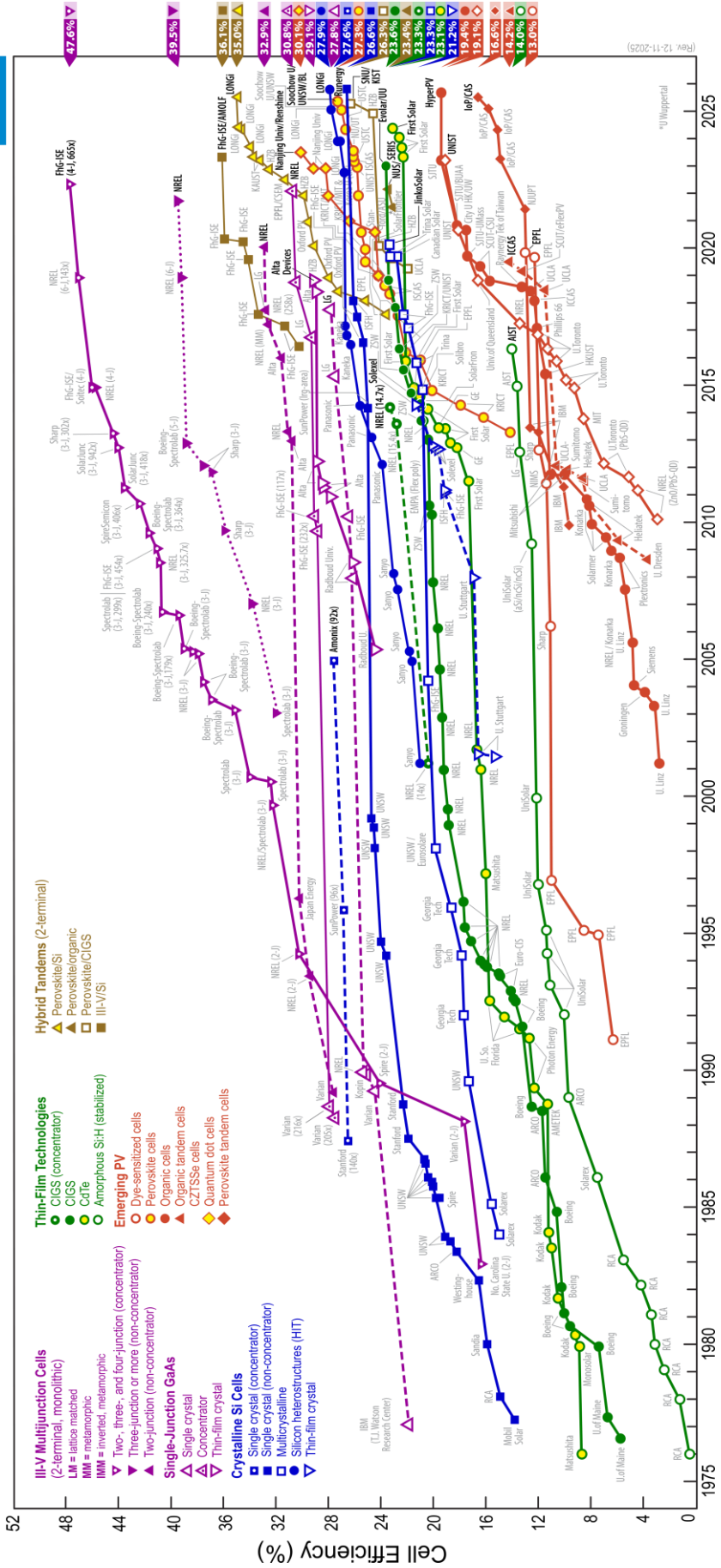


Figure 1.3: The record efficiency chart for best photovoltaics from the National Renewable Energy Laboratory (NREL).

1.2.1 First-generation solar cell

First-generation solar cells are characterized by inorganic crystalline semiconductor materials that are mechanically self-supporting. This category includes single-crystalline silicon, multi-crystalline silicon, and gallium arsenide (GaAs). According to the National Renewable Energy Laboratory (NREL) efficiency chart,³⁹ the current record PCEs for crystalline silicon (single-crystal, non-concentrator) and multi-crystalline silicon are 26.6% and 23.3%, respectively (Figure 1.3). For GaAs (single-crystal), a direct-bandgap semiconductor, the reported record PCE for a single-junction solar cell has reached 27.8% to date. This value, together with the one for the silicon heterojunction cell (HIT), also 27.9%, is the highest reported efficiency for a single-junction solar cell. These types of solar cells are widely utilized due to their high efficiency and long operational lifetime. However, their high production costs and substantial energy requirements during manufacturing result in longer energy payback periods, posing a significant limitation to their large-scale adoption.^{40,41}

1.2.2 Second-generation solar cell

Second-generation solar cells are based on thin-film technology, which offers significant reductions in production costs and material consumption compared to first-generation solar cells.^{41,42} The semiconductor layers in these solar cells are substantially thinner, typically 10 to 100 times thinner than those in crystalline silicon-based cells. According to recent NREL data, the record PCEs for thin-film solar cells based on amorphous silicon (a-Si:H), cadmium telluride (CdTe), and copper indium gallium selenide (CIGS) are 14%, 23.1%, and 23.6%, respectively (Figure 1.3). The fabrication of second-generation solar cells is relatively straightforward and employs techniques such as co-evaporation, spray pyrolysis, and sputtering.⁴³ However, these technologies face challenges related to material instability, toxicity, and comparatively longer energy payback times than first-generation solar cells.⁴⁴ Consequently, extensive research efforts have been directed towards improving device architecture, developing novel materials, and optimizing material composition to overcome these limitations and enhance overall performance.

1.2.3 Third-generation solar cell

Third-generation solar cells are primarily based on advanced thin-film technologies, including dye-sensitized solar cells (DSSCs), perovskite solar cells (PSCs), and organic solar cells (OSCs).⁴⁵ These technologies are designed to simplify the fabrication process and reduce the solar cell production costs per watt of generated power.^{45,46} DSSCs typically consist of a transparent electrode, a nanoporous titanium dioxide layer, a light-absorbing dye, an electrolyte, and a platinum counter electrode. When sunlight is absorbed by the dye molecules, photogenerated electrons are injected into the conduction band of the titanium dioxide (TiO_2). These electrons travel through the semiconductor to the transparent electrode and subsequently flow through an external circuit to the counter electrode, generating current. The electrolyte restores the oxidized dye molecules by donating electrons and is itself reduced at the platinum counter electrode by the returning electrons from the external circuit, completing the electrochemical cycle.²⁹ The first high-efficiency DSSC, developed by Brian O'Regan and Michael Grätzel in 1991, achieved a PCE of 7%.³⁰ Although DSSCs initially demonstrated promising performance, their current record PCE stands at approximately 13%, which remains lower than that of first- and second-generation solar cells and also lower than PSCs and OSCs.²⁹ Furthermore, their instability under prolonged illumination has limited large-scale commercialization. Over the past decade, PSCs have undergone rapid technological advancement, achieving certified power PCE of 27.3% for single-junction architectures (Figure 1.3).⁴⁷ These devices employ hybrid inorganic-organic lead halide materials with the ABX_3 perovskite crystal structure as light absorbers, where A represents the organic molecule, B represents the inorganic element, and X represents the halide element. Owing to their high absorption coefficients, long diffusion lengths, low exciton binding energies, high charge carrier mobilities, and ambipolar charge transport properties, perovskites are considered highly promising materials for photovoltaic applications.^{31,37} Additionally, their fabrication via a low-temperature *solution processing technique* offers cost and scalability advantages. Nonetheless, challenges such as lead toxicity, morphological control, the use of toxic solvents, and material and device instability continue to hinder their commercial deployment.⁴⁸

OSCs have attracted considerable attention from researchers due to several advantageous properties, including ease of fabrication, mechanical flexibility, lightweight structure, and large-area manufacturability.^{33,49} Recently, OSCs have achieved certified record PCEs of 19.4% for single-junction devices and 14.2% for tandem configurations (Figure 1.3).^{50,51} Several companies, such as Infinity PV and Epishine, are actively developing solution-processed roll-to-roll (R2R) printed organic photovoltaic technologies.^{52,53} Notably, Heliatek recently installed the world's largest organic photovoltaic (OPV) panels at the Simmering power plant in Vienna, demonstrating the potential of OSCs for real-world energy generation.⁵⁴ However, despite these advances, OSCs have not yet achieved widespread commercial adoption.^{55,56} While crystalline silicon solar panels typically exhibit lifespans of 25-30 years, the operational stability of OSCs remains limited to only a few years.^{20,57-61} This limitation continues to drive intensive research aimed at enhancing the durability, stability, and long-term performance of OSCs.

OSCs are primarily composed of a photoactive layer containing electron-donor and electron-acceptor materials that absorb light, along with charge-transport layers and electrodes. For high-efficiency OSCs, the most widely used materials are the donor polymers PBDB-T,⁶² PM6,⁶³ D18,⁶⁴ PTQ10,⁶⁵ and the non-fullerene acceptor (NFA) families IDTBR,⁶⁶ ITIC,⁶⁷ and the so-called Y-series⁶⁸. The long-term durability and operational stability of OSCs are governed by both intrinsic material properties and extrinsic environmental stress. Intrinsic degradation typically results from interfacial reactions between different layers, while extrinsic degradation is primarily caused by exposure to environmental stressors such as irradiation, moisture ingress, oxygen, and heat, as illustrated in Figure 1.4.^{34,67,69,70} Several degradation mechanisms can affect the photoactive layer of OSCs, including photo-induced degradation, photochemical degradation, thermal degradation, moisture and oxygen sensitivity, morphological degradation, interface degradation, and UV-induced degradation, ultimately leading to performance degradation.^{34,71-74}

For example, the most used electrodes are aluminum (Al) and poly(3,4-ethylene dioxathiophene)/poly(styrene sulfonate) (PEDOT:PSS). The conductive polymer

PEDOT:PSS is coated on the glass/indium tin oxide (ITO) substrate. PEDOT:PSS exhibits hygroscopic and acidic properties, which can lead to corrosion of the ITO layer.⁷⁵ Consequently, indium (In) diffuses into the PEDOT:PSS layer and can migrate towards the photoactive layers, potentially affecting the performance of the OSCs.⁷⁶⁻⁷⁸ Various alternative charge-transport materials have been used as substitutes for PEDOT:PSS and can be applied by either thermal evaporation or solution processing.^{78,79} At the same time, the top electrode may also degrade when in contact with oxygen and moisture.

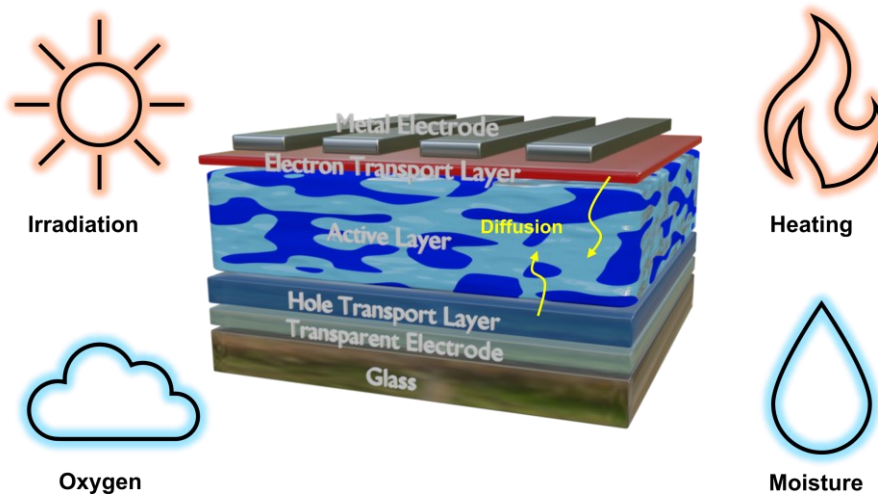


Figure 1.4: Schematic of OSC illustrating some of the degradation processes.

To prevent this, transparent epoxy and glass slide encapsulation are used as barriers against moisture and oxygen. Nevertheless, this will increase the production costs. Although advances in encapsulation materials have improved their performance, it is important to explore materials with inherent stability that can resist moisture and oxygen.^{34,73,74,80,81}

1.3 Motivation

Although OSCs show promising alternatives to conventional silicon-based solar cells due to their flexibility, low cost, and ease of production. Despite their potential, OSCs suffer from material stability issues and longer device lifetime, which hinder their widespread adoption in commercial applications. Upon degradation, the optical and electronic properties of the organic semiconductor can change.⁸²⁻⁸⁶ Extrinsic factors, such as oxygen and moisture, can affect the photoactive layer of

the OSCs.⁸⁷⁻⁸⁹ Moreover, continuous exposure to light can lead to photo-induced degradation of the active layer in OSCs.⁹⁰⁻⁹²

This thesis aims to identify factors that influence the photodegradation rate of thin films of state-of-the-art organic semiconductors used as photoactive materials for high-efficiency solar cells and to investigate the relation between the photodegradation behavior of these organic semiconductors and the degradation of the electrical performance of OSCs. The state-of-the-art materials used in this thesis are donor polymers PBDB-T, PM6, and PTQ10, as well as NFAs, including the small molecules Y5 and Y6, and the copolymer acceptors PF5-Y5 and PYT.⁹³ To assess the photodegradation of thin-film and OSCs, samples were intentionally exposed to continuous light from a solar simulator (AM1.5) for varying durations under ambient conditions (air, room temperature). A range of characterization techniques, such as UV-vis spectroscopy, Photoluminescence (PL), Fourier Transform Infrared Spectroscopy (FTIR), Atomic Force Microscopy (AFM), and synchrotron-based techniques such X-ray, and Ultraviolet Photoelectron Spectroscopy (XPS and UPS), and Near Edge X-ray Absorption Fine Structure (NEXAFS), were employed to analyze compositional and structural changes in the materials. To evaluate OSC performance, electrical and optoelectronic characterization techniques are employed, including current-voltage (I-V), External Quantum Efficiency (EQE), and Photo-CELIV measurements.

1.4 Outline of the thesis

This doctoral thesis is organized into two main parts. The first part comprises six chapters. Chapter 1 introduces the fundamentals of solar cells, while Chapter 2 provides an overview of organic semiconductors. Chapter 3 describes the working principles of organic solar cells (OSCs). Chapter 4 presents the materials, experimental techniques, and device fabrication employed in this research. Chapter 5 summarizes the papers included in the thesis, Chapter 6 presents the main conclusions, and Chapter 7 outlines future research perspectives. The second part comprises the appended publications: two peer-reviewed journal articles, one peer-

reviewed conference paper, one submitted manuscript, and one manuscript for journal publication.

Chapter 2

Organic semiconductors

Organic semiconductors are materials composed of organic molecules, primarily carbon and hydrogen, with a few heteroatoms such as oxygen, sulfur, or nitrogen, and exhibit properties typically associated with semiconductors. These materials feature conjugated systems that enable efficient charge transport. Based on their molecular architecture, conjugated organic semiconductors are broadly classified into two categories: polymers and small molecules. Moreover, the tunable bandgap of organic semiconductors enables light absorption and emission across a broad range of wavelengths within the visible spectrum. Their electrical conductivity and tunable bandgap make them suitable for fabricating various semiconductor devices, including organic solar cells (OSCs), organic light-emitting diodes (OLEDs), and organic field-effect transistors (OFETs). Beyond their semiconducting properties, organic semiconductors are also appreciated for their lightweight nature, solution-processability, mechanical flexibility, low production costs, and suitability for large-scale fabrication.^{38,94}

The semiconducting properties of organic and inorganic materials differ significantly. Conventional inorganic semiconductors typically exhibit relatively low band gaps, for instance, 0.67 eV for Germanium (Ge), 1.1 eV for Silicon (Si), and 1.4 eV for Gallium Arsenide (GaAs). In these materials, free charge carriers can be generated (at low concentrations) at room temperature via thermal excitation of electrons from the valence band to the conduction band. The intrinsic conductivity of inorganic semiconductors generally falls within the range of 10^{-8} to $10^{-2} \Omega^{-1} \text{ cm}^{-1}$. Furthermore, the relatively large dielectric constant of inorganic semiconductors ($\epsilon_r > 11$) means that the Coulomb interaction between electrons and holes becomes unimportant, so that light absorption at room temperature directly creates free charge carriers. Unlike inorganic semiconductors, the conductivity of organic semiconductors is typically extrinsic, depending on doping and the efficiency of

exciton dissociation into free charge carriers. Due to their relatively low dielectric constant ($\epsilon_r = 3-5$), electrons and holes in organic semiconductors experience strong Coulombic attraction, forming tightly bound electron-hole pairs known as excitons.⁹⁵

2.1 Conjugated molecules

Organic semiconductors are primarily composed of carbon-based materials, and their properties are largely determined by the delocalization of π -electrons across conjugated molecular structures. Carbon, with an atomic number of 6, has an electronic configuration $1s^2 2s^2 2p^2$. The two 1s electrons are tightly bound to the nucleus, while the remaining four valence electrons participate in chemical bonding. Carbon can exhibit three types of hybridization: sp^3 , sp^2 , and sp . The sp^3 hybridization forms tetrahedral structures with bond angles of 109.5° , as in diamond. The sp^2 hybridization results in trigonal planar or hexagonal structures with bond angles of 120° , as seen in graphene. The sp hybridization produces linear structures with bond angles of 180° (Figure 2.1). The favorable hybridization for conjugation to happen in the molecules is sp^2 .

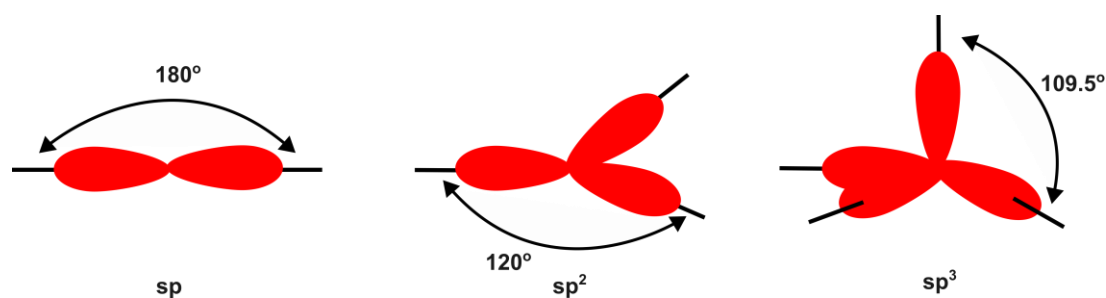


Figure 2.1: The sp , sp^2 , and sp^3 hybrid orbitals.

Now let us consider the ethene molecule, C_2H_4 (Figure 2.2), where each carbon atom has sp^2 hybridization. The $2s$ orbital and two of the $2p$ orbitals (p_x and p_y) combine to form three sp^2 hybrid orbitals, which are used to form σ -bonds. The third $2p$ orbital (p_z) remains unhybridized and contains one electron. This unhybridized p -orbital can overlap with p -orbitals on adjacent atoms, enabling the delocalization of π -electrons across multiple atoms, which is essential for

conjugation.⁹⁶ The two p_x orbitals overlap and form a π -bond, resulting in a double bond, as shown in Figure 2.2, and the π^* is the antibonding. The electrons in the σ -bonds are strongly localized and form the backbone of the polymers, whereas in the π -bonds, electrons are delocalized. The increase in π -electrons delocalization across adjacent monomer units is essential for electronic conduction in conjugated molecules. The electron density of the π -bonding configuration is comparatively more stable than in the π^* -antibonding configuration.

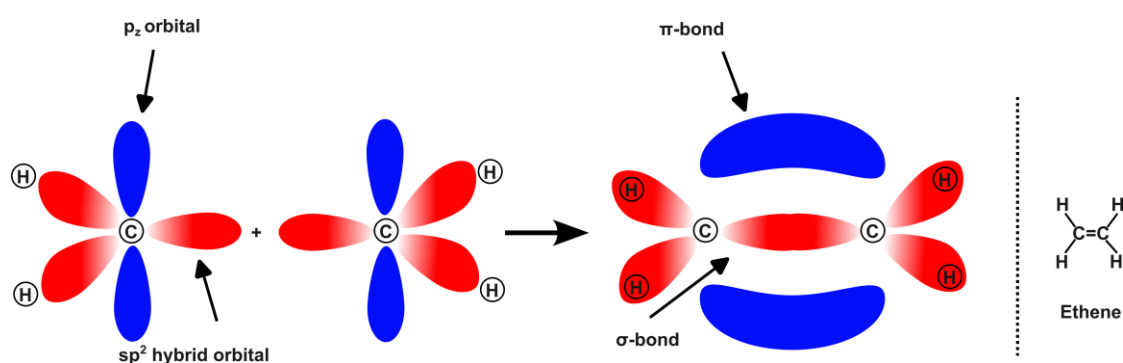


Figure 2.2: Formation of σ and π in sp^2 hybridization for the ethene molecule.

During the formation of a solid, molecular orbitals from adjacent molecules can interact and merge to form extended electronic bands, particularly when the molecules are closely packed, as in covalent or molecular solids. In contrast, in molecular solids held together primarily by van der Waals interactions, these weak forces facilitate only limited physical attraction between non-covalently bonded molecules and do not result in significant overlap between bonding and antibonding molecular orbitals. When orbital overlap occurs, it leads to splitting of energy levels into electron-filled π (bonding) states and unfilled π^* (antibonding) states, separated by a forbidden energy gap. In organic semiconductors, the resulting electronic bands are typically narrower than those found in inorganic semiconductors due to the weak intermolecular van der Waals interactions. The bandgap (E_g) of an organic semiconductor is defined as the energy difference between the highest occupied molecular orbital (HOMO), which corresponds to the π -bonding orbital, and the lowest unoccupied molecular orbital (LUMO), which corresponds to the π^* -

antibonding orbital. This energy separation is also referred to as the HOMO-LUMO gap.

The electron-filled states below the bandgap constitute the valence band, while the unfilled states above the bandgap form the conduction band. The bandgap depends strongly on the conjugation length of the molecule; as the conjugation length increases, the bandgap decreases due to enhanced π -electron delocalization over a larger molecular framework.⁹⁷ A schematic representation of the electronic structure of sp^2 -hybridized orbitals is shown in Figure 2.3.

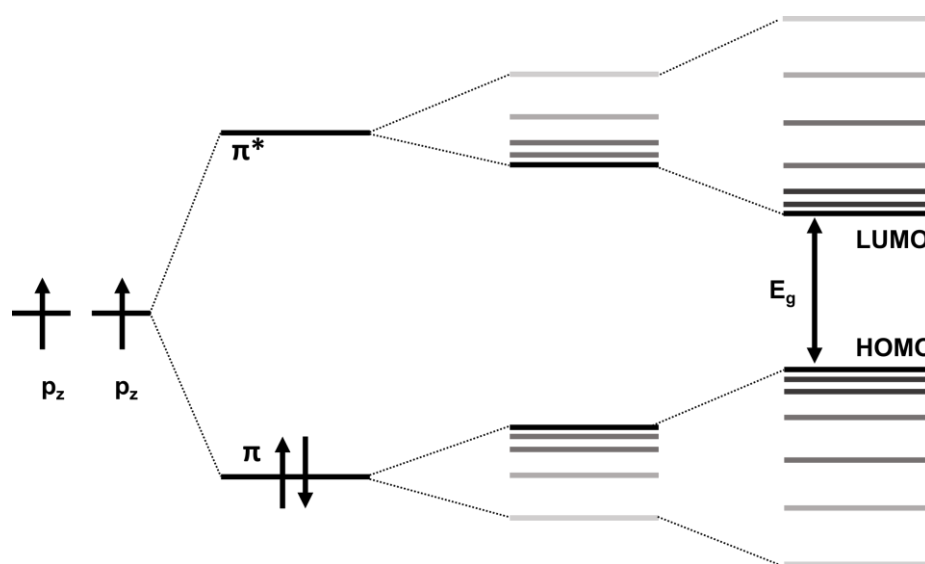


Figure 2.3: Schematic representation of the electronic structure of a sp^2 hybridized orbital.

Small molecules are discrete, rigid entities characterized by well-defined molecular weights and structural configurations. Conjugated small molecules contain alternating single and double bonds, which allow for the delocalization of π -electrons along the molecular backbone. In contrast, polymers consist of long chains formed by the repetitive linkage of monomer units, resulting in a distribution of molecular weights and structural diversity. The arrangement of these repeating units can vary, leading to different polymer architectures. When all repeating units are chemically identical, the material is referred to as a homopolymer, whereas a copolymer consists of two or more distinct types of repeating units.⁹⁵

2.2 Morphology

In general, the donor and acceptor materials are mixed with a solvent and heated to dissolve, with the temperature depending on the solvent and molecules used. The selection of appropriate solvents and the blend ratio is crucial for dissolving the donor and acceptor materials. For solution deposition, various techniques are available, including spin coating, slot-die coating, blade coating, and others.⁹⁸ However, the spin coating technique is widely used for lab-scale production and is the method used in this thesis. During spin coating, as the solvent evaporates, donor and acceptor molecules interact, and the phase separates into donor-rich or acceptor-rich domains. After film formation, the films are typically annealed to remove residual solvent. This annealing process allows the molecular structures in the donor and acceptor materials to reorganize, thereby improving phase separation. The phase-separated donor-rich or acceptor-rich domains should typically be in the 10 nm range, which is important for efficient charge separation and transport in OSCs. The spin coating process is discussed in detail in Chapter 4. To control the morphology of the active layers, several techniques are used, including adjusting the spin speed, incorporating additives, exploring different solvents, implementing post-annealing processes, selecting appropriate substrates, and choosing different materials.^{99,100} The spin coating is mainly used for small-area devices, as it is difficult to fabricate a uniform film on large-area substrates. For large-area fabrication, other coating techniques are used, including spray coating, dip coating, blade coating, and slot-die coating.⁹⁸

The morphology of the active layer plays an important role in the efficiency and performance of OSCs. Morphology can affect exciton generation, dissociation, charge transport, and charge collection. Details of the different processes are discussed in the next chapter. The active layers for the OSCs can be prepared via two techniques: layer-by-layer coating (LBL) and bulk heterojunction (BHJ).¹⁰¹ The LBL strategy involves the sequential deposition of donor and acceptor materials to fabricate an active layer. Indeed, it allows optimization of individual material layers, making it easier to characterize and fine-tune their properties. It is challenging in terms of processability, including solvent selection, active-layer uniformity, and

washing off the bottom layer during fabrication.¹⁰² In contrast, in bulk heterojunction (BHJ) solar cells, donor and acceptor materials are blended in a common solvent. By selecting an appropriate solvent and optimizing the blend ratio, a continuous interpenetrating network forms, along with phase-separated donor-rich and acceptor-rich domains. This facilitates exciton dissociation upon photoexcitation owing to the larger interfacial area between the donor and acceptor materials. The details about the BHJ are discussed in the next chapter.

2.2.1 Photochemical stability

The photochemical stability of the active layer is crucial for determining the operational stability and longevity of OSCs. Upon exposure to light, organic semiconductors can undergo a variety of photochemical reactions, often leading to bond cleavage, isomerization, or the formation of reactive intermediate species, which collectively contribute to the degradation of the active layer.^{73,74,103} Over time, oxygen from the ambient atmosphere can further interact with photoexcited molecules through two major degradation pathways: (1) the generation of singlet oxygen (1O_2) and (2) the formation of superoxide radicals (O_2^-).¹⁰⁴⁻¹⁰⁷ These reactive oxygen species (ROS) readily react with organic molecules, leading to photo-oxidation, structural modifications, and changes in the electrical and optical properties of the active-layer materials. Even in encapsulated devices, oxygen diffusion into the active layer can occur under prolonged duration, leading to photooxidation and progressive deterioration of device performance. Such degradation processes adversely affect charge transport, exciton dissociation, and energy-level alignment, ultimately reducing PCE and device lifetime.

To mitigate these effects, several molecular design and device engineering strategies have been developed. From a molecular perspective, enhancing intrinsic photostability can be achieved by incorporating electron-withdrawing groups and introducing stabilizing side chains that reduce molecular reactivity with oxygen.^{34,73,86,108} The use of highly crystalline donor and acceptor materials can also suppress photochemical degradation by limiting the diffusion of oxygen and reactive species into the active layer. Furthermore, end-group functionalization and

cross-linkable moieties have been explored to strengthen molecular robustness and improve morphological stability under illumination. From a device engineering standpoint, encapsulation techniques, the integration of UV-filtering interlayers, and the use of oxygen- and moisture-impermeable barrier layers have proven effective in limiting environmental degradation. Optimizing the active layer morphology and energy-level alignment can further minimize charge accumulation, thereby reducing photo-induced oxidative stress within the device. Collectively, these strategies enhance the photochemical durability and long-term operational stability of OSCs. Further details about the device's stability are discussed in Chapter 3.

2.2.1.1 Photochemical stability of the electron donor (Polymers)

Over the past few years, significant progress in the development of new electron donor materials has led to substantial improvements in the performance of OSCs.^{68,100,109} Electron donor polymers can generally be classified into two main categories: D-type and donor-acceptor (D-A) type polymers, where D denotes the donor segment and A denotes the acceptor segment. Typical examples of D-type donor polymers include P3HT, P(DOT), P(ProDOT)-B, and MDMO-PPV. These D-type polymers typically have a relatively wide bandgap, limiting their light absorption in the visible and near-infrared regions. To overcome this limitation, extensive research has focused on the development of D-A copolymers, in which electron-donating (D) and electron-accepting (A) units are alternately incorporated along the polymer backbone. This donor-acceptor hybridization effectively reduces the polymer bandgap by enhancing intramolecular charge transfer (ICT) between the D and A segments, thereby broadening their absorption spectrum. Through careful monomer selection and molecular design, D-A type polymers have come to dominate OSC research over the past decade. Among the most efficient D-A donor polymers reported to date are PTB7-Th, PBDB-T, PM6, D18, and PTQ10, which have demonstrated excellent PCEs.¹¹⁰⁻¹¹² In this thesis, particular emphasis is placed on investigating the photochemical stability of three representative high-performance D-A electron donor polymers: PBDB-T, PM6, and PTQ10.

This section focuses on the photochemical degradation of electron donor polymers. Donor-acceptor (D-A) polymers are conjugated polymers with attached side chains: the conjugated backbone serves as the charge-transport pathway, while the alkyl side chains enhance solution processability and film-forming properties. However, the conjugated backbone is susceptible to oxidation and ring-opening reactions upon exposure to light and air. Meanwhile, the side chains are prone to hydrogen abstraction and chain scission reactions, which further contribute to molecular degradation.^{73,113} For example, Tournebize *et al.* investigated the role of side chains in the photodegradation of conjugated polymers and demonstrated their significant influence on the overall stability of the materials.¹⁰⁸ Ratcliff *et al.* examined the photodegradation behavior of five different polymer donors under illumination in air, all of which contained an alkyl thienyl-substituted benzodithiophene (BDT-T, also referred to as BDT) donor unit, but featured different acceptor components.¹¹³ Using a combination of optical and X-ray spectroscopic techniques, they observed oxygen incorporation into the alkyl side chains and sulfur oxidation on the BDT-T units. More recently, Wang *et al.* demonstrated that the donor polymer plays a critical role in the photochemical stability of non-fullerene OSCs. Structural instability in the BDT-thiophene motif of PM6 and D18 leads to rapid exciton trapping and reduced charge generation, whereas PTQ10, lacking this motif, exhibits superior stability.⁸⁵

2.2.1.2 Photochemical stability of the electron acceptor

Fullerenes and their derivatives have long dominated as electron acceptors in OSCs, thanks to their excellent solubility, high electron mobility, and compatibility with a wide range of electron donor materials.^{114,115} However, fullerene is sensitive to oxygen, and photo-induced degradation occurs upon illumination. For example, thin films of PC₆₀BM and PC₇₀BM degrade when exposed to light under ambient conditions.^{106,116} Anselmo *et al.* studied the photodegradation of PCBM and C₆₀ films under AM 1.5 illumination in ambient conditions. The results indicate that both HOMO and LUMO are affected during photodegradation, due to the destruction of the molecule's conjugation.¹¹⁷ The detailed insights into the photooxidation of PC₆₀BM were provided by Brumboiu *et al.* in a joint

experimental-theoretical study based on IR and X-ray spectroscopy techniques to understand the photooxidation products.¹¹⁸ The study confirms that photooxidation mainly disrupts the fullerene cage, forming numerous photooxidation products such as carbonyls, dicarbonyls, and anhydrides. Even in the absence of oxygen, photo-induced dimerization of fullerenes has been reported.^{119,120} The instability and low absorbance in the visible spectral range limit the use of fullerene acceptors in OPV technology.

In recent decades, the synthesis of non-fullerene acceptors (NFAs) has advanced significantly in OSC technology, thanks to their high visible-range absorption coefficients, tunable band gaps, molecular functionalization, and suitable energy-level alignment with donors.¹²¹⁻¹²³ The molecular structure of NFAs is based on acceptor (A) and donor (D) repeating units as a backbone with branched side chains. For example, the ITIC family has an A-D-A configuration, while the Y-series has an A-D-A'-D-A configuration. The conjugated core is made up of fused or non-fused rings. Fused rings make the molecule relatively planar, facilitating high intermolecular interaction and packing. In contrast, non-fused rings introduce twists into the molecular structure, leading to different conformations. The strong packing tendency of fused NFAs often leads to excessively large aggregates, which can negatively affect exciton dissociation, charge-carrier mobility, and charge-transport properties in OSCs.¹²⁴ In contrast, non-fused NFAs with twisted conformations exhibit weakened π -electron delocalization between the donor and acceptor units, which can affect intramolecular charge transfer. To enhance the planarity of non-fused NFAs, intermolecular conformational locks can be introduced by incorporating interactions such as O \cdots S, O \cdots H, F \cdots H, and F \cdots S. These interactions help stabilize the molecular conformation, promoting a more planar structure and improving the overall performance of OSCs.¹²⁵ Like in the case of fullerene acceptors, oxygen can diffuse into the active layer and react with NFAs, potentially damaging their molecular structure via the photooxidation process. For instance, Wang *et al.* studied the effect of oxygen and moisture on both fullerene and NFAs using *in situ* photoelectron spectroscopy.⁸⁷ They observed that NFAs, such as p/m-ITIC and o-IDTBR, exhibit higher moisture resistance and slightly lower resistance

to oxygen compared to PC₇₁BM fullerene acceptors. Additionally, the photostability of ITIC and ITIC-4F films prepared by blade coating was compared, revealing that fluorine in ITIC reduces the photooxidation rate.⁸⁸ Recently, Liu *et al.* reported that the photostability of NFAs strongly depends on the molecular structure.⁸² They observed that the non-fused ring acceptor (PTIC) remains highly photostable compared to the fused ring acceptor (ITIC-4F) and to the semi-fused ring acceptor (HF-PCIC) during photodegradation. The photoinduced isomerization breaks the exocyclic vinyl group between the donor and acceptor units in ITIC-4F and HF-PCIC. However, in PTIC, the vinyl group is protected by the side chain on the outside, and a tightly packed, solid-state film prevents photo-induced isomerization. Zhang *et al.* investigated the photostability of PM6:Y6 using in situ X-ray photoelectron spectroscopy. They found that the moisture and oxygen primarily interact with the cyano group in Y6, while PM6 interacts with the sulfur attached to the backbone.⁸³

2.2.1.3 Degradation due to electron and energy transfer in the donor-acceptor blend

As discussed above, photochemical degradation can occur in the presence of light and oxygen, affecting both electron donors and electron acceptors. In this section, the degradation mechanisms due to electron and energy transfer in the donor-acceptor blend are discussed. In donor/acceptor blends, the charge transfer is an essential process for photocurrent generation. However, prolonged illumination in air can also lead to the photochemical degradation of both the donor and acceptor components. Upon light absorption, excitons (bound electron–hole pairs) are generated within either the donor or acceptor domains. Once the excitons are dissociated into free charge carriers, the photogenerated electron from the donor can either transfer to the acceptor or to the dioxygen molecule, provided that the excited state of the donor has higher energy than the reduction potential of O₂ (as illustrated in Figure 2.4). Electron transfer to O₂ can generate the superoxide anion, which can then react with either the donor or the acceptor to form oxidation products.^{107,126} Electron transfer to O₂ is thermodynamically unfavorable since the reduction potential (energy level) of O₂ is higher than the LUMO energy level of the

acceptor. In contrast, the singlet oxygen (1O_2) species can be formed by energy transfer from the triplet excited state of an acceptor molecule (photosensitizer) to ground-state molecular oxygen. A schematic of superoxide radicals generated via electron and singlet oxygen generated via energy transfer is shown in Figure 2.4.

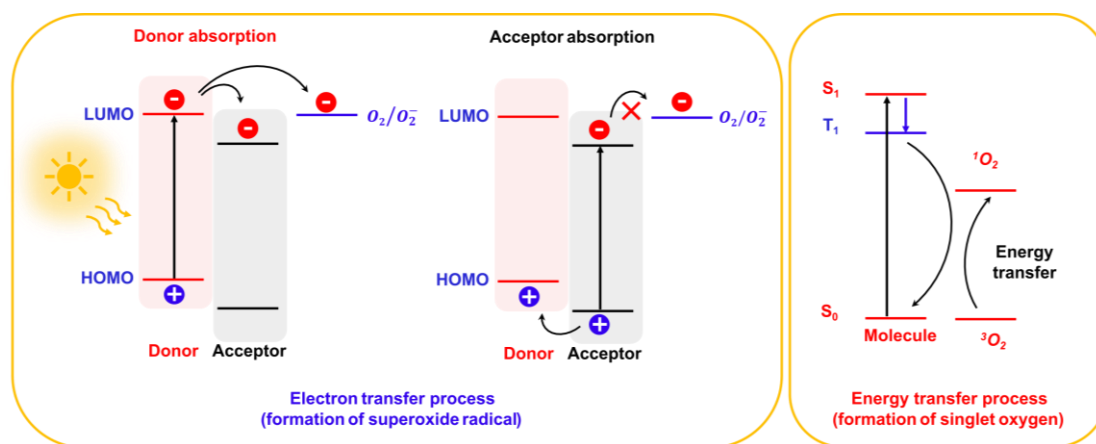


Figure 2.4: Schematic representation of electron transfer and energy transfer processes in the donor-acceptor blend, illustrating the formation of superoxide radicals (O_2^-) and singlet oxygen (1O_2).

The photooxidation of donor and acceptor moieties can lead to the formation of sulfoxides, peroxides, and carbonyl groups, further accelerating the degradation of the active layer.^{93,126,127} Overall, these degradation pathways result in the formation of trap states, loss of conjugation, and changes in molecular energy levels. These effects collectively reduce charge generation efficiency, carrier mobility, and device performance, thereby limiting the operational stability and lifetime of OSCs.

2.2.2 Morphological stability

The morphological stability of the photoactive layer can also affect the performance, efficiency, and lifetime of OSCs. The key factors that may influence morphological stability are thermal stress, light-induced degradation, and electrical stress. Under these stress conditions, the active layer morphology can evolve due to molecular diffusion, domain coarsening, crystallization changes, or vertical phase segregation, leading to reduced interfacial area and disrupted charge-transport pathways, both of which play a critical role in long-term morphological stability.⁹⁹ Such structural rearrangements are particularly relevant in non-fullerene systems

based on materials, where aggregation and polymorphic transitions can significantly impact device stability.^{88,128,129}

During OSC operation under one-sun conditions, the solar cell temperature reaches 85°C, the standard test temperature, and under these conditions, the solar cell can degrade, affecting its morphology.¹³⁰ Sachs-Quintana *et al.* observed that morphological degradation of P3HT:PC₆₀BM and PCDTBT:PC₆₀BM is associated with the T_g of P3HT and PCDTBT. It was observed that the open-circuit voltage (V_{oc}) begins to decrease once the annealing temperature exceeds the T_g of P3HT and PCBTBT in the P3HT:PC₆₀BM and PCDTBT:PC₆₀BM blends.¹³¹ Thermally induced aggregation and crystallization of fullerene acceptors affect the charge separation and transport properties of the OSCs.^{132,133} Unlike fullerene, the NFAs have a planar molecular structure based on A-D-A and A-D-A-D-A configuration. This provides greater molecular flexibility than fullerene acceptors and has demonstrated superior morphological stability for OSCs. For example, Li *et al.* demonstrated excellent thermal stability for unfused core-based NFA, DF-PCIC. The PBDB-T:DF-PCIC and PBDB-T:PC₇₁BM thin film were thermally treated at 180°C and it was observed that PBDB-T:PC₇₁BM exhibits granular agglomerations.¹³⁴ Kang An *et al.* reported that when two L8-BO:Y6 NFAs are mixed with donor PTzBI-dF, thermal and morphological stability for the ternary system improves compared to a blend of PTzBI-dF: L8-BO and PTzBI-dF:Y6.¹³⁵ The polymerized NFAs have shown excellent thermal and mechanical stability, owing to their higher T_g compared to small-molecule NFAs.¹⁰⁹

In summary, photochemical and morphological degradation processes critically influence the stability and operational lifetime of OSCs. Photooxidation, molecular structural changes, and morphology evolution under different environmental conditions and thermal stress can significantly deteriorate the electrical and optical properties of the photoactive layer. A comprehensive understanding of these degradation mechanisms is essential for designing more stable donor and acceptor materials. Such insights are crucial for enhancing the long-term performance and practical applicability of OSCs.

Chapter 3

Organic solar cells

Organic solar cells (OSCs) consist of several thin layers, including the photoactive layer, charge-transport layers, and electrodes. The photoactive layer is typically sandwiched between an electron transport layer and a hole transport layer, which facilitates the selective extraction and transport of electrons and holes to the respective electrodes. These cells are mainly fabricated using two distinct device architectures: conventional and inverted, as depicted in Figure 3.1. In the conventional configuration, the transparent bottom electrode (anode) collects holes, whereas in the inverted configuration, it serves as the cathode, collecting electrons from the active layer. The photoactive layer consists of an electron donor and an electron acceptor, both of which are molecular semiconductors. To ensure efficient charge-carrier collection, charge transport with a well-aligned work function is integrated between the active layer and the electrodes. Commonly used materials for electron transport layers are ZnO, LiF, and PDINO, and for hole transport layers are PEDOT:PSS, 2PACz, and MoO₃.¹³⁶⁻¹³⁸

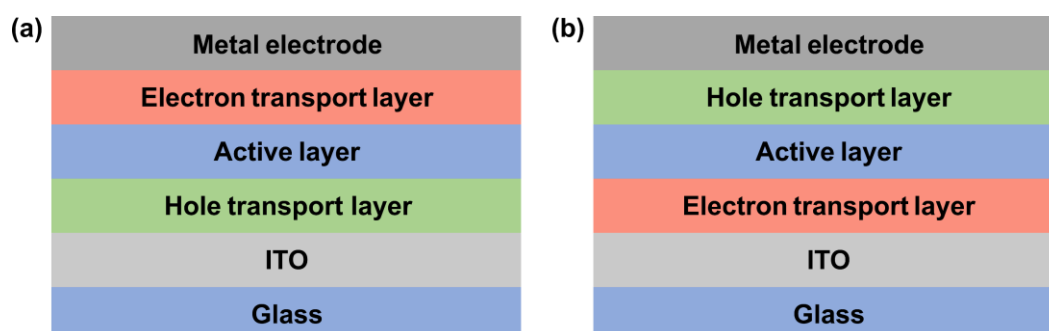


Figure 3.1: The two different device architectures (a) conventional and (b) inverted.

3.1 Working principle

The working principle of OSCs can be broadly divided into four key stages: (a) photon absorption and exciton generation, (b) exciton diffusion and formation of the charge transfer (CT) state, (c) exciton dissociation and charge separation, and

(d) charge transport and collection. These processes occur sequentially but over different time scales. Schematic representations of these individual processes are illustrated in Figure 3.2.

3.1.1 Photon absorption and Frenkel exciton formation

When light is incident on an organic semiconductor, it is absorbed if the photon energy of the incident light is greater than or equal to the band gap of the semiconductor. Therefore, the choice of donor and acceptor materials is crucial to ensure that they can absorb radiation across a broad range of wavelengths of the solar spectrum. The absorption coefficient of organic semiconductors ($\sim 10^5 \text{ cm}^{-1}$) is higher than that of inorganic silicon ($\sim 10^3 \text{ cm}^{-1}$), which enables OSCs to achieve higher absorption with a thickness three orders of magnitude smaller than that of silicon semiconductors.^{139,140}

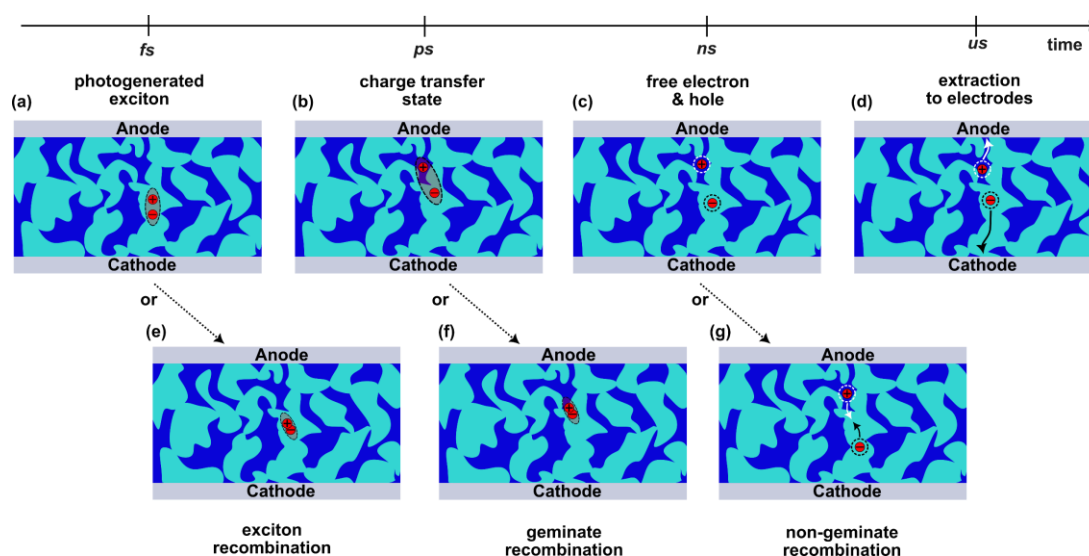


Figure 3.2: The different processes involved during the operation of organic solar cells (a) photon absorption, (b) exciton diffusion and charge transfer state formation, (c) charge separation, and (d) charge transport and collection, as well as the loss mechanisms (e-g) based on photogenerated charge carriers.

Upon light absorption in organic semiconductors, Frenkel-type excitons are generated. These are bound electron-hole pairs with a binding energy ranging from 100 to 1000 meV.¹⁴¹ Organic semiconductors typically have a low dielectric constant (3-5), whereas inorganic semiconductors have a higher dielectric constant (12-13),

which facilitates the formation of Mott-Wannier excitons that have a much lower binding energy, around 10 meV.^{95,142}

3.1.2 Exciton diffusion and CT state formation

Upon light absorption, an electron in the organic molecule is excited to a higher energy state. The Frenkel exciton, the electron-hole pair that is formed in this process, has a high binding energy due to the strong Coulomb interaction between the electron and the hole. The electron can then relax back to the ground state through either a radiative or non-radiative process, as depicted in the Jablonski diagram (Figure 3.3).

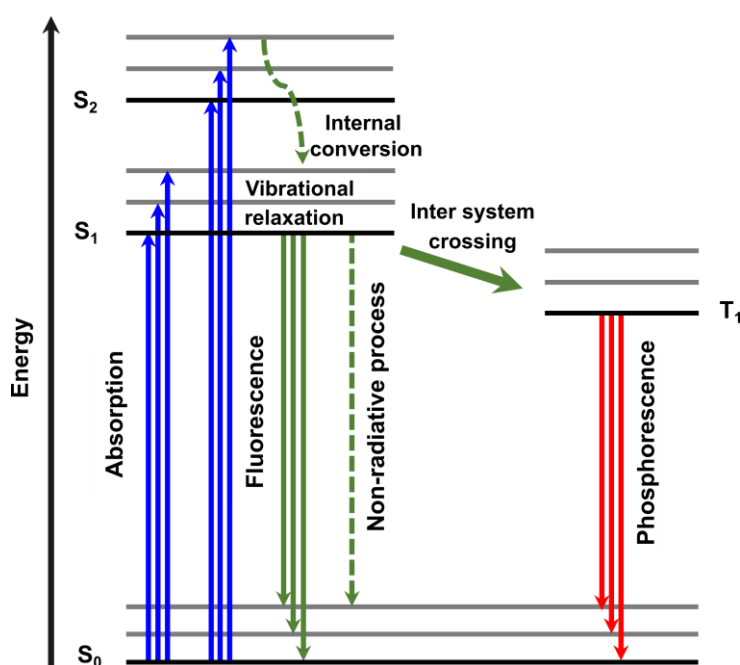


Figure 3.3: Jablonski diagram for an organic molecule with different electronic levels, S_0 , S_1 , S_2 , and T_1 . The S_0 is the ground state, S_1 and S_2 are the first and second excited states, and T_1 is the triplet state. The arrow indicates the absorption and recombination processes.

In the radiative process, photons are emitted within sub-nanosecond timescales, a process known as fluorescence.¹⁴³ During the non-radiative process, the electron and hole recombine, releasing energy in the form of heat. Additionally, the electron can undergo intersystem crossing from the singlet state to the triplet state, where it can recombine and emit photons. This process is known as phosphorescence, and the electrons in the triplet state have a longer lifetime, typically 1-10 μs .¹⁴⁴ In OSCs,

the goal is to dissociate the electron-hole pairs before they relax to the ground state. To achieve this, the excitons must diffuse toward the donor-acceptor interface, as shown in Figure 3.2a. When the exciton reaches the donor-acceptor interface, the electron is transferred from the donor's LUMO to the acceptor's LUMO, creating a charge transfer (CT) state across the interface. In this CT state, the electron resides on the acceptor, and the hole remains on the donor. For efficient charge transfer, a type II heterostructure is required, where the donor material has a lower ionization potential, and the acceptor material has a higher electron affinity. If the exciton fails to reach the interface, it is highly likely to recombine before free charge carriers are generated. The exciton diffusion length, which is the distance an exciton can travel from its point of generation, is typically around 10 nm.^{95,143,145,146} The exciton diffusion length (L_{exc}) can be expressed as:

$$L_{exc} = \sqrt{D_{exc} \times \tau_{exc}} \quad (3.1)$$

where D_{exc} is the diffusion coefficient of the exciton, and τ_{exc} is the lifetime of the exciton. The typical lifetime of a singlet exciton is less than 5 ns. To facilitate the diffusion and dissociation of photogenerated excitons into free charge carriers, it is essential to use a material with a high exciton diffusion coefficient in OSCs. This can also be achieved by optimizing the morphology of the donor-acceptor (D/A) blend, as morphology influences the probability of exciton dissociation and the efficiency of exciton separation at the D/A interface.^{147,148}

3.1.3 Formation of charge separation state

The formation of the charge-transfer (CT) state is a complex process that serves as an intermediate state in OSCs. Once an exciton diffuses to the donor-acceptor (D/A) interface, the electron-hole pair must dissociate into free charge carriers. This dissociation is a critical step in the overall charge separation process. The schematic of this process is illustrated in Figure 3.4. In organic photovoltaics, a key requirement for efficient charge dissociation is an energy offset between the HOMO and LUMO levels of the donor and acceptor materials. This energy offset helps dissociate excitons into free charge carriers by overcoming the Coulombic attraction between the electron and hole.¹⁴⁹ For polymer:fullerene-based systems,

the energy offset typically ranges from 0.2 to 0.5 eV.^{150,151} However, in NFA-based systems, these energy offsets are generally lower.¹⁵²⁻¹⁵⁵ Once the exciton reaches the donor-acceptor (D/A) interface, the electron and hole form a CT state, with the electron on the acceptor and the hole on the donor. This is also referred to as a CT exciton (Figure 3.2b).¹⁵⁶ The electron in the CT state can relax from the excited state to the ground state via radiative or non-radiative processes. The lifetime of the CT exciton in polymer/non-fullerene systems is typically on the order of sub-picoseconds.¹⁵⁷ Understanding the D/A interface and the dynamics of exciton dissociation is crucial, as it directly influences the V_{OC} of OSCs. The efficiency of exciton dissociation and the formation of CT excitons are strongly influenced by the nanomorphology of the bulk heterojunction, which governs the charge transfer process.

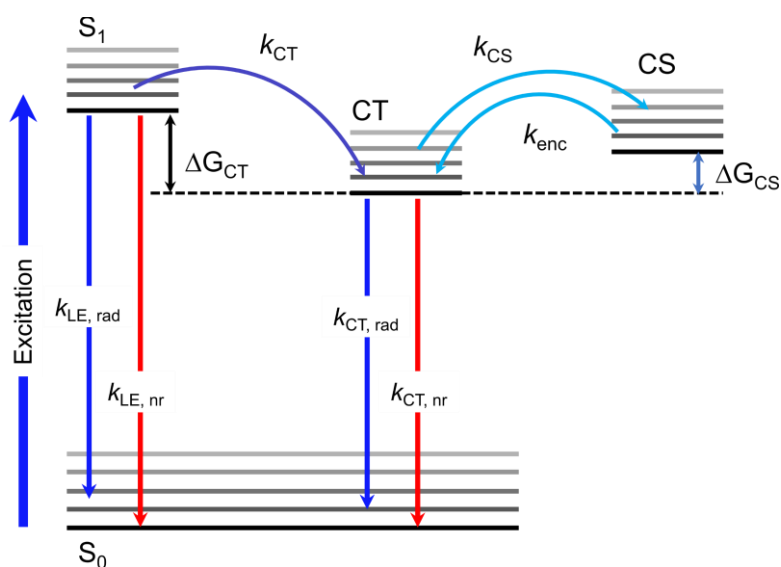


Figure 3.4: Schematic of the energy level diagram from the exciton formation to the charge separation state. Here, S_0 and S_1 are the ground state and first excited state. The symbol k represents the rate constant for processes such as LE (local exciton), CT (charge transfer), and CS (charge separation), and ΔG is the Gibbs energy. Adapted from the reference.¹⁵⁸

3.1.4 Charge transport and collection

Once the exciton dissociates into free charge carriers from the CT state, electrons and holes must move toward their respective electrodes because of the difference in work functions between the electrodes, as illustrated in Figures 3.2 (c-d). Charge transport in inorganic semiconductors differs significantly from that in organic

semiconductors. In inorganic semiconductors, atoms are arranged in well-ordered crystalline structures with strong covalent bonds, allowing charges to move more efficiently and resulting in high charge-carrier mobility (typically 10^2 - 10^3 cm^2/Vs). In contrast, organic semiconductors have a more complex structure due to side chains and molecular backbones, resulting in a mixture of amorphous and crystalline regions. The backbone of organic molecules consists of alternating single and double bonds, which enable electron delocalization along the conjugation length. As a result, the charge carrier mobility in organic semiconductors is generally lower, ranging from approximately 10^{-5} to 10^{-3} cm^2/Vs . Mobility can also be influenced by factors such as intermolecular distances and molecular orientations between organic molecules. In recent years, however, advances in materials design have enabled organic semiconductors to achieve charge-carrier mobilities exceeding 10 cm^2/Vs .¹⁵⁹⁻¹⁶¹

3.1.5 Recombination

As discussed in previous sections, photon absorption, exciton diffusion, charge-transfer state formation, charge transport, and charge collection involve processes in which charge carriers may recombine, which can affect the OSC's device performance. Two types of recombination can occur: geminate and non-geminate recombination. These recombination processes are illustrated in Figure 3.2 (e-g).

3.1.5.1 Geminate recombination

The term 'geminate' is derived from the Latin word Gemini, meaning twins, and refers to the recombination of an electron and a hole generated by the absorption of a single photon. There are two types of geminate recombination: one occurring within the bulk material and the other at the donor/acceptor (D/A) interfaces as shown in Figure 3.2(e & f). When an exciton is formed upon photon absorption, the electron and hole remain bound together as a Frenkel exciton. Due to the strong binding energy between the electron and hole, the exciton may recombine within the bulk before reaching the D/A interface. This recombination is influenced by the exciton's limited diffusion length, typically around 10 nm. Alternatively, recombination can occur at the D/A interface due to the strong electrostatic

attraction between the electron and hole. In both cases, driven by a single photon, recombination takes place before the exciton can separate into free charge carriers. Recombination can occur via radiative or non-radiative processes.¹⁵⁶

3.1.5.2 Non-geminate recombination

Once the charge carriers are free from the geminate pair, they move towards their respective electrodes due to the difference in work functions between the electrodes. This process is depicted in Figure 3.2g. During this process, the free charge carriers may recombine. Unlike geminate pairs, these charges are generated by separate photons. There are three types of non-geminate recombination: bimolecular recombination, trap-assisted recombination, and Auger recombination.¹⁵⁶

Bimolecular recombination occurs when free electron and hole pairs recombine. Bimolecular recombination can increase due to an imbalance in electron and hole mobilities, thereby increasing the charge-carrier concentration in the devices.¹⁶² The Langevin expression for bimolecular recombination (R_L) is described in Equation 3.2:

$$R_L = \frac{q}{\varepsilon} (\mu_n + \mu_p) (np - n_i^2) \quad (3.2)$$

where q is the elementary charge, ε is the dielectric constant, μ_n is the mobility of the electron, μ_p is the mobility of the hole, n and p represent the charge carrier densities of electrons and holes, and n_i is the intrinsic charge carrier concentration.

Trap-assisted recombination is a monomolecular recombination process.¹⁵⁶ In this type of recombination, either the electron or the hole becomes trapped in energy states within the bandgap. The rate of this process depends on the number of available trap sites. It is a non-radiative process and is commonly referred to as Shockley-Read-Hall recombination (R_{SRH}).^{163,164}

$$R_{SRH} = \frac{D_n D_p N_t (np - n_i^2)}{D_n (n + n_1) + D_p (p + p_1)} \quad (3.3)$$

where D_n and D_p are the probabilities per unit time of the electron and hole in the conduction and valence band at the empty and filled trap sites, and N_t is the electron trap density, $n_i^2 = n_1 p_1$, where n_i denotes the intrinsic carrier concentration.

The third type of non-geminate recombination is Auger recombination, also known as tri-molecular recombination, because it is a three-particle process.¹⁵⁶ In Auger recombination, an electron in the LUMO recombines with a hole in the HOMO, releasing energy that is transferred to a third electron, promoting it to a higher-energy state. The Auger recombination rate is described in Equation 3.4:

$$R_{Auger} = C_n n(np - n_i^2) + C_p p(np - n_i^2) \quad (3.4)$$

where, C_n and C_p are Auger coefficients.

3.2 Device configuration

The development of organic photovoltaics has led to several advances in device configurations, each with its own advantages and disadvantages. The different types of device configurations are shown in Figure 3.5.

3.2.1 Single-layer device configuration

This type of OPV cell is among the simplest. In this configuration, the active layer consists of one type of conjugated molecules sandwiched between two electrodes. While these solar cells typically have low PCE due to the lack of an exciton-dissociation interface, recent advances have brought the single-component active layer back into focus. The highest reported efficiency for single-component OSCs is over 11%.¹⁶⁵⁻¹⁶⁷

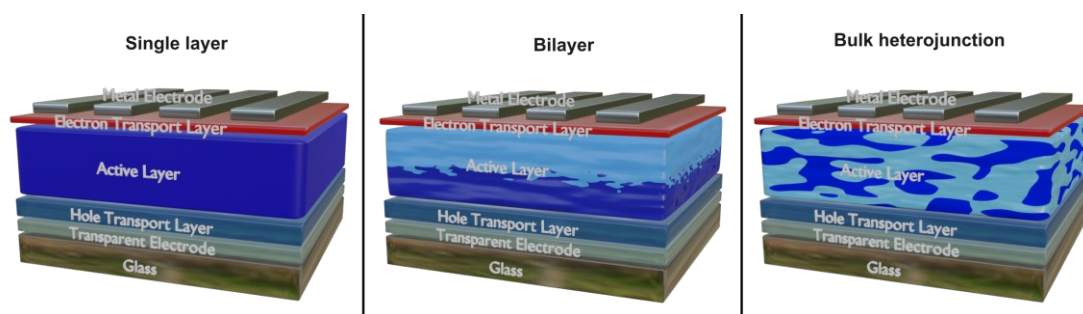


Figure 3.5: The device configurations of organic photovoltaic cells.

3.2.2 Bilayer device configuration

In a bilayer configuration, exciton splitting is more efficient due to the formation of a type-II heterostructure at the D/A interface, compared to a single-layer device architecture. The active layer consists of two organic semiconducting layers: a donor with a lower ionization potential and an acceptor with a higher electron affinity. The solution-processed bilayers are deposited via consecutive spin-coating steps using two different solutions or orthogonal solvents.¹⁶⁸ These two layers are sandwiched between the electron- and hole-transport layers, with electrodes on both sides. Compared to single-layer device architectures, bilayer devices exhibit higher PCE because the reduced exciton diffusion length required to reach the D/A interface enhances exciton dissociation efficiency. In recent years, the development of a pseudo-bilayer device architecture, based on D18/Y6 processed with chloroform, has achieved an efficiency of 17.94%.¹⁶⁹

3.2.3 Bulk heterojunction device configuration

In a bulk heterojunction (BHJ) device, the donor and acceptor materials are blended to form an interpenetrating, continuous network composed of donor-rich and acceptor-rich domains. During film formation, these domains are not fully phase-pure but instead form a finely phase-separated morphology governed by liquid-liquid phase separation during solvent evaporation. The intimate mixing of donor and acceptor materials results in a large D/A interfacial area, which enables efficient exciton dissociation. Because excitons are generated within a diffusion length of a D/A interface, exciton recombination losses are significantly reduced compared to single-layer architectures. Following charge separation, the interpenetrating donor- and acceptor-rich domains provide continuous percolation pathways for holes and electrons, respectively, thereby facilitating efficient charge transport to the electrodes. With the recent advances in NFAs and morphology control, the PCE of BHJ-based OSCs has now exceeded 20%.¹⁷⁰⁻¹⁷³

3.3 Solar cell parameters

The parameters used to characterize solar cell performance are open-circuit voltage (V_{OC}), short-circuit current density (J_{SC}), fill factor (FF), and peak power (P_{max}).

These parameters can be determined from the J-V characteristics under light illumination, as illustrated in Figure 3.6.

The power conversion efficiency (PCE) of the solar cell is defined as the ratio of the maximum generated power and the incident light power, as shown in Equation 3.5. The incident power is 1000 W/m² (AM 1.5 spectrum) at standard illumination conditions.

$$PCE (\eta) = \frac{P_{max}}{P_{inc}} = \frac{FF \times V_{OC} \times J_{SC}}{P_{inc}} \quad (3.5)$$

where, P_{max} is the maximum power, P_{inc} is the incident light power. The parameters are discussed in detail further.

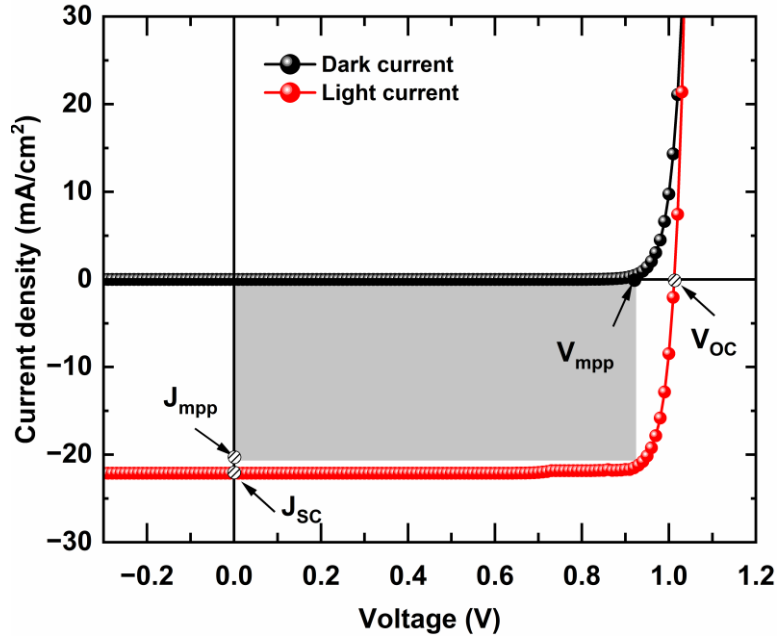


Figure 3.6: The current-voltage characteristics of the solar cell under dark and illuminated conditions, where J_{SC} is the short-circuit density, V_{OC} is the open-circuit voltage, J_{mpp} is the current density, and V_{mpp} is the voltage at the maximum power point.

3.3.1 Open-circuit voltage (V_{oc})

The open-circuit voltage is defined as the voltage at which no current flows through the external circuit. In open-circuit conditions, the rate of photogenerated charge carriers equals the recombination rate of the charges. The V_{OC} of the solar cell typically depends upon the difference between the HOMO of the donor and the

LUMO of the acceptor. Factors that can affect the V_{OC} of solar cells include morphology, interfacial disorder (D/A), orbital offsets, and charge recombination.^{174,175} One can choose a high-bandgap material to achieve a higher V_{OC} ; however, this will result in a smaller portion of the solar spectrum being absorbed, thereby lowering the J_{SC} of the solar cell. It is important to note that the material's bandgap can affect both the V_{OC} and J_{SC} , which, in turn, will impact the solar cell's performance.

3.3.2 Short-circuit current density (J_{SC})

The short-circuit current is defined as the current that flows through the external circuit when the solar cell is short-circuited. This is the maximum current that the device can generate under incident photon absorption (AM 1.5). In the ideal solar cell, the device current, i.e., the photogenerated carriers, equals the number of photons absorbed (AM1.5). However, this is not the case; some charge carriers recombine within the device. This is called recombination loss and decreases the short-circuit current density of the solar cell. Other factors can also affect the J_{SC} of devices, such as the absorption coefficients of the donor and acceptor materials, exciton dissociation, charge transport, and collection. The short-circuit current density (J_{SC}) also depends on the device's active area. The J_{SC} is defined as:

$$J_{SC} = q \int EQE(\lambda) \times AM1.5(\lambda) \times d\lambda \quad (3.6)$$

where q is the elementary charge, external quantum efficiency (EQE) is the number of charge carriers collected to the number of incident photons, and AM 1.5 is the solar spectrum.

3.3.3 Fill factor (FF)

The fill factor of a solar cell is the ratio of the product of J_{mpp} and V_{mpp} to the product of J_{SC} and V_{OC} .

$$FF = \frac{J_{mpp} \times V_{mpp}}{J_{SC} \times V_{OC}} \quad (3.7)$$

where J_{mpp} and V_{mpp} are the current and voltage at the maximum power point, and the J_{SC} and V_{OC} are the short-circuit current density and open-circuit voltage of the

solar cell (see Figure 3.6). The fill factor depends on the parasitic resistances, recombination, and charge-carrier mobility.^{176,177} This provides information about how efficiently the charge carriers can be extracted from the device.

3.4 Stability and lifetime of OSCs

Over the last decade, OSCs have exhibited a remarkable increase in PCE, with state-of-the-art devices now surpassing 20%. This rapid progress has been driven primarily by the development of a new class of NFAs capable of harvesting a broad portion of the solar spectrum, extending from the visible to the near-infrared. However, the commercialization of NFA-based OPVs remains constrained by their relatively short operational lifetimes and stability issues. For comparison, conventional crystalline silicon (c-Si) photovoltaic modules typically exhibit service lifetimes of 25-30 years.^{20,57-61} In contrast, the operational lifetime of OSCs is currently limited to only several years, which represents a major barrier to their large-scale commercialization.⁵⁷⁻⁵⁹

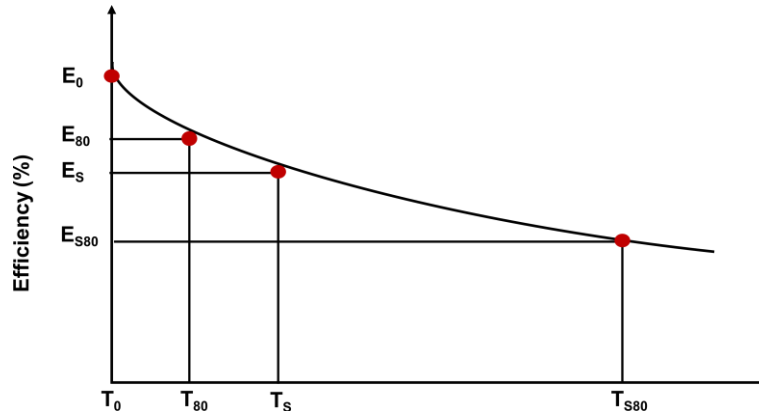


Figure 3.7: Schematic representation of a lifetime chart for the stability of organic solar cells.

In this section, the stability, lifetime, and challenges of the OSCs are addressed. Stability and lifetime are fundamental factors that determine the long-term performance of OSCs. Stability refers to a solar cell's ability to maintain its PCE under different environmental conditions, including light, temperature, air, and moisture. The lifetime parameter (T_{80}) of OSCs is defined as the time it takes for the solar cell's performance to degrade by 20%, retaining 80% of its initial efficiency.

After reaching T_{80} , the aging process often slows down, and the performance curve enters a more stable state. At this stage, when the degradation rate stabilizes, a new point (E_S) is defined. The stabilized lifetime (T_{S80}) is calculated when the device degrades by 20% compared to the new starting point (E_S). The device can continue operating with reduced efficiency for a longer period.^{178,179} Figure 3.7 shows how to define stability for OSCs. On the other hand, under illumination, the devices can degrade rapidly during the initial phase of device operation, known as the burn-in phase.¹⁷⁸ This time can range from a few hours to hundreds of hours.

The stability of OSCs is a critical aspect, as their photoactive materials are generally more susceptible to degradation. The stability of OSCs is commonly classified into four main categories: photostability, thermal stability, air and moisture stability, and chemical stability.^{68,69} Extrinsic factors, such as encapsulation quality, electrode oxidation, and deliberately applied stress during characterization, can significantly impact device stability. These aspects are addressed in more detail in the following sections.

3.4.1 Light and oxygen

Extrinsic factors such as light and oxygen play an important role in determining the stability of OSC devices. The O_2 -induced degradation can be reduced by encapsulating the device using glass and epoxy. However, this is difficult to completely avoid in the case of large-area devices fabricated on plastic substrates via roll-to-roll processing.⁸⁰ Oxygen can penetrate the encapsulation and reach the active layer, where it can react with the conjugated molecules, especially under illumination.¹⁸⁰ The penetration of oxygen can also affect the electronic structure of the active layer, even without illumination.⁸⁷ The details about the photooxidation processes are discussed in section 2.2. For instance, the NFAs ITIC-2F and ITIC-Th-based devices have shown a PCE of 8% with promising photostability under 1 sun illumination in a dry N_2 atmosphere. The extrapolated T_{80} lifetime was estimated to be around 10 years.⁵⁷ Moreover, devices based on ITIC, ITIC-M, and ITIC-DM experience an increase in energetic traps upon photodegradation, which leads to higher recombination rates, thereby decreasing

the J_{SC} and the FF. Li *et al.* reported that the intrinsic lifetime of NFA-based OSCs maintains 94% of their initial performance (1900 hours) in encapsulated devices tested under 1 sun intensity at 55°C. By introducing solution-processed buffer layers of IC-SAM on the cathode side to filter out UV irradiation, and C₇₀ on the anode side, respectively.⁵⁹ In addition, they performed accelerated aging tests at up to 27 suns of illumination at 65°C, and the extrapolated results indicated a potential lifetime of 30 years. Li *et al.* demonstrated that a highly efficient system based on PM6:Y6 increased the lifetime to over 10000 hours when the electron transport layer was replaced with Ir/IrO_x.⁵⁸ The T₈₀ lifetime of thermally evaporated DBP:C₇₀ with TPBi:C₇₀ as a cathode buffer layer under high temperature and very high illumination intensity was found to be 4.9×10^7 hours when devices were encapsulated in an inert atmosphere. However, the device efficiency remains low at about 6.7%.¹⁸¹ Recently, Baran *et al.* investigated the outdoor stability of Y-series NFAs under real-world operating conditions over 1000 hours of continuous illumination. Their results revealed that devices incorporating the Y12 acceptor exhibited superior stability compared to OSCs based on other Y-series NFAs. This enhanced photostability was attributed to the long internal side chain of Y12, which introduces a higher energetic barrier to cis-trans photoisomerization.¹⁸² Subsequently, they investigated the photostability of high-efficiency polymer donors PM6, D18, and PBDB-T blended with the Y6 non-fullerene acceptor. Under continuous illumination for 2000 hours, PBDB-T:Y6-based devices retained 84% of their initial performance, indicating superior photostability compared to the corresponding PM6:Y6 and D18:Y6 devices.¹⁰³

3.4.2 Interfacial instability

The device architecture of bulk-heterojunction (BHJ) OSCs is illustrated in Figure 3.1, where the photoactive layer is sandwiched between an electron transport layer and a hole transport layer. The interfaces between the active layer and the charge transport layers are critical for efficient charge extraction at the respective electrodes. In conventional OSCs (Figure 3.1a), the conducting polymer PEDOT:PSS is widely employed as the hole-transport layer due to its water-processability, environmental compatibility, high electrical conductivity, and good

optical transparency, all of which have contributed to its widespread use. However, OSCs using PEDOT:PSS as the hole-transport layer also face several challenges. The acidic nature of PEDOT:PSS can cause corrosion of the indium tin oxide (ITO) electrode, leading to indium diffusion into the PEDOT:PSS layer.^{183,184} Furthermore, the highly hygroscopic nature of PEDOT:PSS causes it to readily absorb moisture from the ambient environment, which can further compromise device stability and performance.^{76,77}

On the other hand, the most widely used electron transport layer in inverted device structures (Figure 3.1b) is zinc oxide (ZnO) and lithium fluoride (LiF), which is deposited on top of the transparent ITO. Another class of electron transport layers used in fullerene-based OSCs includes amine-containing small molecules and polymers such as polyethylenimine (PEI) or ethoxylated polyethylenimine (PEIE). However, the charge-transport properties of PEI or PEIE are less efficient than those of ZnO in NFA-based organic solar cells, leading to an S-shaped JV curve.^{185,186} In addition, the amine groups of PEI or PEIE can react with NFAs, potentially disrupting their electronic structures and intramolecular charge-transfer properties. Another widely used ETL is ZnO. The band gap of bulk ZnO is 3.3 eV, which means ZnO absorbs UV light to generate charge carriers. Under UV irradiation, ZnO generates electron-hole pairs by promoting electrons from the valence band to the conduction band. The photo-generated charge carriers can recombine, be trapped in surface defect states (oxygen vacancies), or participate in surface reactions, with defect trapping reducing recombination. Trapped carriers react with adsorbed H₂O to form a highly reactive hydroxyl radical, which subsequently degrades organic materials.^{67,90} There are several HTLs or ETLs used in OSCs, such as Molybdenum Oxide (MoO₃), Vanadium Oxide (V₂O₅), CuSCN, 2PACz, PDINN, PDINO, and PFN.^{136,138,187}

Chapter 4

Materials and experimental techniques

4.1 Materials

The photoactive materials investigated in this thesis include donor polymers, small-molecule acceptors (SMAs), and polymerized small-molecule acceptors (PSMAs).

4.1.1 Polymer PBDB-T donor

PBDB-T, or PCE12, is a conjugated polymer that acts as a light absorber and an electron donor. The molecular structure of PBDB-T is shown in Figure 4.1. The backbone consists of repeating D-A units, where D denotes the donor moiety and A denotes the acceptor moiety. The D unit consists of 2-alkylthiophenesubstituted benzo [1,2-b:4,5-b'] dithiophene (BDT) and 1,3-bis(thiophen-2-yl)-5,7-bis(2-ethylhexyl)benzo-[1,2-c:4,5-c']dithiophene-4,8 dione (BDD) serves as the A unit.¹⁸⁸ The PBDB-T polymer undergoes strong aggregation in chlorobenzene solution and disaggregates at elevated temperatures.¹⁸⁸ The PBDB-T used for the experiments has an Mw: ~65k and PDI: ~2.3, purchased from 1-Materials (CAS No: 1415929-80-4).

The full name of PBDB-T is Poly[(2,6-(4,8-bis(5-(2-ethylhexyl)thiophen-2-yl)-benzo[1,2-b:4,5-b']dithiophene))-alt-(5,5-(1',3'-di-2-thienyl-5',7'-bis(2-ethylhexyl)benzo[1',2'-c:4',5'-c']dithiophene-4,8-dione)].

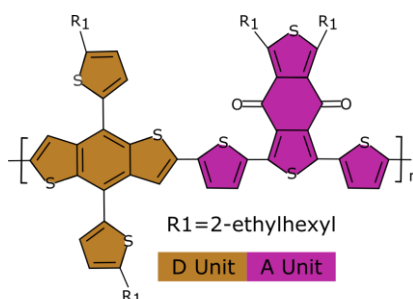


Figure 4.1: Molecular structure of PBDB-T.

4.1.2 Polymer PM6 donor

PM6 (PBDB-T-2F or PCE135) is an electron-donor conjugated polymer with a molecular structure similar to that of PBDB-T, but with a fluorinated thienyl benzodithiophene in the donor unit, as shown in Figure 4.2. The backbone consists of donor and acceptor moieties and exhibits strong absorption in the 300-685 nm range, with an optical bandgap of 1.80 eV.¹⁸⁹ Additionally, PM6 has been utilized in large-scale manufacturing processes.¹⁹⁰ The PM6 used for the experiments has an Mw: ~120k and PDI: ~2.5, purchased from 1-Materials (CAS No: 1802013-83-7).

The full name of PM6 is Poly[[4,8-bis[5-(2-ethylhexyl)-4-fluoro-2-thienyl]benzo[1,2-b:4,5-b']dithiophene-2,6-diyl]-2,5-thiophenediyl[5,7-bis(2-ethylhexyl)-4,8-dioxo-4H,8H-benzo[1,2-c:4,5-c']dithiophene-1,3-diyl]-2,5-thiophenediyl].

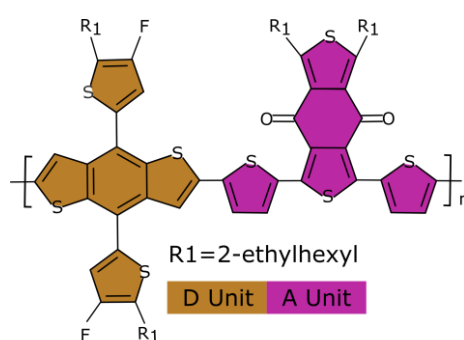


Figure 4.2: Molecular structure of PM6.

4.1.3 Polymer PTQ10 donor

The PTQ10 is an electron-donor polymer that consists of a thiophene ring as the electron donor unit and quinoxaline as the electron acceptor unit, as shown in Figure 4.3. The alkoxy side chain attached to the acceptor unit enhances solubility, while fluorination at the acceptor unit downshifts the HOMO level.¹⁹¹ Compared to other polymers, the simple structure of PTQ10 allows cost-effective mass production.¹⁹¹ This polymer can be dissolved in eco-friendly non-halogenated solvents such as o-xylene. The PTQ10 used for the experiments has an Mw: ~100k, PDI: ~2.5, purchased from 1-Materials (CAS No: 2270233-86-6).

The full name of PTQ10 is Poly [[6,7-difluoro[(2-hexyldecyl)oxy]-5,8-quinoxalinediyl]-2,5-thiophenediyl].

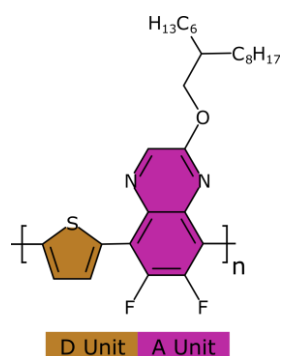


Figure 4.3: Molecular structure of PTQ10.

4.1.4 Small molecule acceptor Y5

Y5 is a small-molecule acceptor with a planar conjugated structure. Figure 4.4 shows the molecular structure of the Y5 acceptor. The BT (benzo[*c*][1,2,5]thiadiazole) unit is added to the central core.^{192,193} The unique A-D-A'-D-A structure provides a broad absorption spectrum ranging from 600 to 900 nm.⁹³ The Y5 has an optical band gap of 1.38 eV, a high absorption coefficient of 10^5 cm^{-1} , and an electron mobility of $10^{-4} \text{ cm}^2 \text{ V}^{-1} \text{ s}^{-1}$.¹⁹² The planar D-A'-D structure allows electron delocalization in the molecule. The Y5 used for the experiments has an Mw of 1379.97 g/mol and was purchased from Sigma-Aldrich (CAS No: 2304444-48-0).

The full name of Y5 is 2,2'-((2*Z*,2'*Z*)-((12,13-bis(2-ethylhexyl)-3,9-diundecyl-12,13-dihydro[1,2,5]thiadiazolo[3,4*e*]thieno[2'',3''':4',5']thieno[2',3':4,5]pyrrolo[3,2-*g*]thieno[2',3':4,5]thieno[3,2-*b*]indole-2,10-diyl)bis(methanylylidene))bis(3-oxo-2,3-dihydro1*H*-indene-2,1-diylidene))dimalononitrile.

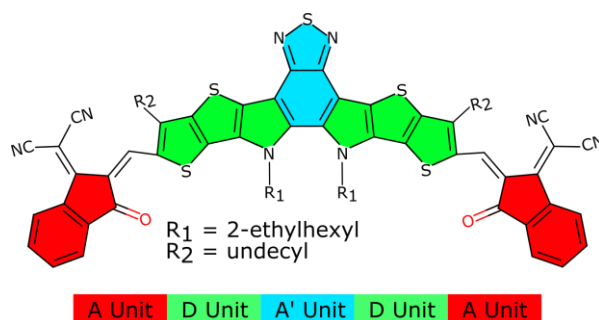


Figure 4.4: Molecular structure of Y5.

4.1.5 Small molecule acceptor Y6

Y6 is a small-molecule NFA with a structure similar to Y5, with two fluorine atoms at each of the end terminal positions of the acceptor units. The molecular structure is shown in Figure 4.5. The optical band gap Y6 is 1.33 eV with an absorption coefficient of 10^5 cm^{-1} .¹⁹⁴ Y6 has shown excellent photochemical and thermal stability.¹⁸² The Y6 used for the experiments has an Mw of 1451.93 g/mol, purchased from Sigma Aldrich and 1-Materials (CAS No: 2304444-49-1).

The full name of Y6 is 2,2'-((2Z,2'Z)-((12,13-Bis(2-ethylhexyl)-3,9-diundecyl-12,13-dihydro-[1,2,5]thiadiazolo[3,4-e]thieno[2'',3'':4',5']thieno[2',3':4,5]pyrrolo[3,2-g]thieno-[2',3':4,5]thieno[3,2-b]indole-2,10-diyl)bis(methanylylidene))-bis(5,6-difluoro-3-oxo-2,3-dihydro-1H-indene-2,1-diylidene))dimalononitrile.

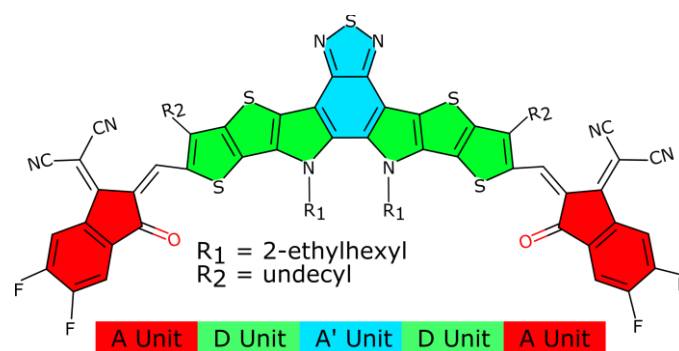


Figure 4.5: Molecular structure of Y6.

4.1.6 Polymer PF5-Y5 acceptor

PF5-Y5 is an alternating co-polymer that functions as an electron acceptor, as shown in Figure 4.6. The molecule is composed of Y5 units that act as an electron acceptor moiety, and thienyl-benzodithiophene (BDT-T) units that act as an electron donor moiety. The addition of the BDT-T donor unit to the Y5 unit up-shifted the LUMO energy level, thereby improving charge separation and transport properties in OSCs.¹⁴⁰ The material has an absorption coefficient of 10^5 cm^{-1} and a high electron mobility of $10^{-3} \text{ cm}^2 \text{ V}^{-1} \text{ s}^{-1}$ in film.^{140,195} The copolymer PF5-Y5 used for the experiments has an Mw of $\sim 13.6\text{k}$, Mn of $\sim 7\text{k}$, and a PDI of ~ 1.95 .

The full name of PF5-Y5 is Poly[(2,2'-((2Z,2'Z)-((12,13-bis(2-ethylhexyl)-3,9-diundecyl-12,13 dihydro[1,2,5]thiadiazolo[3,4e]thieno[2'',3'':4',5'']thieno[2',3':4,5] pyrrolo[3,2-g]thieno[2',3':4,5]thieno[3,2-b]-indole-2,10-diyl)bis(methanylylidene)) bis(3-oxo-2,3-dihydro-1H-indene-2,1-diylidene))dimalononitrile-alt-2,6-(4,8-bis(5-(2-ethylhexyl-3-hexyl)thiophen-2-yl)-benzo[1,2-b:4,5-b']dithiophene))]

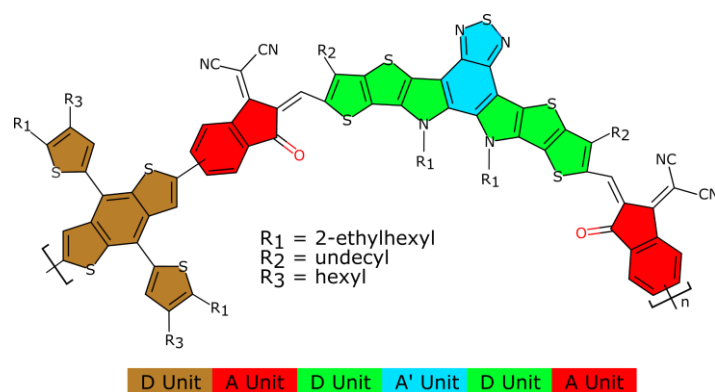


Figure 4.6: Molecular structure of PF5-Y5.

4.1.7 Polymer PYT acceptor

PYT is an alternating copolymer that functions as an electron acceptor. Min *et al.* were the first to design and synthesize the alternating copolymer.¹⁹⁶ The copolymer is composed of Y5 as an electron-deficient unit and thiophene as an electron-donor unit. Figure 4.7 shows the molecular structure of PYT. These polymer acceptors have a narrow optical band gap of 1.40-1.44 eV and a high absorption coefficient of 10^5 cm^{-1} .¹⁹⁶ The copolymer PYT used for the experiments has an Mw of ~40k, Mn of ~17.4k, and a PDI of ~2.3.

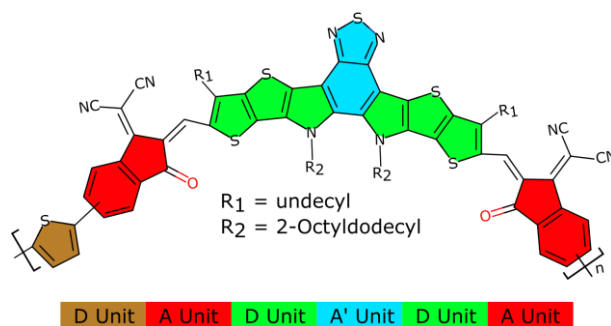


Figure 4.7: Molecular structure of PYT.

The full name of PYT is Poly[(2,2'-((2Z,2'Z)-((12,13-bis(2-octyldodecyl)-3,9-diundecyl-12,13dihydro[1,2,5] thiadiazolo[3,4e]thieno[2'',3'':4',5']thieno[2',3':4,5]pyrrolo[3,2-g]thieno[2',3':4,5]thieno[3,2-b]-indole-2,10-diyl)bis(methanylylidene))bis(3-oxo-2,3-dihydro-1H-indene-2,1-diylidene))dimalononitrile-alt-2,5-thiophene)].

4.2 Experimental techniques

This section provides a detailed description of the experimental techniques and device fabrication procedures used in this thesis. The thin film characterization methods include Ultraviolet-Visible-Near-Infrared Absorption Spectroscopy (UV-Vis-NIR), Fourier Transform Infrared Spectroscopy (FTIR), Photoluminescence Spectroscopy (PL), Atomic Force Microscopy (AFM), synchrotron radiation-based X-ray Photoelectron Spectroscopy (XPS), Ultraviolet Photoelectron Spectroscopy (UPS), and Near-Edge X-ray Absorption Fine Structure (NEXAFS) Spectroscopy.

4.2.1 Film preparation

For optical and surface characterization techniques, different substrates were used depending on the method. Glass substrates were used for UV-Vis-NIR spectroscopy, PL measurements, and AFM imaging. Si/SiO_x substrates were used for XPS, UPS, and NEXAFS measurements. For FTIR spectroscopy, KBr substrates were utilized. Before spin coating, the glass substrates were cleaned by sequential sonication in acetone and isopropyl alcohol for 20 minutes each. The n-type Si/SiO_x substrates were cleaned using the standard RCA cleaning method, excluding the HF step.¹⁹⁷ The KBr substrates were used without any additional treatment.

The blend solution is deposited onto the rotating substrate, which is then accelerated to a high angular speed, typically 1000-5000 rpm. This process results in a thin film with a final thickness of 80-150 nm. The process of spin coating is shown in Figure 4.8 (a-d).

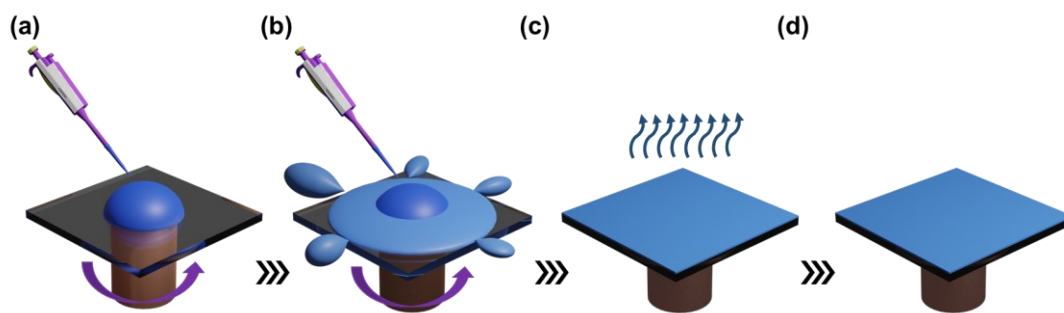


Figure 4.8: The process of spin coating (a) solution deposition, (b) thinning, (c) drying, and (d) thin film deposited.

The steps for spin coating are as follows:

1. The solution is dripped onto the substrate using a micropipette/syringe.
2. Once the solution is deposited, the substrate is rotated at a high angular speed. Centrifugal force drives the excess solution off the substrate, resulting in a uniform film coating.
3. After the film is coated onto the substrate, the solvent continues to evaporate.
4. In the final step, to remove any remaining solvent residue from the film, the spin-coated film is annealed, leaving the substrate with a thin solid film.

The sample preparation process is described in each paper separately.

4.2.2 Ultraviolet-visible-NIR absorption spectroscopy

When organic compounds are exposed to ultraviolet-visible-NIR radiation, they absorb energy, thereby exciting molecules from the ground state to higher-energy states. This process, known as *electronic excitation*, is depicted on the left side of Figure 4.9 (left). The ability of a molecule to absorb an incident photon depends on the specific electronic transitions available within the material. One such transition involves the excitation of electrons from σ -bonding orbitals to σ^* -antibonding orbitals. These σ - σ^* transitions typically require high energy and occur at wavelengths below 200 nm, depending on the molecular structure. Due to their high energy requirements, these transitions are generally observed in the far-ultraviolet (UV) region. Since UV-vis spectroscopy typically spans the near-UV and

visible regions (200 to 700 nm), $\sigma\text{-}\sigma^*$ transitions are not typically detected in conventional UV-vis absorption spectra. However, other electronic transitions, such as $n\text{-}\pi^*$ and $\pi\text{-}\pi^*$ transitions, are frequently observed in the UV-vis region. In $n\text{-}\pi^*$ transitions, an electron from a non-bonding orbital (n) is excited to an anti-bonding π^* orbital. In $\pi\text{-}\pi^*$ transitions, an electron is excited from a bonding π orbital to an anti-bonding π^* orbital. These transitions are common in organic compounds and are responsible for absorption in the UV-vis region. As the conjugation length of molecules increases (i.e., as the number of alternating single and double bonds increases), the energy gap between the highest occupied molecular orbital (HOMO) and the lowest unoccupied molecular orbital (LUMO) decreases. This reduction in the energy gap occurs due to the increased electron delocalization over the extended conjugated system.⁹⁷ As a result, the molecule can absorb lower-energy photons, leading to absorption at longer wavelengths, such as in the visible or near-UV regions. Figure 4.9 (right) shows the absorption spectra of donor PBDB-T and acceptor PF5-Y5.

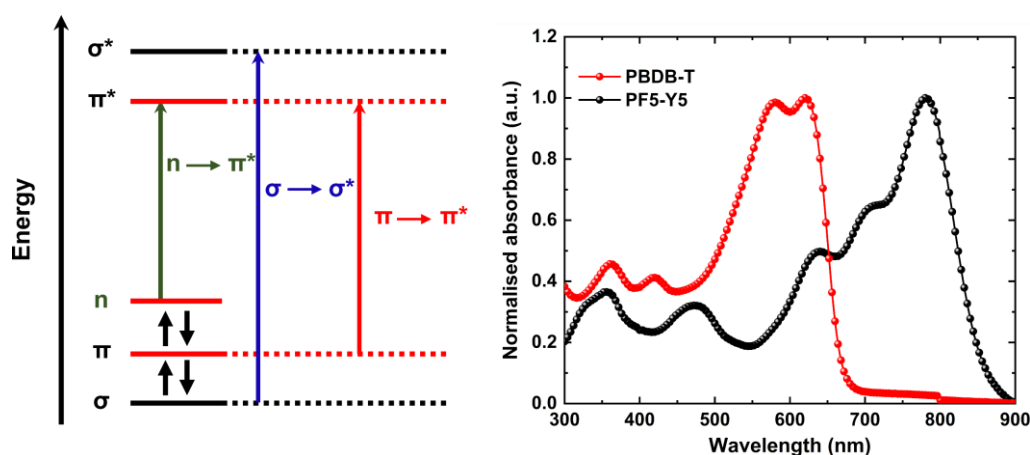


Figure 4.9: The electronic transitions from the ground state to the higher excited state (left). The absorption spectrum of PBDB-T and PF5-Y5 (right). The symbol represents the ground state σ , π as bonding orbitals, n as non-bonding orbitals, and the excited state σ^* , π^* as antibonding orbitals.

The schematic of the experimental setup is shown in Figure 4.10. The experimental setup consists of two light sources: a tungsten-halogen lamp (240-2700 nm) and a deuterium arc UV lamp (160-400 nm). The light passes through a small entrance slit, then through mirrors, and the rotating grating splits it into different wavelength

components. The beam splitter splits the light into two different paths so that part of the beam passes through the reference sample position and the other part passes through the sample position.

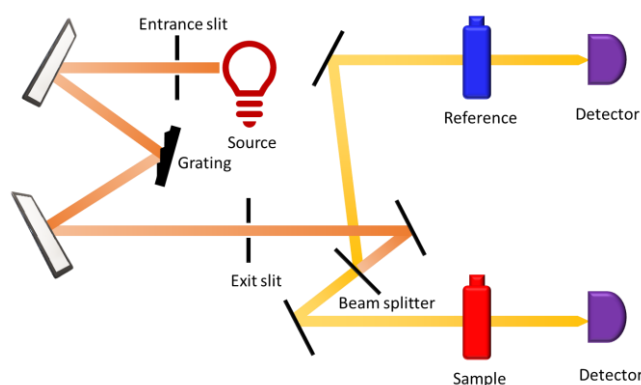


Figure 4.10: Schematic illustration of the ultraviolet-visible absorption spectrometer.

The intensity of the light (I) is measured with the photodetector and compared to the intensity of the incident light (I_0). The absorbance of the sample at a specific wavelength can be calculated as:¹⁹⁸

$$A(\lambda) = -\log \frac{I}{I_0} \quad (4.1)$$

UV-vis absorption spectroscopy was employed to record the absorption spectra of thin films, providing insight into the electronic transitions of the samples. This technique is widely used to evaluate how processing and environmental factors, such as aggregation, temperature, and humidity, affect the optical properties of materials. In this thesis, UV-vis spectroscopy was used to investigate organic thin films degraded for different exposure times under AM 1.5 illumination. All measurements were performed using a Cary 5000 UV-Vis-NIR spectrophotometer (Agilent Technologies, USA) equipped with Cary WinUV 6.1 software.

4.2.3 Fourier Transform Infrared Spectroscopy

Fourier Transform Infrared Spectroscopy (FTIR) is an effective method for probing the chemical composition of organic molecules by analyzing their vibrational modes. When infrared light (IR) is incident on an organic molecule, the molecule absorbs the light if the photon energy corresponds to the energy difference between two vibrational levels. Absorption occurs when IR light induces

a change in the molecule's net dipole moment, which is detected as an absorption signal. The vibrational frequency of a diatomic molecule (e.g., C=O) can be estimated by modeling the molecular bond as a harmonic oscillator, analogous to a spring. The vibrational frequency of the spring model can be represented using the formula:^{199,200}

$$\nu = \frac{1}{2\pi} \sqrt{\frac{k}{\mu}} \quad (4.2)$$

where, ν is the vibrational frequency, k is the force constant of the bond, and μ is the reduced mass of the two atoms in the molecule ($\mu = \frac{m_1 m_2}{m_1 + m_2}$), m_1 and m_2 are the masses of the atoms.

The frequency of diatomic molecules depends on bond order, from single to double to triple bonds. As spring constantly increases, the vibrational frequency increases. The vibrational frequency of the molecules also depends upon the mass of the atoms.²⁰⁰ The several vibrational modes of the triatomic molecules are shown in Figure 4.11. The above equation 4.2 can also be expressed as:

$$\bar{\nu} = \frac{1}{2\pi c} \sqrt{\frac{k}{\mu}} \quad (4.3)$$

where, $\bar{\nu} = 1/\lambda$ represents the wavenumber and $c = \nu\lambda$ represents the speed of light. The vibrational modes of simple molecules are observed in the mid-IR range (4000-400 cm^{-1}) and can be used to identify chemical bonds.

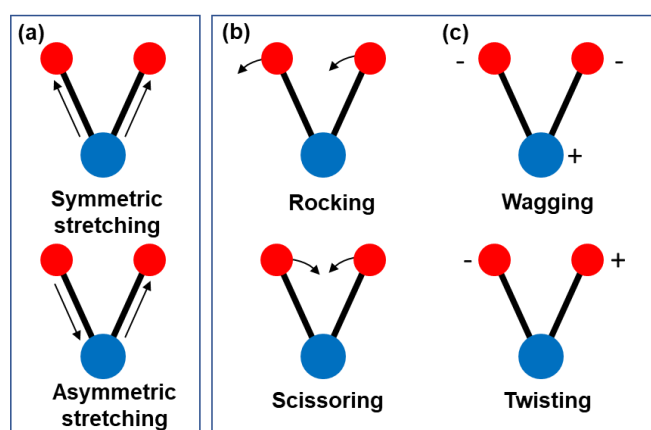


Figure 4.11: Illustration of different modes of vibration for a triatomic molecule: (a) Stretching modes, (b) in-plane modes, and (c) out-of-plane modes.

The schematic of the FTIR spectrometer is shown in Figure 4.12. The main component of the FTIR spectrometer is a *Michelson interferometer*. It consists of two mirrors, M1 and M2. They are mounted at 90° with respect to one another. The M1 mirror is stationary, and M2 is movable in the direction of the beam, which can move precisely and accurately within a few millimeters. When IR light is incident on the beam splitter, 50% is reflected, and 50% is transmitted. The reflected beam back from the mirrors M1 and M2 recombines at the beam splitter and interferes. The optical path difference between the two light beams results in constructive or destructive interference at the detector. The sample is placed between the interferometer and the detector. Considering the IR source as a monochromatic beam of light of wavelength (λ) and movable mirror M2, the intensity of the beam can be given as:

$$I(x) = \frac{1}{2}I(\bar{\nu})\cos(2\pi\bar{\nu}x) \quad (4.4)$$

where $I(\bar{\nu})$ is the intensity at frequency $\bar{\nu}$.

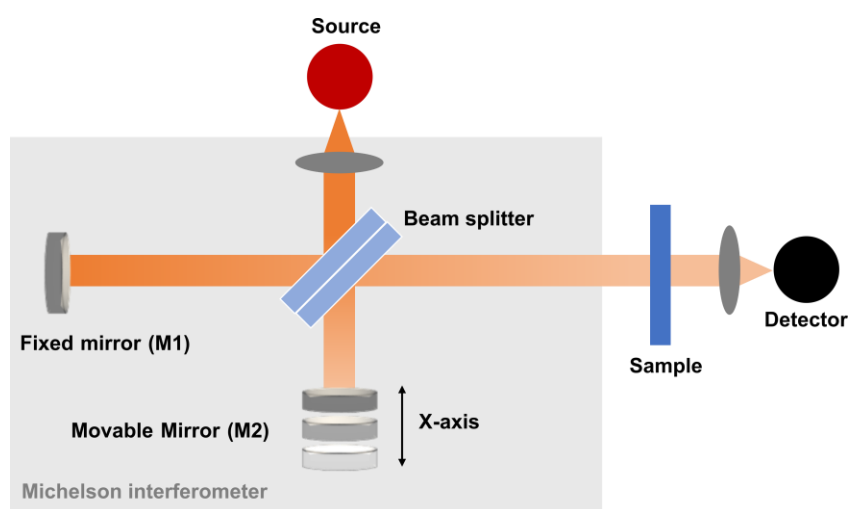


Figure 4.12: Schematic of FTIR spectrometer.

For a *continuous* source of IR radiation, all wavelengths of light pass through the interferometer. At the position $X=0$ (when the path difference between the two beams in the interferometer is zero), all the wavelengths of light will be in phase, resulting in constructive interference. This condition produces the maximum intensity of the signal at the detector. At any movement of the mirror M2, it gives

a complex interference pattern, and the detector records the resulting interferogram, which contains the combined contributions of all wavelengths. The corresponding IR spectrum is then obtained by applying a Fourier transformation to the interferogram.²⁰¹ The obtained IR spectra help to identify the chemical bonds within the molecules by analyzing the specific absorption peaks corresponding to different vibrational modes. Each type of chemical bond (e.g., C-H, O-H, C=O) has a characteristic vibrational frequency, which results in absorption at specific wavelengths of infrared light. The functional groups and chemical structure of the molecule can be identified by comparing the absorption intensity peaks and frequencies.^{202,203} The instrument used for IR measurements in this work is an INVENIO S spectrometer (Bruker, France), purged with dry air, working with OPUS 8.5 software.

4.2.4 Atomic force microscopy

Atomic Force Microscopy (AFM) is a widely used scanning probe microscopy technique for imaging surface morphology. In AFM, a flexible cantilever with a sharp tip is scanned across the sample surface, where it interacts with the surface at the nanoscale. The laser hits the back side of the cantilever, and the deflection of the cantilever is measured by detecting the position of the reflected laser beam with a sensitive photodiode detector, as shown in Figure 4.13. The interaction between the tip and the sample surface is used to map the sample's topography at nanometer resolution.

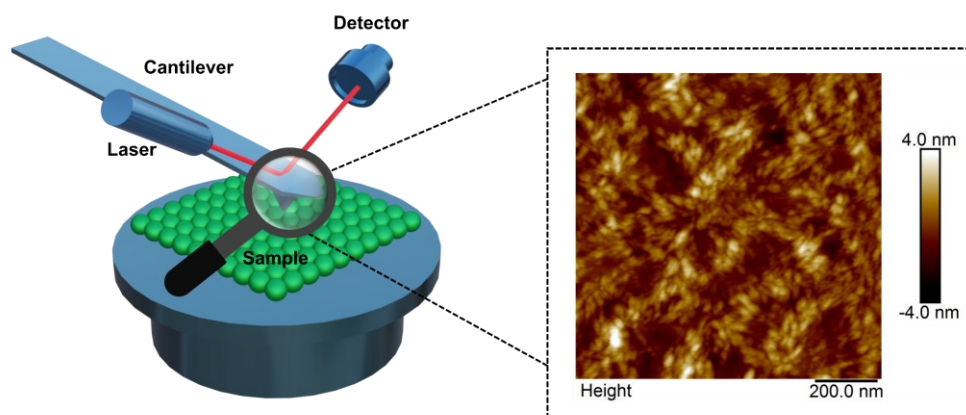


Figure 4.13: Schematic of AFM setup.

The interaction between the tip and the sample surface can be described by the Lennard-Jones potential:²⁰⁴

$$U(r) = 4\epsilon \left[\left(\frac{\sigma}{r} \right)^{12} - \left(\frac{\sigma}{r} \right)^6 \right] \quad (4.5)$$

where $U(r)$ is the interaction potential, ϵ is the depth of the potential well, r is the distance between the tip and the sample, σ is the distance where the potential is zero. The positive term in equation 4.5 represents the repulsive force interaction, while the negative term corresponds to the attractive force interaction. The Lennard-Jones potential is shown in Figure 4.14.

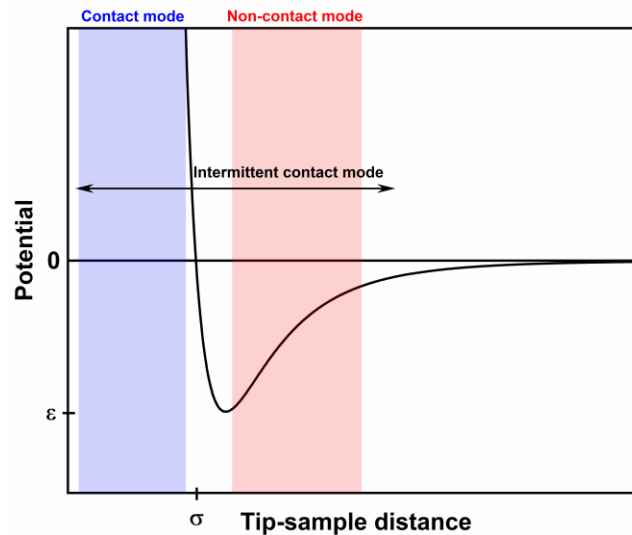


Figure 4.14: Lennard-Jones potential curve. There are several different types of modes being used in AFM: contact mode, intermittent contact/tapping mode, and non-contact mode.

In contact mode, the tip is in physical contact with the sample surface. The laser light is incident on the back side of the cantilever. The sample topography induces a vertical deflection of the cantilever, and the cantilever's motion is detected by the photodiode. The sample surface exerts a repulsive force on the cantilever tip at a short interatomic distance between them. To maintain the cantilever's constant deflection, the deflection set point is held constant via the feedback loop circuit, which responds to z-axis changes. Contact mode is typically used to measure hard, relatively flat sample surfaces due to the strong force interaction between the sample and the cantilever tip. However, a drawback of contact mode is that the cantilever

tip or the sample surface can be damaged by the continuous, strong force applied during scanning, particularly when dealing with soft or delicate materials.

Intermittent or tapping mode is commonly used to measure soft materials, such as polymers. In this mode, the cantilever tip oscillates near its resonance frequency. During scanning, the tip intermittently contacts the sample surface. The amplitude of the AFM tip oscillation in tapping mode can be controlled by adjusting the drive voltage applied to the piezoelectric actuator that drives the cantilever. The feedback loop in AFM controls the piezoelectric actuator to maintain the desired distance between the sample and the cantilever tip. Compared to contact mode, tapping (or intermittent) mode significantly reduces the risk of damage to both the sample and the tip.

In non-contact mode, the tip oscillates near the sample but never touches the sample. When the cantilever approaches the sample surface, the resonance frequency shifts due to van der Waals and other long-range forces acting between the tip and the sample. So, the oscillation is slightly above the resonance frequency, so it never makes physical contact with the sample surface. However, the oscillation can be maintained with proper sample and tip distance. The energy dissipation into the sample in non-contact mode is much lower than in all other modes of operation.

In this work, tapping mode AFM was used to examine the morphology and thickness of organic thin films. The measurements were conducted using a Nanoscope 8 Multimode AFM (Bruker, France) equipped with an Antimony (n) doped Si cantilever tip manufactured by Bruker (Model: RTESPA-300). The details about the cantilever tip are as follows: resistivity (ρ) = 0.01 - 0.025 Ω -cm, Coating: Front side (None), Back side (Reflective Al), thickness (t) = 3.4 μ m, length (l) = 125 μ m, width (w) = 40 μ m, frequency (f) = 300 kHz, spring constant (kN) = 40 N/m.

4.2.5 Photoluminescence Spectroscopy

Photoluminescence (PL) spectroscopy is an analytical technique used to investigate the electronic and optical properties of materials. In this process, incident photons

promote electrons from the ground state to higher electronic excited states; when these excited states relax back toward the ground state, light can be emitted, as illustrated in the Jablonski diagram in Section 3.1.2.

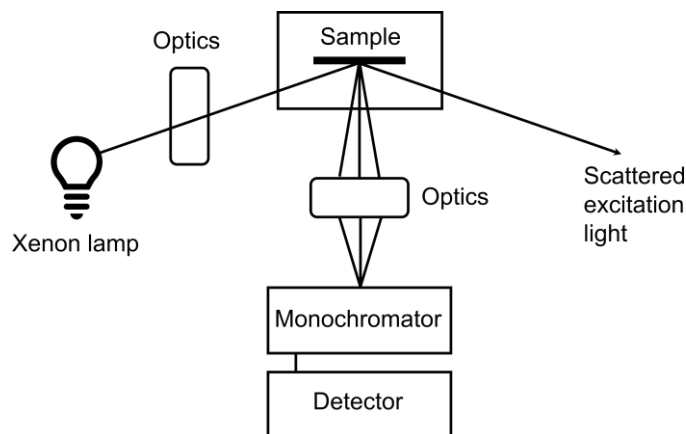


Figure 4.15: Schematic of the photoluminescence measurement system.

Within the sample, this relaxation can proceed via radiative or non-radiative pathways. Radiative relaxation gives rise to photoluminescence, which is generally classified as either fluorescence or phosphorescence. Fluorescence is a fast process, typically originating from the radiative decay of singlet excited states, with characteristic lifetimes on the order of $\sim 10^{-9}$ - 10^{-6} s, whereas phosphorescence is a slower process, usually associated with radiative decay from triplet states, with lifetimes ranging from about 10^{-6} s to longer than 1 s. The schematic of the photoluminescence setup is shown in Figure 4.15. The PL measurements were performed using a Fluorolog system from Horiba (Japan) equipped with the FluorEssence software.

4.2.6 Synchrotron radiation

The development of X-ray-based characterization techniques can be traced back to the discovery of X-rays by W. Röntgen in 1895, after which X-rays rapidly became a cornerstone of materials research.²⁰⁵ Synchrotron radiation is primarily distinguished by its ability to generate highly collimated, narrow X-ray beams with exceptionally high intensity.²⁰⁶ In these modern facilities, X-rays are produced by relativistic electrons circulating in storage rings and emitting radiation when their

trajectories are bent by magnetic fields. The performance of an X-ray source is not fully described by its total photon flux alone; instead, the more relevant parameter is the brilliance, which reflects how concentrated the photon beam is in terms of space, angle, energy bandwidth, and time. It is defined as:²⁰⁷

$$\textit{Brilliance} = \frac{\textit{photons/second}}{\textit{mrad}^2 (\textit{mm}^2 \textit{ source area}) (0.1\% \textit{ bandwidth})} \quad (4.6)$$

The emitted radiation is confined to a narrow cone around the instantaneous direction of motion, roughly tangent to the electron orbit, with an angular divergence θ that can be expressed as:

$$\theta \sim \frac{1}{\gamma} \quad (4.7)$$

where γ is the Lorentz factor.

Figure 4.16 illustrates the components of a synchrotron radiation facility.²⁰⁷ In such systems, electrons are first generated in an electron gun through thermionic emission from a heated cathode and subsequently accelerated to relativistic energies using a linear accelerator (linac) to about 100 MeV. After this initial acceleration stage, the electron bunches are injected into a booster ring, where their kinetic energy is further increased to the level required for storage. The high-energy electrons are then transferred into the storage ring, which, in modern synchrotrons, is composed of multiple straight sections connected by curved segments, giving the ring a polygonal geometry rather than a perfect circle. The electron trajectory is controlled by dipole magnets positioned at the curved sections, which bend the beam to maintain a closed orbit. As electrons traverse these magnetic fields and undergo continuous changes in direction, they emit synchrotron radiation, which forms the basis for the intense, highly collimated X-ray beams used in advanced experiments.

As electrons circulate in the storage ring, synchrotron radiation is emitted, leading to a continuous energy loss. If this energy loss were not compensated, the electrons would gradually drift away from the stable orbit and ultimately be lost through collisions with the vacuum chamber walls. Energy stability is therefore ensured by

radiofrequency (RF) cavities, which restore the lost energy by exposing the electrons to oscillating electromagnetic fields synchronized with their revolution frequency. The electron beam is structured into distinct bunches rather than forming a continuous stream. Due to small energy differences, electrons within a bunch interact with the RF field at slightly different phases, resulting in differential acceleration that stabilizes the longitudinal bunch structure and preserves a nearly uniform velocity. Transverse confinement and beam quality are maintained using magnetic optics: quadrupole magnets focus the beam in the horizontal and vertical directions, while sextupole magnets compensate for chromatic effects arising from energy-dependent focusing, thereby ensuring stable beam dynamics.

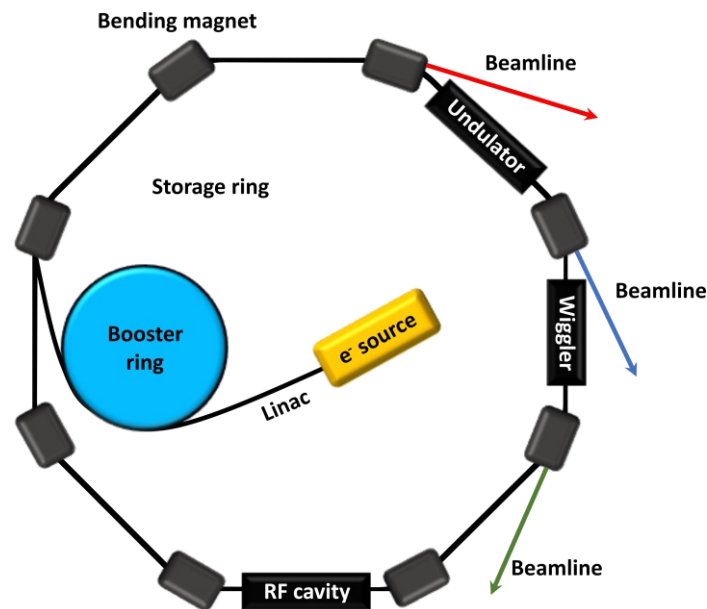


Figure 4.16: Schematic layout of a synchrotron and highlights several key components. Electrons are first generated and subsequently accelerated before being injected into the storage ring. As the electrons circulate, synchrotron radiation is produced whenever their trajectory is deflected, either by bending magnets or by dedicated insertion devices installed in the straight sections of the ring. reproduced from reference²⁰⁷

Synchrotron radiation is produced not only when electrons are deflected by bending magnets, but also through specialized magnetic structures placed in the straight sections of the storage ring, known as insertion devices. These devices generate a periodically varying magnetic field that forces the electron beam to undergo transverse oscillations as it propagates forward. If the magnetic field strength is high, the electrons experience large angular deflections, and the device operates in the wiggler regime. In this case, radiation is emitted at each oscillation, leading to a

substantial increase in photon flux compared to a single bending magnet, while the resulting spectrum remains relatively broad. When the magnetic field is weaker, the electron oscillations are confined within the natural angular spread of the emitted radiation, and the device functions as an undulator. Under these conditions, radiation emitted at successive oscillations interferes coherently, resulting in constructive interference at specific wavelengths. As a result, the emitted spectrum consists of intense, narrow energy peaks rather than continuous distribution. The photon energy of these peaks can be adjusted by varying the magnetic field strength, typically by changing the gap between opposing magnet arrays. Radiation generated in bending magnets, wigglers, or undulators is extracted tangentially from the storage ring and transported through dedicated beamlines.

4.2.7 Photoelectron spectroscopy

Photoelectron spectroscopy is a surface-sensitive technique based on the photoelectric effect. In the 1950s, Swedish physicist Kai Siegbahn developed this technique to determine the chemical composition of surfaces, for which he was awarded the Nobel Prize in 1981.²⁰⁸ Depending on the excitation source, photoelectron spectroscopy has two distinct methods. In Ultraviolet Photoelectron Spectroscopy (UPS), ultraviolet photons are used for excitation. When X-ray photons are used, the technique is called X-ray Photoelectron Spectroscopy (XPS) or Electron Spectroscopy for Chemical Analysis (ESCA). The schematics of UPS and XPS processes are shown in Figure 4.17. In XPS, X-ray photons are absorbed by core-level electrons, which are excited and emitted from the sample. The kinetic energy of the emitted electrons, the photoelectrons, is measured.

The electron binding energy is then calculated from the measured kinetic energy and the photon energy, as shown in Equation 4.8.

$$E_B = h\nu - E_k - \varphi_s \quad (4.8)$$

where, E_B is the binding energy of the electron, E_k is the kinetic energy of the emitted electron, $h\nu$ is the photon energy of the X-ray incident on the sample, and φ_s is the work function of the sample in electrical contact with the detector.

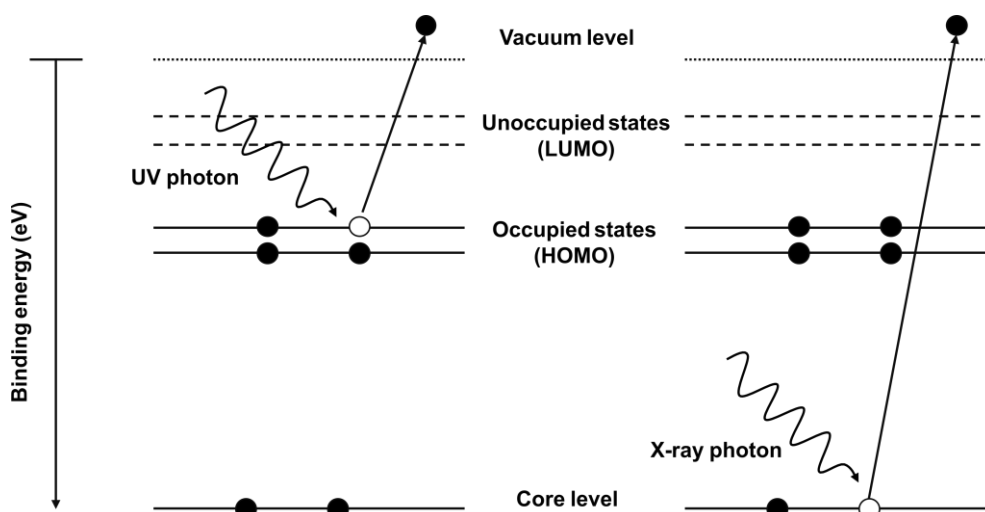


Figure 4.17: Schematic of UPS and XPS process.

The photoelectron emitted from the sample surface enters the concentric hemispherical analyzer, where its kinetic energy is measured. The outer hemisphere of the analyzer is negatively charged, while the inner hemisphere is positively charged. The applied electric potential can be adjusted to the analyzer, allowing a specific range of electron kinetic energies to pass through it. Ultimately, the electron reaches the detector after passing through the exit slit. The sample and the spectrometer are electrically connected, ensuring that the sample's Fermi level is aligned with the detector's Fermi level.

UPS is used to measure the energy of valence-band states in semiconductors or the work function of metallic surfaces. For UV radiation, a helium (He I) source with an energy of 21.22 eV is typically used (in-house). For both XPS and UPS, the samples are prepared on a conducting substrate. X-ray Photoelectron Spectroscopy (XPS) enables the precise measurement of the binding energy of core electrons associated with different atoms, such as carbon. This technique aids in identifying their chemical environments (e.g., C-C, C=C, C=O) by detecting chemical shifts arising from variations in the chemical environment. On the other hand, UPS spectra provide insights into the sample's valence states, facilitating studies of doping, energy-level alignment, and degradation.

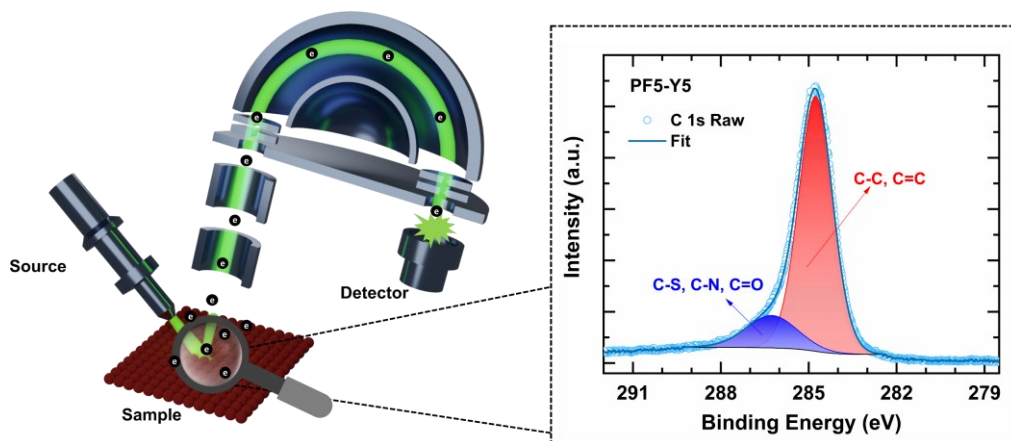


Figure 4.18: Schematic representation of the XPS system and the C 1s spectra of PF5-Y5.

In this work, XPS and UPS measurements were performed using both in-house and synchrotron-based instruments. An in-house XPS system typically consists of a measurement chamber with an ultra-high vacuum system ($\sim 10^{-9}$ mbar), X-ray anode source Mg $K\alpha$ (1253.6 eV) or Al $K\alpha$ (1486.6 eV), and an electron analyzer.²⁰⁹ The UHV system (ÓMICRON, Germany) is equipped with a non-monochromated Al $K\alpha$ X-ray source (PSP Vacuum Technology-TX400/2, UK), operated at 150 W, and a He I UV-source (HIS 13-FOCUS, Germany). A Scienta SES 100 electron analyzer was used with pass energies of 50 eV for XPS and 2 eV for UPS. The pressure for the XPS was 1×10^{-9} mbar and for UPS 2×10^{-7} mbar. Synchrotron-based radiation with high-resolution core-level XPS was performed at the FlexPES beamline of the synchrotron facility MAX IV in Lund, Sweden, using de-focused light and a Scienta DA-30L (W) electron analyzer at normal emission with a pass energy of 50 eV, under a base pressure of 3×10^{-10} mbar. Specific photon energies were used for different core-level measurements.

4.2.8 Near-Edge X-Ray Absorption Fine Structure (NEXAFS) spectroscopy

Near-edge X-ray absorption fine structure (NEXAFS) spectroscopy uses soft X-rays, typically with photon energies in the 100-1000 eV range, to probe unoccupied electronic states.^{210,211} In a typical NEXAFS experiment, the X-ray energy is scanned across a selected absorption edge, corresponding with a core level (for example, the 1s or K-edge), and the resulting resonant transitions into π^* and σ^*

antibonding molecular orbitals near that edge are detected. Thus, NEXAFS provides detailed information on the X-ray absorption fine structure close to an element-specific absorption edge. This technique has been widely used to characterize small molecules and thin polymer films.^{212,213}

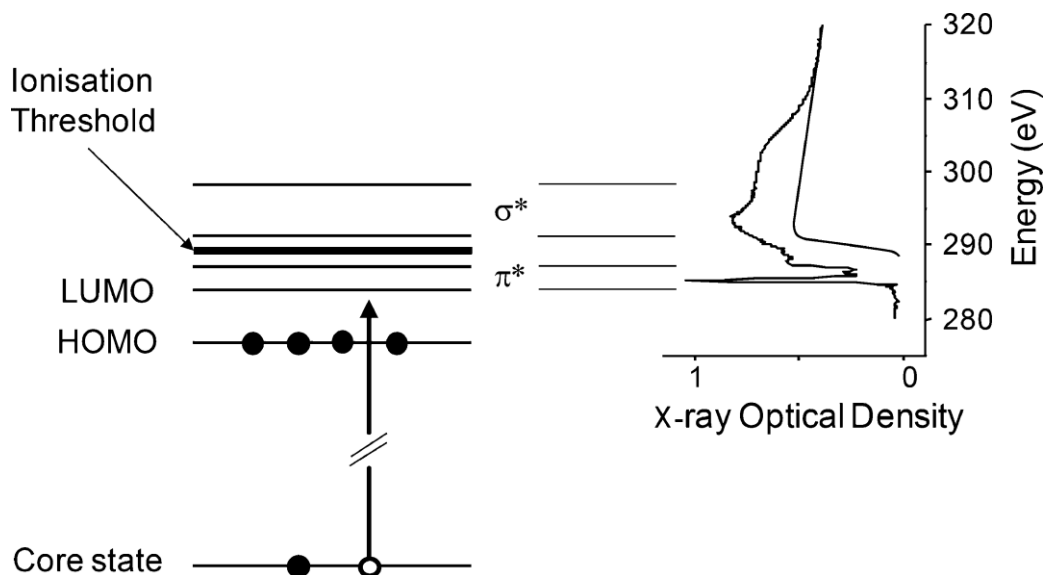


Figure 4.19: Schematic illustration of the molecular energy levels and the transitions from core levels into antibonding and continuum states. The corresponding NEXAFS spectrum arising from these transitions is shown on the right-hand side of the figure.²¹²

NEXAFS experiments are typically carried out under ultra-high-vacuum conditions, and the spectra can be collected using several detection modes, most commonly total electron yield (TEY), partial electron yield (PEY), and partial fluorescence yield (PFY), as shown in Figure 4.20.

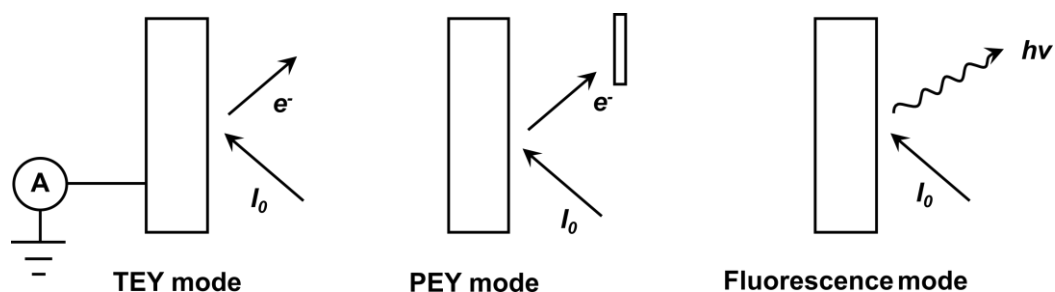


Figure 4.20: Schematic of the different NEXAFS measurement techniques in different modes.

In PEY mode, the technique provides high surface sensitivity, with an electron escape depth in the order of 1-3 nm. The signal originates from electrons emitted

from the sample's surface and is detected using a channeltron. A retarding voltage is applied to the channeltron to suppress low-kinetic-energy background electrons, thereby enhancing the signal-to-noise ratio. In contrast, TEY is sensitive to a somewhat larger electron escape depth (approximately 3-5 nm). Here, one measures the drain current required to neutralise the positive charge left behind as electrons escape the sample. PFY detection records the X-ray-induced fluorescence emitted from the sample following core-level excitation and is intrinsically more bulk-sensitive than electron-yield modes, as the photon escape depth is significantly larger than that of electrons. NEXAFS spectra can also be used to extract information about the surface chemical composition of polymer blend films. This is commonly done by modelling the blend spectrum as a linear combination of the spectra of the corresponding neat components. NEXAFS measurements are typically performed at an incidence angle of $\sim 55^\circ$, the so-called magic angle, at which contributions from molecular orientation effects are minimized.

In addition, NEXAFS spectroscopy can be used to determine molecular orientation at the surface of a film. The intensity of the resonant features near a given absorption edge depends on both the orientation and magnitude of the corresponding transition dipole moment, O , relative to the electric field vector, E , of the incident linearly polarised X-ray beam:

$$I \propto |E \cdot O|^2 \propto \cos^2 \delta \quad (4.9)$$

where δ is the angle between E and O .

Molecular orientation can influence the charge transport properties of OSCs.^{214,215} In the edge-on orientation, the π -conjugated backbone and side chains of the organic molecule are aligned perpendicular to the substrate plane. On the other hand, in the face-on orientation, the π -conjugated backbone and side chains of the organic molecule are aligned parallel to the substrate plane. In OSCs, with a face-on orientation, the charges can travel along the chain and the conjugated plane. In contrast, for the edge-on orientation, insulating side chains may negatively affect the charge transport.

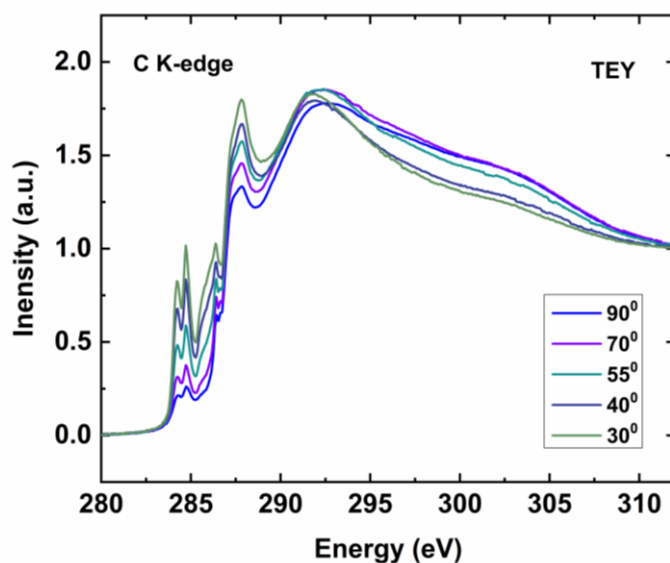


Figure 4.21. Angular dependent NEXAFS spectra at the carbon K-edge of a PF5-Y5 film processed from chlorobenzene solutions. The angle given in the legend is the angle of incidence of the X-ray with respect to the sample surface.

In aromatic polymers, for example, the C 1s $\rightarrow \pi^*$ resonance exhibits its maximum intensity when the electric field vector is aligned such that it probes the orbital component oriented normal to the conjugated ring plane, whereas the C 1s $\rightarrow \sigma^*$ resonance is strongest when the electric field vector is aligned along the σ -bond axis. In practice, NEXAFS spectra are recorded at several angles of incidence, typically from a shallow angle of 20° to normal incidence (90°) with respect to the substrate plane. Figure 4.21 depicts the NEXAFS spectra at the carbon K-edge of PF5-Y5 films processed from a chlorobenzene solution. The absorption intensities at ~ 284.3 eV and ~ 284.9 eV increase as the X-ray incidence angle decreases, indicating a pronounced angular dependence of the π^* resonances. This behavior is characteristic of a face-on molecular orientation, indicating that the PF5-Y5 film predominantly adopts a face-on orientation relative to the substrate.²¹⁵ The spectra are normalized so that the pre-edge value is 0 and the post-edge value is 1. In this thesis, PyMca 5.8.1 was used to analyze the NEXAFS results.

NEXAFS can also be used to probe molecular changes in the LUMO of organic materials upon photodegradation. For instance, it has been shown that exposure to light decreases the conjugation character in PC₆₀BM and C₆₀.¹¹⁷ The C1s NEXAFS

spectra measured in TEY mode of (a) pristine TQ1, (b) pristine N2200, and (c) TQ1:N2200 (2:1) blend thin films measured after exposure in air to AM 1.5 light for different lengths of time (Figure 4.22).

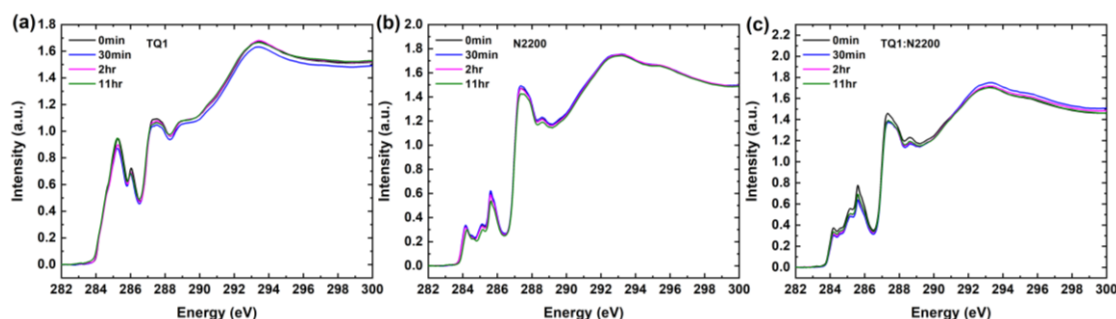


Figure 4.22: *C1s* NEXAFS spectra in TEY mode of TQ1, N2200, and TQ1:N2200 (2:1) films after different photodegradation times in air (0 min, 30 min, 2 hr, and 11 hr).

No significant changes in the spectra are observed as a function of photodegradation time for all the films. In the case of TQ1, C1s NEXAFS spectra showed absorption resonances at 285.3 eV and 286 eV corresponding to C1s - π^* transitions, while the peak at 293.3 eV is assigned to a C1s - σ^* transition.²¹⁶ In the case of N2200, which contains both naphthalene diimide (NDI) derivative as the acceptor unit and thiophene as the donor unit in the polymer backbone, the absorption peaks at 284.2eV and 285.6eV correspond to C1s - π^* transitions from the acceptor NDI monomer and the peaks located at 284.6eV and 285.1eV are assigned to C1s - π^* transitions from the donor thiophene units, while the peak at 293.2eV is from C1s - σ^* transitions.^{213,217} Also, the blend film exhibits good photochemical stability, as indicated by the lack of substantial changes in its C1s NEXAFS spectra over time. We note that the C1s NEXAFS spectra of the TQ1:N2200 (ratio 2:1) blend resemble those of pristine N2200, with small contributions from TQ1, resulting in a difference in relative peak intensities in the π^* region. This significantly lower contribution of TQ1 in the TQ1:N2200 C1s NEXAFS spectrum compared to what is expected from a blend ratio 2:1 indicates that the top surface is depleted of TQ1. This surface segregation can be explained by the differences in surface energy between the components. The surface energies of TQ1 and N2200 are 29 mNm⁻¹ and 24.58 mNm⁻¹,²¹⁶ respectively, and therefore

N2200 will accumulate at the top surface of the blend film. Surface energy minimization at the top surface has previously been reported for several other systems.²¹⁸⁻²²⁰

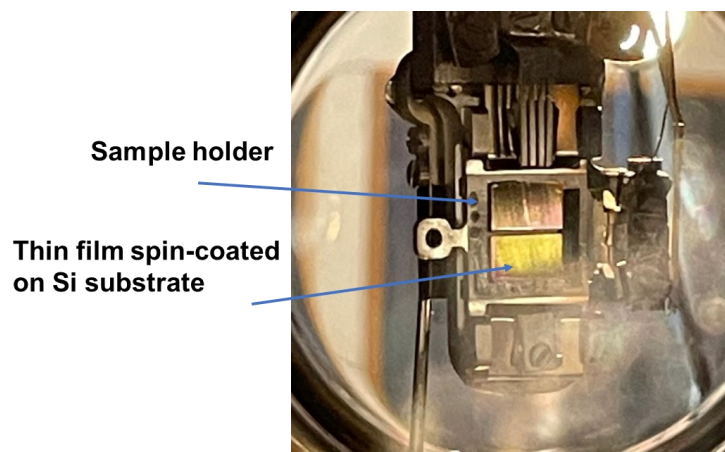


Figure 4.23: The sample holder with spin-coated thin films of PM6:Y6 on a Si/SiO_x substrate for NEXAFS measurements done at the FlexPES beamline at MAXIV, Lund.

For NEXAFS measurements, thin films were prepared by spin-coating the samples onto highly conductive, bare Si/SiO_x substrates, using the same spin-coating conditions as those employed in device fabrication (see section 4.3). Following deposition, the coated wafers were cut into smaller pieces (approximately 5 mm × 10 mm) and fixed to a conductive sample holder using double-sided carbon tape to ensure good electrical contact during the measurements, as shown in Figure 4.23. NEXAFS measurements were performed at the FlexPES beamline, at the Swedish National Synchrotron Facility, MAX IV, in Lund, Sweden, and the PIRX Beamline at the National Synchrotron Radiation Centre SOLARIS, in Kraków, Poland.

4.3 Device fabrication

In this section, the fabrication of the devices and the corresponding electrical characterization techniques are described, including current-voltage (I-V) measurements, External Quantum Efficiency (EQE), and Photo-CELIV.

A typical OSC employs sandwich-type architecture, with a photoactive layer sandwiched between two electrodes. In this thesis, the OSCs were fabricated using

a conventional device structure with the layout: bottom transparent electrode/hole transport layer (HTL)/active layer/electron transport layer (ETL)/top electrode, as illustrated in Figure 4.24. In this configuration, the bottom electrode functions as the hole-collecting contact, while the top electrode collects electrons.

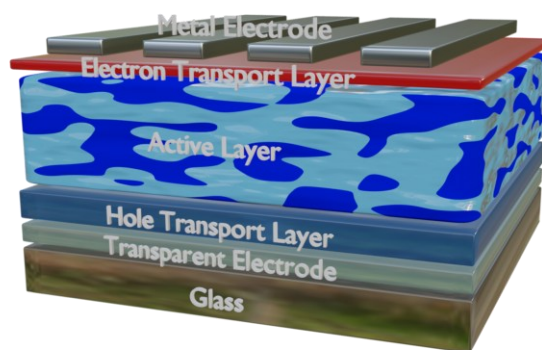


Figure 4.24: Schematic representation of the conventional device architecture of an organic solar cell.

The solar cells were fabricated on transparent Indium Tin Oxide (ITO)-coated glass substrates. ITO, a transparent conducting oxide (TCO), serves as the bottom electrode. The patterned ITO substrates were purchased from Kintec, Hong Kong, with a sheet resistance of $10 \Omega/\text{sq}$. The substrate dimensions were $2 \text{ cm} \times 2 \text{ cm}$. The patterned ITO substrates were cleaned by sequential sonication in acetone and isopropyl alcohol (IPA) for 20 minutes each and dried with nitrogen. To further improve the wettability of the substrates, the cleaned ITO-coated glass substrates were treated in a UV-ozone cleaner for 10 minutes.

4.3.1 Deposition of charge transport, active layer, and metal electrode.

Spin-coating was employed to deposit the HTL layer onto the ITO substrate uniformly. In this process, a solution is dispensed onto the substrate using a micropipette, and the substrate is spun at a specified speed for a predetermined duration. The process begins with spreading the solution and removing excess solvent during the ramp-up phase, continuing until the solvent evaporates in the final stage, as discussed in the spin-coating section. Spin-coating is a straightforward method that provides precise control over the film's morphology and thickness. In this thesis, PEDOT:PSS was used as the HTL and deposited onto the ITO substrate

via spin-coating. The water-based PEDOT:PSS dispersed solution was first filtered through a 0.45 μm nylon filter and then spin-coated at 5000 rpm for 45 seconds. The films were subsequently annealed at 120 $^{\circ}\text{C}$ for 20 minutes in ambient air. After annealing the PEDOT:PSS layer, the samples were transferred to a nitrogen-filled glove box ($\text{O}_2 < 5 \text{ ppm}$, $\text{H}_2\text{O} < 0.1 \text{ ppm}$) (MB200MOD, MBraun Inert Gas Systems GmbH, Germany) for processing of the active layer. The active layer solution was prepared by mixing the donor and acceptor materials in a 1:1 (V/V) ratio in a common solvent, are discussed in each paper separately. The donor-acceptor blend was stirred overnight at the desired temperature. Following this, the blend solution was spin-coated at 3000 rpm for 60 seconds onto the PEDOT:PSS layer and annealed at 100 $^{\circ}\text{C}$ for 10 minutes. After that, the PDINO, dissolved in methanol and used as an ETL solution, was spin-coated onto the active layer at 5000 rpm for 40 seconds. To complete the device architecture, the top metal Ag electrode was thermally deposited. The thickness of the Ag electrode was 100 nm, deposited initially at a rate of 0.1 $\text{\AA}/\text{s}$ for the first 10 nm, and then increased to 1 $\text{\AA}/\text{s}$ for the remaining deposition. The four pixels, each with an area of 4 mm^2 , were defined using a metal shadow mask. For the electrical measurements, the fabricated devices are kept inside a gas-tight holder with a quartz window, as shown in Figure 4.25.

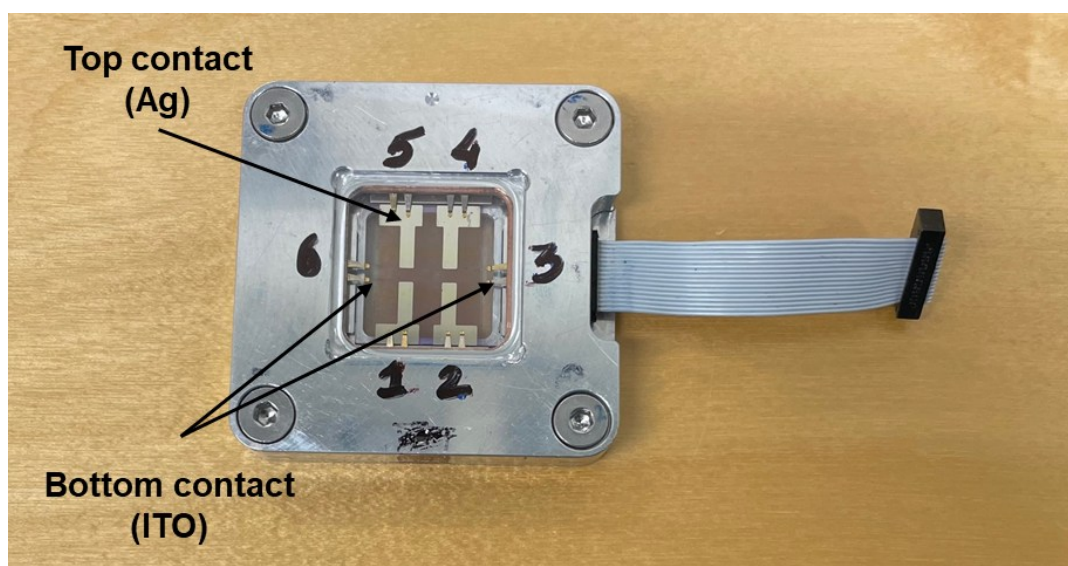


Figure 4.25: Schematic of the fabricated device inside a quartz-window device holder.

4.4 Device characterization

In this work, electrical characterization of the fabricated devices was performed by measuring both dark and illuminated current-voltage (I-V) characteristics and the external quantum efficiency (EQE).

4.4.1 I-V measurements

The current-voltage (I-V) measurement is the primary characterization technique used to evaluate device quality and power conversion efficiency (PCE). In this measurement, the current through the diode is recorded as the voltage across the device is systematically varied. The diode can be modelled by the Shockley diode equation:

$$I_D = I_0 \left[\exp\left(\frac{eV}{nk_B T}\right) - 1 \right] \quad (4.10)$$

where I_D is the dark current through the diode, I_0 the reverse bias saturation current of the diode, e the elementary charge, V the voltage across the diode, n the ideality factor, k_B Boltzmann's constant, and T the absolute temperature.

Figure 4.26 presents the equivalent circuit of the solar cell under illumination. In this circuit, I_L , R_{sh} , and R_s represent the photo-generated current, shunt resistance, and series resistance, respectively.

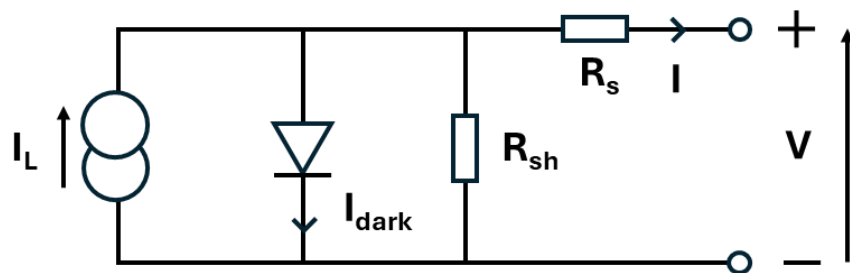


Figure 4.26: Equivalent circuit diagram of the solar cell under illumination, represented by a single-diode model including both series and shunt resistances.

The current flowing through the device under an applied bias voltage can be expressed as:

$$I = -I_L + I_0 \left[\exp\left(\frac{q(V - IR_s)}{\eta k_B T}\right) - 1 \right] + \frac{V - IR_s}{R_{sh}} \quad (4.11)$$

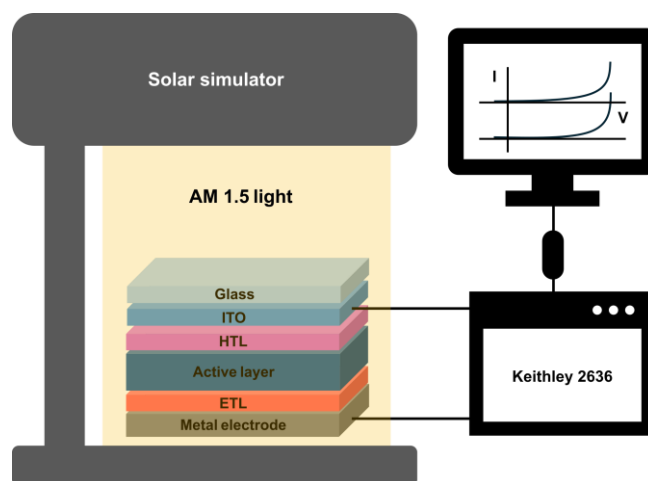


Figure 4.27: Schematic of the illuminated J - V measurement setup for organic solar cells under a solar simulator.

All photovoltaic measurements were carried out under ambient conditions. Current-voltage (I-V) characteristics were measured outside the glovebox using a gas-tight holder equipped with a quartz window, a Keithley 2636 source meter, and a xenon-lamp-based solar simulator (ORIEL Sol2A ABA), as shown in Figure 4.27. The simulator was calibrated to AM 1.5G at 100 mW cm^{-2} using a certified reference solar cell from Newport.

4.4.2 IPCE measurements

The incident photon-to-current efficiency (IPCE) is an essential characterization technique for solar cells and plays a crucial role in optical design and optimization of photovoltaic devices. From IPCE measurements, the spectral responsivity (SR), external quantum efficiency (EQE), and internal quantum efficiency (IQE) of the device can be determined. In this work, the IPCE spectra of all organic solar cells were measured using a Bentham PVE 300 system. A schematic illustration of the IPCE measurement setup is shown in Figure 4.28. In the Bentham PVE 300 system, two light sources are used: a 75 W xenon lamp and a 100 W quartz halogen (QTH) lamp, to generate a white-light beam with an intensity below 1 mW cm^{-1} . The light is passed through a monochromator, and both wavelength control and IPCE data acquisition are carried out using the BenWin+ software. Measurements can be performed in three modes: DC, AC, and transformer. In the AC and transformer

modes, the continuous (DC) light is mechanically chopped at a frequency of 295 Hz, and the resulting modulated signal is used as the reference for the lock-in amplifier. The chopped light is then guided through optical lenses and focused onto the device.

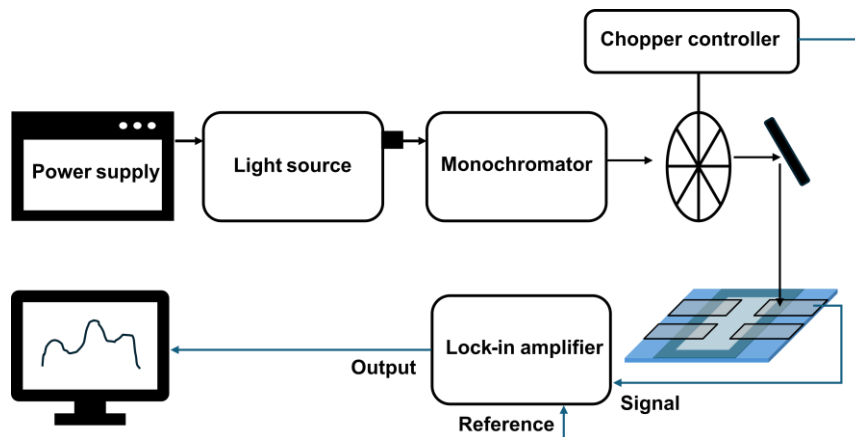


Figure 4.28: Schematic of external quantum efficiency setup.

To ensure reliable measurements, the illuminated spot is kept smaller than the device's active area by selecting slits that match the device geometry. Before each measurement series, the Bentham PVE 300 system is calibrated using a standard silicon reference photodiode over the wavelength range of 300-1100 nm.

4.4.3 Photo-CELIV measurements

Photo-CELIV (photo-induced charge extraction by linearly increasing voltage) is a powerful transient technique used to investigate free-carrier transport in solar cells. In this method, a short white-light pulse is first applied to generate free charge carriers within the device. Subsequently, a linearly increasing voltage ramp is applied to extract these photogenerated carriers. The offset voltage prior to the ramp is set to the open-circuit condition so that no current flows in the steady state. The extraction process results in a characteristic current overshoot superimposed on the displacement current. A schematic illustration of the measurement scheme is shown in Figure 4.29.

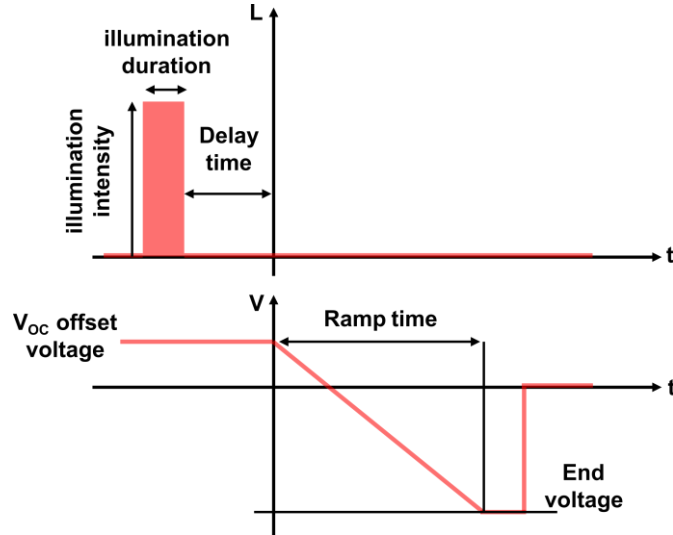


Figure 4.29: Schematic representation of the Photo-CELIV measurement, adapted from PAIOS (Fluxim).

From the position of the transient peak in time, the mobility of the faster charge carriers can be determined using an analytical expression.

$$\mu = \frac{2d^2}{3At_{max}^2 \left[1 + 0.36 \frac{\Delta j}{j_{disp}} \right]} \quad (4.12)$$

where, where d is the thickness of the active layer, A is the ramp rate (100 V/ms), t_{max} is the time where the current peaks, Δj is the peak current minus the displacement current, and j_{disp} is the displacement current. In this work, Photo-CELIV measurements were performed using the Platform for All-In-One Characterization of Solar Cells (PAIOS, Fluxim, Switzerland).

Chapter 5

Summary of papers

Paper I & II

In this paper, we investigated the photodegradation of the donor polymer PBDB-T, small molecule acceptor (SMA) Y5, small molecule polymer acceptors (SMPA) PF5-Y5, and PYT. Spectroscopy techniques such as UV-vis absorption, Fourier-Transform Infrared (FTIR), and X-ray and Ultraviolet Photoelectron Spectroscopy (XPS and UPS), are used to monitor the changes in the thin films upon photodegradation over time in the air.

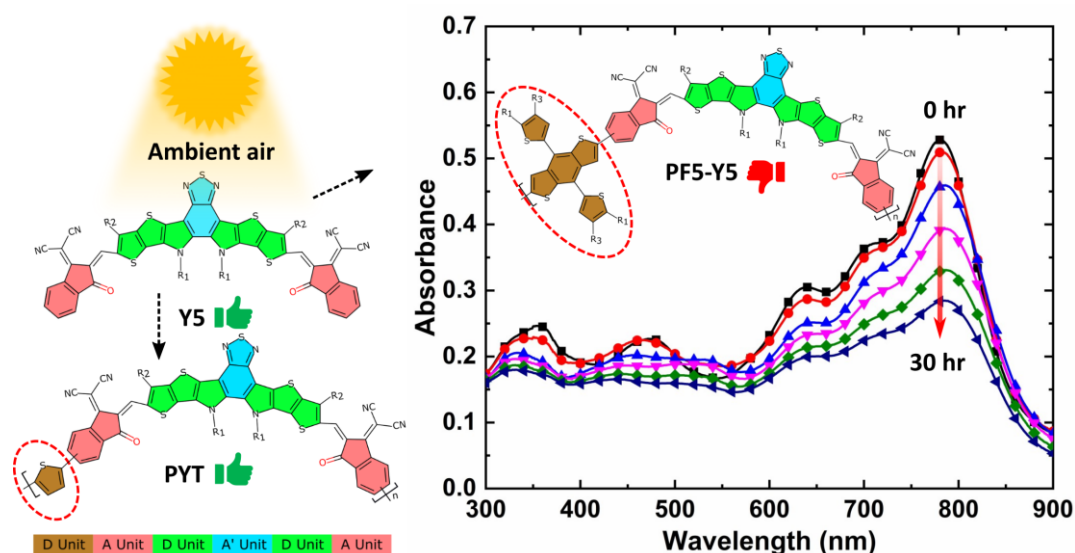


Figure 5.1: The graphical summary of papers I and II.

The thin films of PBDB-T, Y5, PF5-Y5, and PYT were exposed to AM1.5 in ambient conditions. Surprisingly, the absorption spectra shows that the Y5 and PYT films remain stable, with no major changes after 30 hours of exposure, whereas the PBDB-T and PF5-Y5 films photobleach rapidly. The FTIR spectra reveals the formation of new carbonyl and sulphone peaks in PBDB-T and PF5-Y5 after exposure, while these peaks are absent in Y5 and PYT. In addition, the C 1s XPS spectra confirms the formation of new carbonyl peaks, and S 2p spectra reveal the

formation of sulphone groups after 30 hours of exposure in PBDB-T and PF5-Y5 films. To understand the effect of photodegradation on energy levels, the work function is determined from the secondary-electron cutoff in UPS measurements for different exposure times. The SECO reveals that the Fermi level of PBDB-T and PF5-Y5 changed by 0.9 eV and 0.4 eV, respectively, upon photodegradation. Moreover, PBDB-T and PF5-Y5 also exhibit changes in the shape of their valence band spectra. However, for Y5, no major changes were observed. The results conclude that the presence of the benzo[1,2-b:4,5-b']dithiophene moiety with alkylated thiophenes as side chains (BDT-T) unit in PBDB-T and PF5-Y5 accelerates photodegradation, whereas the replacement of the BDT-T unit with the thiophene unit improves the intrinsic photostability of PYT.

Paper III

In this paper, we investigated the light-induced photodegradation of the donor polymer PM6 and the non-fullerene acceptor Y6 under ambient conditions. Our results show that the acceptor Y6 exhibits substantially higher intrinsic photostability than the donor PM6. However, when incorporated into a PM6:Y6 blend and subjected to AM 1.5 illumination, the degradation rate of Y6 was found to be significantly accelerated compared to that of neat Y6, indicating that intermolecular interactions within the blend can adversely impact the stability of the acceptor.

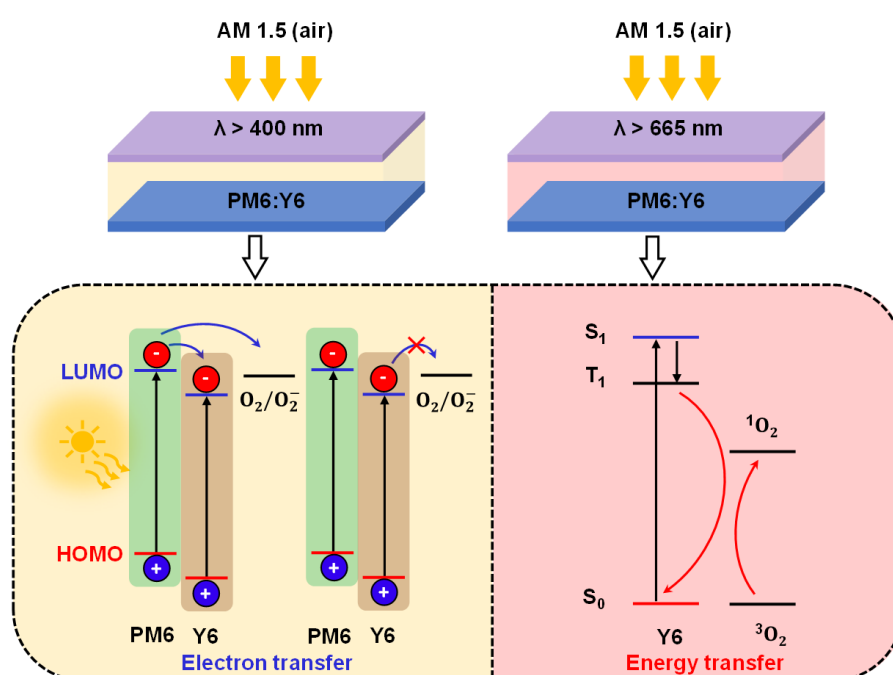


Figure 5.2: The graphical summary of paper III.

The photodegradation of the blends occurs through multiple pathways, including the formation of superoxide radicals and singlet oxygen. These processes arise from electron transfer from the donor to ground-state oxygen molecules, leading to superoxide radical formation, and energy transfer from either the donor or the acceptor components to ground-state oxygen molecules, generating singlet oxygen. Notably, when the blends were exposed to filtered light (665nm long-pass filter), no light was absorbed by the donor, and electron transfer from the donor was suppressed, effectively blocking the formation of superoxide radicals. Under these conditions, degradation primarily occurred due to energy transfer processes, which lead to the formation of singlet oxygen.

Paper IV

In this paper, we investigated the impact of processing solvents (chloroform and chlorobenzene) on the degradation of thin films and OSCs using the donor polymer PM6 and the non-fullerene acceptor Y6. The samples were degraded under an AM 1.5 solar simulator in air. The results show that PM6 degrades faster than Y6 in both solvents, with chlorobenzene causing faster Y6 degradation than chloroform. In the PM6:Y6 blend, PM6 degrades more rapidly when processed from chlorobenzene, while the degradation rate of Y6 remains the same in both solvents.

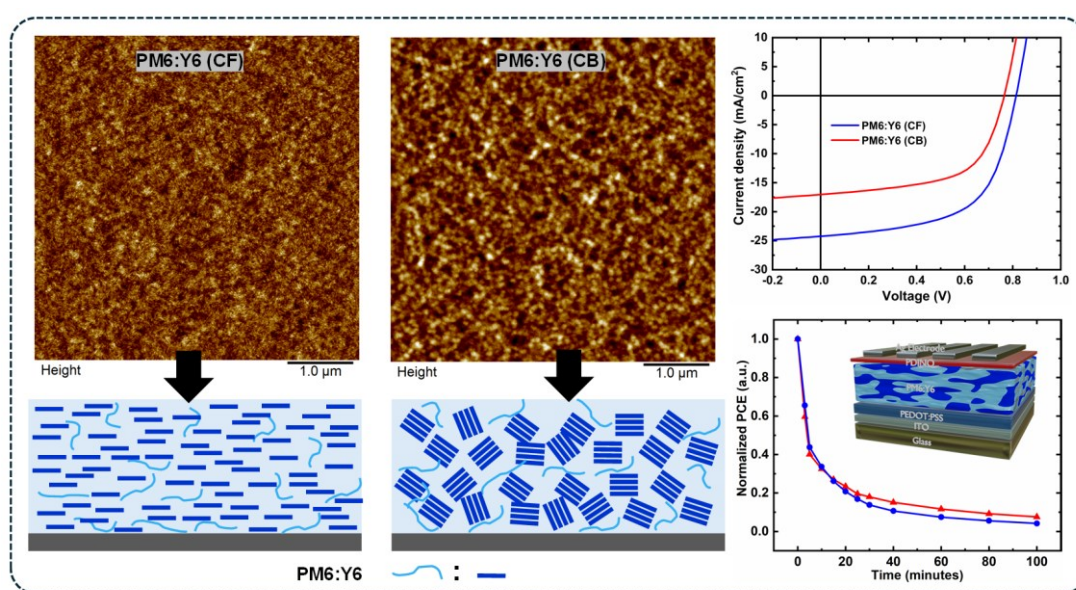


Figure 5.3: The graphical summary of paper IV.

Morphological differences, identified through atomic force microscopy (AFM) and near-edge X-ray absorption fine structure (NEXAFS) spectroscopy, reveal that films processed from chlorobenzene have higher surface roughness, and Y6 exhibits mixed orientation depending on the solvent. OSCs made from chloroform-processed films achieve a higher power conversion efficiency (11.7%) due to better exciton dissociation and charge separation. However, both solvent-processed devices degrade at similar rates, indicating that solvent choice does not significantly affect the degradation rate of OSCs.

Paper V

In this paper, we investigated the use of PC₇₀BM as a third component to enhance both the photovoltaic performance and photostability of organic solar cells (OSCs) based on the low-cost donor polymer PTQ10 and the non-fullerene acceptor Y6.

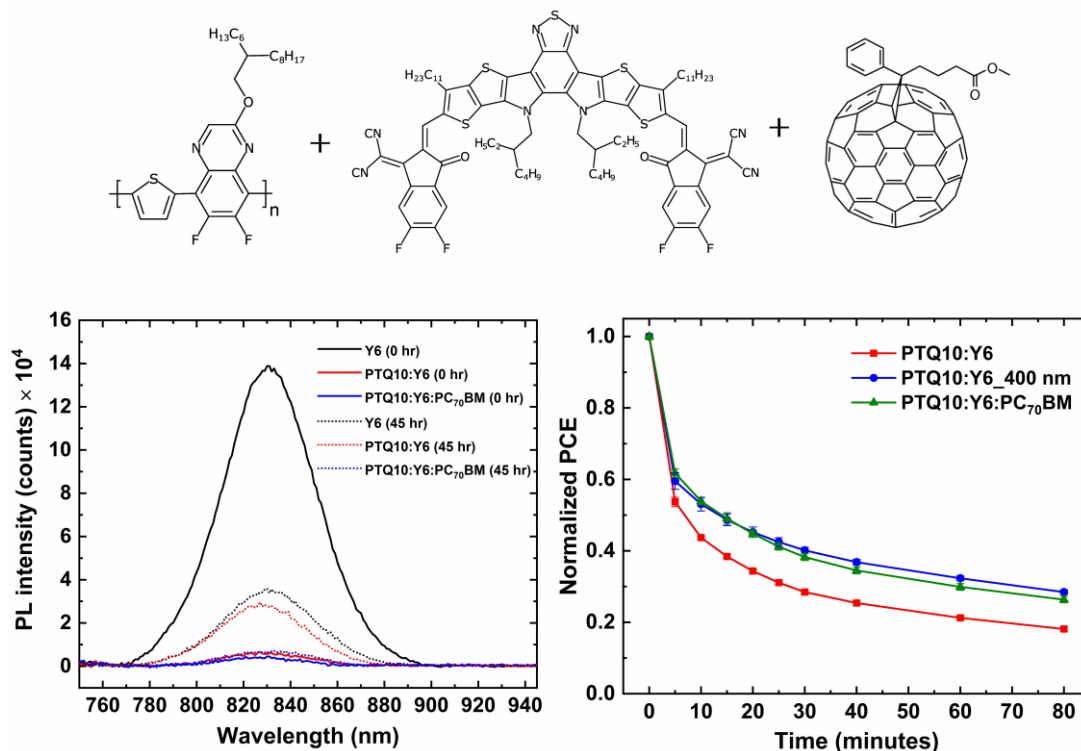


Figure 5.4: The graphical summary of paper V.

UV-vis spectroscopy reveals that after 45 hours of continuous AM 1.5 illumination in air, pristine PTQ10 and Y6 films remain stable, while the binary PTQ10:Y6 blend shows rapid photobleaching. When the blend was exposed to light filtered by a 400 nm long-pass filter, the degradation rate decreased, particularly for Y6, indicating its sensitivity to high-energy UV photons. Adding 20% PC₇₀BM to the blend reduces the formation of new carbonyl groups, suggesting less photo-oxidation. Steady-state photoluminescence spectra confirm better charge dissociation in the ternary blend. The ternary PTQ10:Y6:PC₇₀BM OSCs achieved a power conversion efficiency (PCE) of 11%, with improved short-circuit current, open-circuit voltage, and fill factor. After 100 minutes of continuous illumination in air, binary PTQ10:Y6 OSCs degraded by 82%, while degradation in the ternary devices was reduced to 74%, demonstrating that PC₇₀BM incorporation and spectral management can mitigate photodegradation in PTQ10:Y6-based OSCs.

Chapter 6

Conclusions

The work presented in this thesis investigates the photodegradation behavior of active-layer materials and organic solar cells (OSCs) under simulated AM 1.5 illumination in ambient conditions. The results provide insight into the degradation mechanisms of donor and non-fullerene acceptor (NFA) materials and demonstrate how molecular structure, light conditions, morphology, and additives influence the photostability of the active layer and OSCs.

In the first part of the thesis, the photodegradation of PBDB-T, Y5, and their copolymers PF5-Y5 and PYT were studied. UV-vis and IR spectroscopy revealed that Y5 and PYT exhibit excellent photostability, while PBDB-T and PF5-Y5 undergo photooxidation, indicated by the formation of carbonyl groups. XPS and UPS measurements further confirmed oxygen incorporation and significant changes in the electronic structure of PBDB-T and PF5-Y5. The results show that the benzodithiophene (BDT) unit present in PBDB-T and PF5-Y5 is particularly susceptible to photooxidation, whereas PYT, in which BDT is replaced by thiophene, exhibits improved stability. These findings demonstrate that the molecular design of both donor and acceptor polymers plays a crucial role in determining photochemical stability. Next, the photodegradation behavior of PM6, Y6, and PM6:Y6 was also investigated. While pristine Y6 films exhibit relatively high stability, the degradation of Y6 is accelerated in the PM6:Y6 blend. When PM6:Y6 blend films are exposed to unfiltered or 400 nm long-pass filtered light, degradation occurs through multiple pathways, including direct photodegradation, superoxide formation via electron transfer, and singlet oxygen formation through energy transfer to ambient oxygen. In contrast, when PM6:Y6 blend films are exposed to 665 nm long-pass filtered light, degradation is dominated by singlet oxygen formation via energy transfer from the acceptor to ambient oxygen, followed by photooxidation of both the donor and acceptor. This work could

inspire the design of new donor and acceptor materials by tuning their singlet and triplet states to prevent photodegradation caused by oxygen-mediated species.

In the second part of the thesis, the influence of morphology on photodegradation was studied in PM6:Y6 films processed from chloroform and chlorobenzene. Chloroform-processed films exhibit smoother morphology and predominantly face-on molecular orientation, leading to slower photobleaching and improved protection of Y6 against photooxidation. Solar cells prepared from chloroform solutions showed higher efficiencies due to improved charge transport and better exciton dissociation. The photodegradation of the solar cells was found to be faster than that of thin films. This suggests that, in the device, additional charge-transport layers such as the hole- and electron-transport layers, may also contribute to the degradation process. Overall, the results indicate that the choice of solvent does not significantly affect the rate of device degradation, as both solvent types result in similar degradation patterns. Finally, light-induced degradation was investigated in binary PTQ10:Y6 and ternary PTQ10:Y6:PC₇₀BM systems. Pristine PTQ10 and Y6 films show excellent stability, whereas the PTQ10:Y6 blend degrades more rapidly. Under 400 nm long-pass filter conditions, the degradation rate is significantly reduced. The incorporation of PC₇₀BM reduced photooxidation and improved photostability while slightly enhancing device performance. These results demonstrate that both UV exposure and the addition of a third component play an important role in determining device stability.

Overall, this thesis provides a comprehensive understanding of photodegradation mechanisms in OSC active-layer materials. The results highlight the importance of molecular design, morphology control, additives, and illumination conditions for improving the photochemical stability and operational lifetime of OSCs.

Chapter 7

Outlook

Future work in the field of OSCs should focus on addressing the inherent stability challenges of different photoactive materials, as these are critical for the long-term viability of technology. As highlighted in this thesis, while much of the previous research has prioritized maximizing efficiency, many high-performance materials still lack the intrinsic properties required to ensure the operational stability needed for commercial applications.

Building on the findings from Papers I and II, where the BDT-T moiety was identified as a potential stability issue, future research should avoid using BDT-T moiety and explore alternative molecular architectures or modifications that could enhance the long-term stability of OSC materials. In line with the insights from Paper III, photodegradation of PM6:Y6 blends occurs through the formation of superoxide radicals and singlet oxygen. Further investigation is needed to develop strategies to mitigate photodegradation by designing new donor and acceptor materials with improved photostability, for example, by tuning the positions of their singlet and triplet states to minimize the formation of oxygen-mediated reactive species. Paper IV suggests that OSCs fabricated from chloroform and chlorobenzene do not show significant differences in degradation rate. Further investigation is needed to identify the main factors governing device degradation, such as charge-transport layers and electrode materials. Moreover, in Paper V, where the addition of PC₇₀BM was shown to improve device performance and photostability, the results suggest that additives play a key role in enhancing the durability of OSCs. Future studies should explore the optimization of such additives and investigate other potential stabilizing agents or combinations of materials that could further improve the photostability and overall performance of OSC devices.

Overall, advancing the long-term stability of OSCs will require a comprehensive strategy combining improved molecular design, suppression of photochemical degradation pathways, and optimized device architectures. These efforts will be essential for the development of stable and commercially viable organic photovoltaic technologies.

References

- 1 J. Xue. Perspectives on Organic Photovoltaics. *Polymer Reviews* **50**, 411-419 (2010).
- 2 W. Deng, W. Liu, R. Qian & H. Wu. Toward High-Efficiency Organic Photovoltaics: Perspectives on the Origin and Role of Energetic Disorder. *The Journal of Physical Chemistry Letters* **13**, 544-551 (2022).
- 3 M. Farghali, A. I. Osman, Z. Chen, A. Abdelhaleem, I. Ihara, I. M. A. Mohamed, P.-S. Yap & D. W. Rooney. Social, environmental, and economic consequences of integrating renewable energies in the electricity sector: a review. *Environmental Chemistry Letters* **21**, 1381-1418 (2023).
- 4 H. Ritchie. *Our World in Data*, <https://ourworldindata.org/grapher/global-primary-energy>, (accessed May 23, 2025).
- 5 U. Nations. World population projected to reach 9.8 billion in 2050, and 11.2 billion in 2100. *Department of Economic and Social Affairs* (2017).
- 6 A. Z. Amin. *Global energy transformation: a roadmap to 2050*, https://www.irena.org/media/Files/IRENA/Agency/Publication/2018/Apr/IRENA_Report_GET_2018.pdf, (2019).
- 7 S. Karagöz. *Anadolu Agency*, <https://www.aa.com.tr/en/energy/oil/world-energy-demand-will-increase-50-by-2050-eia/33749>, (accessed April 27, 2025).
- 8 H. Ritchie & P. Rosado. Energy mix. *Our world in data* (2020).
- 9 *Agency, I. E., Fuels and Technology-Coal. France*, <https://www.iea.org/fuels-and-technologies/coal>, (2023).
- 10 EIA. *U.S. energy facts explained*, <https://www.eia.gov/energyexplained/us-energy-facts>, (2022).
- 11 *Without big changes, this is what the environment will look like in 2050*, <https://www.unep.org/news-and-stories/story/without-big-changes-what-environment-will-look-2050>, (2025).
- 12 K. Kitamori, T. Manders, R. Dellink & A. Tabeau. OECD environmental outlook to 2050: the consequences of inaction. Report No. 9264122168, (OECD, 2012).

- 13 S. Kirsch. Running out? Rethinking resource depletion. *The extractive industries and society* **7**, 838-840 (2020).
- 14 U. Nations. Renewable energy—powering a safer future. *United Nations. Consulté le: 8 avril 2025*, (2022).
- 15 H. Hertz. Ueber einen Einfluss des ultravioletten Lichtes auf die electrische Entladung. *Annalen der Physik* **267**, 983-1000 (1887).
- 16 A. E. Becquerel. Recherches sur les effets de la radiation chimique de la lumiere solaire au moyen des courants electriques. *Comptes Rendus de L'Academie des Sciences* **9** (1839).
- 17 A. B. Arons & M. Peppard. Einstein's Proposal of the Photon Concept—a Translation of the Annalen der Physik Paper of 1905. *American Journal of Physics* **33**, 367-374 (1965).
- 18 P. T. Landsberg. Nobel Lectures in Physics, 1901-1921. *Physics Bulletin* **18**, 151 (1967).
- 19 D. M. Chapin, C. S. Fuller & G. L. Pearson. A New Silicon p-n Junction Photocell for Converting Solar Radiation into Electrical Power. *Journal of Applied Physics* **25**, 676-677 (1954).
- 20 X. Wang, X. Tian, X. Chen, L. Ren & C. Geng. A review of end-of-life crystalline silicon solar photovoltaic panel recycling technology. *Solar Energy Materials and Solar Cells* **248**, 111976 (2022).
- 21 M. Tao, V. Fthenakis, B. Ebin, B.-M. Steenari, E. Butler, P. Sinha, R. Corkish, K. Wambach & E. S. Simon. Major challenges and opportunities in silicon solar module recycling. *Progress in Photovoltaics: Research and Applications* **28**, 1077-1088 (2020).
- 22 J. H. Petermann, D. Zielke, J. Schmidt, F. Haase, E. G. Rojas & R. Brendel. 19%-efficient and 43 μm -thick crystalline Si solar cell from layer transfer using porous silicon. *Progress in Photovoltaics: Research and Applications* **20**, 1-5 (2012).
- 23 V. E. Ferry, M. A. Verschuuren, H. B. T. Li, R. E. I. Schropp, H. A. Atwater & A. Polman. Improved red-response in thin film a-Si:H solar cells with soft-imprinted plasmonic back reflectors. *Applied Physics Letters* **95** (2009).

- 24 D. E. Carlson & C. R. Wronski. Amorphous silicon solar cell. *Applied Physics Letters* **28**, 671-673 (1976).
- 25 J. Sites & J. Pan. Strategies to increase CdTe solar-cell voltage. *Thin Solid Films* **515**, 6099-6102 (2007).
- 26 T. A. Gessert. in *Comprehensive Renewable Energy* (ed Ali Sayigh) 423-438 (Elsevier, 2012).
- 27 F. Kessler & D. Rudmann. Technological aspects of flexible CIGS solar cells and modules. *Solar Energy* **77**, 685-695 (2004).
- 28 L. L. Kazmerski, F. R. White, M. S. Ayyagari, Y. J. Juang & R. P. Patterson. Growth and characterization of thin-film compound semiconductor photovoltaic heterojunctions. *Journal of Vacuum Science and Technology* **14**, 65-68 (1977).
- 29 B. E. Hardin, H. J. Snaith & M. D. McGehee. The renaissance of dye-sensitized solar cells. *Nature Photonics* **6**, 162-169 (2012).
- 30 B. O'Regan & M. Grätzel. A low-cost, high-efficiency solar cell based on dye-sensitized colloidal TiO₂ films. *Nature* **353**, 737-740 (1991).
- 31 J. Han, K. Park, S. Tan, Y. Vaynzof, J. Xue, E. W.-G. Diau, M. G. Bawendi, J.-W. Lee & I. Jeon. Perovskite solar cells. *Nature Reviews Methods Primers* **5**, 3 (2025).
- 32 A. Kojima, K. Teshima, Y. Shirai & T. Miyasaka. Organometal Halide Perovskites as Visible-Light Sensitizers for Photovoltaic Cells. *Journal of the American Chemical Society* **131**, 6050-6051 (2009).
- 33 N. A. Tegegne, L. T. Nchinda & T. P. J. Krüger. Progress Toward Stable Organic Solar Cells. *Advanced Optical Materials* **13**, 2402257 (2025).
- 34 Y. Zhai, Y. Chang, A. Tang & K. Lu. A review of photostability in organic solar cells: from mechanisms to improvement strategies. *Journal of Materials Chemistry A* **13**, 9589-9618 (2025).
- 35 C. W. Tang. Two-layer organic photovoltaic cell. *Applied Physics Letters* **48**, 183-185 (1986).
- 36 T. D. Lee & A. U. Ebong. A review of thin film solar cell technologies and challenges. *Renewable and Sustainable Energy Reviews* **70**, 1286-1297 (2017).

- 37 J. Y. Kim, J.-W. Lee, H. S. Jung, H. Shin & N.-G. Park. High-Efficiency Perovskite Solar Cells. *Chemical Reviews* **120**, 7867-7918 (2020).
- 38 F. Yang, Y. Huang, Y. Li & Y. Li. Large-area flexible organic solar cells. *npj Flexible Electronics* **5**, 30 (2021).
- 39 National Renewable Energy Laboratory, <https://www.nrel.gov/pv/cell-efficiency.html>, (accessed Feb 25, 2026).
- 40 E. Efficiency. What is the energy payback for PV? *National Renewable Energy Laboratory* (2004).
- 41 B. L. Smith, A. Sekar, H. Mirletz, G. Heath & R. Margolis. An Updated Life Cycle Assessment of Utility-Scale Solar Photovoltaic Systems Installed in the United States. (National Renewable Energy Laboratory (NREL), Golden, CO (United States), 2024).
- 42 V. Muteri, M. Cellura, D. Curto, V. Franzitta, S. Longo, M. Mistretta & M. L. Parisi. Review on Life Cycle Assessment of Solar Photovoltaic Panels. *Energies* **13**, 252 (2020).
- 43 O. Vigil-Galán, M. Courel, J. A. Andrade-Arvizu, Y. Sánchez, M. Espíndola-Rodríguez, E. Saucedo, D. Seuret-Jiménez & M. Titsworth. Route towards low cost-high efficiency second generation solar cells: current status and perspectives. *Journal of Materials Science: Materials in Electronics* **26**, 5562-5573 (2015).
- 44 M. V. Dambhare, B. Butey & S. V. Moharil. Solar photovoltaic technology: A review of different types of solar cells and its future trends. *Journal of Physics: Conference Series* **1913**, 012053 (2021).
- 45 S. Ananthakumar, J. R. Kumar & S. M. Babu. in *Emerging Nanostructured Materials for Energy and Environmental Science* (eds Saravanan Rajendran, Mu Naushad, Kumar Raju, & Rabah Boukherroub) 305-339 (Springer International Publishing, 2019).
- 46 G. Conibeer. Third-generation photovoltaics. *Materials Today* **10**, 42-50 (2007).
- 47 Z. Liang, Y. Zhang, H. Xu, W. Chen, B. Liu, J. Zhang, H. Zhang, Z. Wang, D.-H. Kang, J. Zeng, X. Gao, Q. Wang, H. Hu, H. Zhou, X. Cai, X. Tian, P. Reiss, B. Xu, T. Kirchartz, Z. Xiao, S. Dai, N.-G. Park, J. Ye & X. Pan.

- Homogenizing out-of-plane cation composition in perovskite solar cells. *Nature* **624**, 557-563 (2023).
- 48 C. Yang, W. Hu, J. Liu, C. Han, Q. Gao, A. Mei, Y. Zhou, F. Guo & H. Han. Achievements, challenges, and future prospects for industrialization of perovskite solar cells. *Light: Science & Applications* **13**, 227 (2024).
- 49 Y. Sun, T. Liu, Y. Kan, K. Gao, B. Tang & Y. Li. Flexible Organic Solar Cells: Progress and Challenges. *Small Science* **1**, 2100001 (2021).
- 50 L. Zhu, M. Zhang, J. Xu, C. Li, J. Yan, G. Zhou, W. Zhong, T. Hao, J. Song, X. Xue, Z. Zhou, R. Zeng, H. Zhu, C.-C. Chen, R. C. I. MacKenzie, Y. Zou, J. Nelson, Y. Zhang, Y. Sun & F. Liu. Single-junction organic solar cells with over 19% efficiency enabled by a refined double-fibril network morphology. *Nature Materials* **21**, 656-663 (2022).
- 51 Z. Zheng, J. Wang, P. Bi, J. Ren, Y. Wang, Y. Yang, X. Liu, S. Zhang & J. Hou. Tandem Organic Solar Cell with 20.2% Efficiency. *Joule* **6**, 171-184 (2022).
- 52 *Infinity PV*, <https://www.infinitypv.com/product-overview>, (accessed June 20, 2025).
- 53 *Epishine company*, <https://www.epishine.com/news/epishine-unveils-the-worlds-most-resource-efficient-solar-cell-factory>, (accessed May 18, 2025).
- 54 *Heliatek company*, <https://www.heliatek.com/en/media/news/detail/austrias-largest-opv-installation-at-power-plant-simmering-in-vienna>, (accessed May 20, 2025).
- 55 P. Ding, D. Yang, S. Yang & Z. Ge. Stability of organic solar cells: toward commercial applications. *Chemical Society Reviews* **53**, 2350-2387 (2024).
- 56 J. C. Carrillo-Sendejas & J.-L. Maldonado. Progress in organic solar cells: Materials, challenges, and novel strategies for niche applications. *APL Energy* **3** (2025).
- 57 X. Du, T. Heumueller, W. Gruber, A. Classen, T. Unruh, N. Li & C. J. Brabec. Efficient Polymer Solar Cells Based on Non-fullerene Acceptors with Potential Device Lifetime Approaching 10 Years. *Joule* **3**, 215-226 (2019).

- 58 Y. Li, B. Huang, X. Zhang, J. Ding, Y. Zhang, L. Xiao, B. Wang, Q. Cheng, G. Huang, H. Zhang, Y. Yang, X. Qi, Q. Zheng, Y. Zhang, X. Qiu, M. Liang & H. Zhou. Lifetime over 10000 hours for organic solar cells with Ir/IrOx electron-transporting layer. *Nature Communications* **14**, 1241 (2023).
- 59 Y. Li, X. Huang, K. Ding, H. K. M. Sheriff, L. Ye, H. Liu, C.-Z. Li, H. Ade & S. R. Forrest. Non-fullerene acceptor organic photovoltaics with intrinsic operational lifetimes over 30 years. *Nature Communications* **12**, 5419 (2021).
- 60 W. Oh, S. Bae, S. Kim, N. Park, S.-I. Chan, H. Choi, H. Hwang & D. Kim. Analysis of degradation in 25-year-old field-aged crystalline silicon solar cells. *Microelectronics Reliability* **100-101**, 113392 (2019).
- 61 A. Ndiaye, A. Charki, A. Kobi, C. M. F. Kébé, P. A. Ndiaye & V. Sambou. Degradations of silicon photovoltaic modules: A literature review. *Solar Energy* **96**, 140-151 (2013).
- 62 Z. Zheng, H. Yao, L. Ye, Y. Xu, S. Zhang & J. Hou. PBDB-T and its derivatives: A family of polymer donors enables over 17% efficiency in organic photovoltaics. *Materials Today* **35**, 115-130 (2020).
- 63 S. Shoae, H. M. Luong, J. Song, Y. Zou, T.-Q. Nguyen & D. Neher. What We have Learnt from PM6:Y6. *Advanced Materials* **36**, 2302005 (2024).
- 64 Q. Liu, Y. Jiang, K. Jin, J. Qin, J. Xu, W. Li, J. Xiong, J. Liu, Z. Xiao, K. Sun, S. Yang, X. Zhang & L. Ding. 18% Efficiency organic solar cells. *Science Bulletin* **65**, 272-275 (2020).
- 65 C. Sun, F. Pan, S. Chen, R. Wang, R. Sun, Z. Shang, B. Qiu, J. Min, M. Lv, L. Meng, C. Zhang, M. Xiao, C. Yang & Y. Li. Achieving Fast Charge Separation and Low Nonradiative Recombination Loss by Rational Fluorination for High-Efficiency Polymer Solar Cells. *Advanced Materials* **31**, 1905480 (2019).
- 66 A. J. Clarke, J. Luke, R. Meitzner, J. Wu, Y. Wang, H. K. H. Lee, E. M. Speller, H. Bristow, H. Cha, M. J. Newman, K. Hooper, A. Evans, F. Gao, H. Hoppe, I. McCulloch, U. S. Schubert, T. M. Watson, J. R. Durrant, W. C. Tsoi, J.-S. Kim & Z. Li. Non-fullerene acceptor photostability and its impact on organic solar cell lifetime. *Cell Reports Physical Science* **2**, 100498 (2021).

- 67 S. Park & H. J. Son. Intrinsic photo-degradation and mechanism of polymer solar cells: the crucial role of non-fullerene acceptors. *Journal of Materials Chemistry A* **7**, 25830-25837 (2019).
- 68 Y. Li, T. Li & Y. Lin. Stability: next focus in organic solar cells based on non-fullerene acceptors. *Materials Chemistry Frontiers* **5**, 2907-2930 (2021).
- 69 W. Li, D. Liu & T. Wang. Stability Of Non-Fullerene Electron Acceptors and Their Photovoltaic Devices. *Advanced Functional Materials* **31**, 2104552 (2021).
- 70 Y. Qin, N. Balar, Z. Peng, A. Gadisa, I. Angunawela, A. Bagui, S. Kashani, J. Hou & H. Ade. The performance-stability conundrum of BTP-based organic solar cells. *Joule* **5**, 2129-2147 (2021).
- 71 W. R. Mateker & M. D. McGehee. Progress in Understanding Degradation Mechanisms and Improving Stability in Organic Photovoltaics. *Advanced Materials* **29**, 1603940 (2017).
- 72 S. A. Gevorgyan, I. M. Heckler, E. Bundgaard, M. Corazza, M. Hösel, R. R. Søndergaard, G. A. dos Reis Benatto, M. Jørgensen & F. C. Krebs. Improving, characterizing and predicting the lifetime of organic photovoltaics. *Journal of Physics D: Applied Physics* **50**, 103001 (2017).
- 73 J. Han, H. Xu, S. H. K. Paleti, A. Sharma & D. Baran. Understanding photochemical degradation mechanisms in photoactive layer materials for organic solar cells. *Chemical Society Reviews* **53**, 7426-7454 (2024).
- 74 H. Xu, J. Han, A. Sharma, S. H. K. Paleti, S. Hultmark, A. Yazmaciyan, C. Müller & D. Baran. Progress in the Stability of Small Molecule Acceptor-Based Organic Solar Cells. *Advanced Materials* **37**, 2407119 (2025).
- 75 M. P. de Jong, L. J. van IJzendoorn & M. J. A. de Voigt. Stability of the interface between indium-tin-oxide and poly(3,4-ethylenedioxythiophene)/poly(styrenesulfonate) in polymer light-emitting diodes. *Applied Physics Letters* **77**, 2255-2257 (2000).
- 76 K. Norrman, M. V. Madsen, S. A. Gevorgyan & F. C. Krebs. Degradation Patterns in Water and Oxygen of an Inverted Polymer Solar Cell. *Journal of the American Chemical Society* **132**, 16883-16892 (2010).

- 77 B. Ecker, J. C. Nolasco, J. Pallarés, L. F. Marsal, J. Posdorfer, J. Parisi & E. von Hauff. Degradation Effects Related to the Hole Transport Layer in Organic Solar Cells. *Advanced Functional Materials* **21**, 2705-2711 (2011).
- 78 S. Chen, J. R. Manders, S.-W. Tsang & F. So. Metal oxides for interface engineering in polymer solar cells. *Journal of Materials Chemistry* **22**, 24202-24212 (2012).
- 79 S. D. Chavhan, R. Hansson, L. K. E. Ericsson, P. Beyer, A. Hofmann, W. Brütting, A. Opitz & E. Moons. Low temperature processed NiOx hole transport layers for efficient polymer solar cells. *Organic Electronics* **44**, 59-66 (2017).
- 80 A. Uddin, M. B. Upama, H. Yi & L. Duan. Encapsulation of Organic and Perovskite Solar Cells: A Review. *Coatings* **9**, 65 (2019).
- 81 Q. Lu, Z. Yang, X. Meng, Y. Yue, M. A. Ahmad, W. Zhang, S. Zhang, Y. Zhang, Z. Liu & W. Chen. A Review on Encapsulation Technology from Organic Light Emitting Diodes to Organic and Perovskite Solar Cells. *Advanced Functional Materials* **31**, 2100151 (2021).
- 82 Z.-X. Liu, Z.-P. Yu, Z. Shen, C. He, T.-K. Lau, Z. Chen, H. Zhu, X. Lu, Z. Xie, H. Chen & C.-Z. Li. Molecular insights of exceptionally photostable electron acceptors for organic photovoltaics. *Nature Communications* **12**, 3049 (2021).
- 83 Q. Zhang, Y. Chen, X. Liu & M. Fahlman. In situ near-ambient pressure X-ray photoelectron spectroscopy reveals the effects of water, oxygen and light on the stability of PM6:Y6 photoactive layers. *Journal of Materials Chemistry C* **11**, 3112-3118 (2023).
- 84 J. Guo, Y. Wu, R. Sun, W. Wang, J. Guo, Q. Wu, X. Tang, C. Sun, Z. Luo, K. Chang, Z. Zhang, J. Yuan, T. Li, W. Tang, E. Zhou, Z. Xiao, L. Ding, Y. Zou, X. Zhan, C. Yang, Z. Li, C. J. Brabec, Y. Li & J. Min. Suppressing photo-oxidation of non-fullerene acceptors and their blends in organic solar cells by exploring material design and employing friendly stabilizers. *Journal of Materials Chemistry A* **7**, 25088-25101 (2019).
- 85 Y. Wang, J. Luke, A. Privitera, N. Rolland, C. Labanti, G. Londi, V. Lemaur, D. T. W. Toolan, A. J. Sneyd, S. Jeong, D. Qian, Y. Olivier, L. Sorace, J.-S.

- Kim, D. Beljonne, Z. Li & A. J. Gillett. The critical role of the donor polymer in the stability of high-performance non-fullerene acceptor organic solar cells. *Nature* **7**, 810-829 (2023).
- 86 J. Luke, E. M. Speller, A. Wadsworth, M. F. Wyatt, S. Dimitrov, H. K. H. Lee, Z. Li, W. C. Tsoi, I. McCulloch, D. Bagnis, J. R. Durrant & J.-S. Kim. Twist and Degrade—Impact of Molecular Structure on the Photostability of Nonfullerene Acceptors and Their Photovoltaic Blends. *Advanced Energy Materials* **9**, 1803755 (2019).
- 87 C. Wang, S. Ni, S. Braun, M. Fahlman & X. Liu. Effects of water vapor and oxygen on non-fullerene small molecule acceptors. *Journal of Materials Chemistry C* **7**, 879-886 (2019).
- 88 L. Ciammaruchi, O. Zapata-Arteaga, E. Gutiérrez-Fernández, J. Martin & M. Campoy-Quiles. Structure dependent photostability of ITIC and ITIC-4F. *Materials Advances* **1**, 2846-2861 (2020).
- 89 Y. A. Quiroz Avalos, Q. Eynaud, P. Perkhun, A. Rivaton, W. Köntges, R. R. Schröder, T. Koganezawa, N. Yoshimoto, A. K. Bharwal, D. Duché, C. M. Ruiz, O. Margeat, C. Aumaitre, R. Demadrille, C. Videlot-Ackermann & J. Ackermann. Insights into the relationship between molecular and order-dependent photostability of ITIC derivatives for the production of photochemically stable blends. *Journal of Materials Chemistry C* **12**, 4130-4141 (2024).
- 90 B. Liu, Y. Han, Z. Li, H. Gu, L. Yan, Y. Lin, Q. Luo, S. Yang & C.-Q. Ma. Visible Light-Induced Degradation of Inverted Polymer:Nonfullerene Acceptor Solar Cells: Initiated by the Light Absorption of ZnO Layer. *Solar RRL* **5**, 2000638 (2021).
- 91 T. Liu, Q. C. Burlingame, M. R. Ivancevic, X. Liu, J. Hu, B. P. Rand & Y.-L. Loo. Photochemical Decomposition of Y-Series Non-Fullerene Acceptors Is Responsible for Degradation of High-Efficiency Organic Solar Cells. *Advanced Energy Materials* **13**, 2300046 (2023).
- 92 P. Weitz, V. M. Le Corre, X. Du, K. Forberich, C. Deibel, C. J. Brabec & T. Heumüller. Revealing Photodegradation Pathways of Organic Solar Cells by

- Spectrally Resolved Accelerated Lifetime Analysis. *Advanced Energy Materials* **13**, 2202564 (2023).
- 93 S. Prasad, Z. Genene, C. F. N. Marchiori, S. Singh, L. K. E. Ericsson, E. Wang, C. M. Araujo & E. Moons. Effect of molecular structure on the photochemical stability of acceptor and donor polymers used in organic solar cells. *Materials Advances* **5**, 7708-7720 (2024).
- 94 J.-W. Lee, H.-G. Lee, E. S. Oh, S.-W. Lee, T. N.-L. Phan, S. Li, T.-S. Kim & B. J. Kim. Rigid- and soft-block-copolymerized conjugated polymers enable high-performance intrinsically stretchable organic solar cells. *Joule* **8**, 204-223 (2024).
- 95 A. Köhler & H. Bässler. *Electronic processes in organic semiconductors: An introduction*. (John Wiley & Sons, 2015).
- 96 R. C. Evans, P. Douglas & H. D. Burrow. *Applied photochemistry*. Vol. 36 (Springer, 2013).
- 97 M. C. Scharber & N. S. Sariciftci. Low Band Gap Conjugated Semiconducting Polymers. *Advanced Materials Technologies* **6**, 2000857 (2021).
- 98 B. P. Kirk, J. M. Bjuggren, G. G. Andersson, P. Dastoor & M. R. Andersson. Printing and Coating Techniques for Scalable Organic Photovoltaic Fabrication. *Materials* **17**, 2511 (2024).
- 99 F. Zhao, C. Wang & X. Zhan. Morphology Control in Organic Solar Cells. *Advanced Energy Materials* **8**, 1703147 (2018).
- 100 S. Yoon, E.-Y. Shin, N.-K. Cho, S. Park, H. Y. Woo & H. J. Son. Progress in morphology control from fullerene to nonfullerene acceptors for scalable high-performance organic photovoltaics. *Journal of Materials Chemistry A* **9**, 24729-24758 (2021).
- 101 A. Mishra, N. N. Bhuyan, H. Xu & G. D. Sharma. Advances in layer-by-layer processing for efficient and reliable organic solar cells. *Materials Advances* **4**, 6031-6063 (2023).
- 102 R. Yu, X. Wei, G. Wu & Z. a. Tan. Layer-by-layered organic solar cells: Morphology optimizing strategies and processing techniques. *Aggregate* **3**, e107 (2022).

- 103 H. Xu, J. Han, M. Babics, L. Huerta Hernandez, D. Rosas Villalva, M. Sanviti, J. Bertrandie, Y. Zhang, Y. Liu, H. Chen, L. Zhao, J. Troughton, J. Martin, F. Laquai, S. De Wolf & D. Baran. Elucidating the photodegradation pathways of polymer donors for organic solar cells with seven months of outdoor operational stability. *Nature Photonics* **19**, 415-425 (2025).
- 104 A. Rivaton, A. Tournebize, J. Gaume, P.-O. Bussière, J.-L. Gardette & S. Therias. Photostability of organic materials used in polymer solar cells. *Polymer International* **63**, 1335-1345 (2014).
- 105 M. Jørgensen, K. Norrman & F. C. Krebs. Stability/degradation of polymer solar cells. *Solar Energy Materials and Solar Cells* **92**, 686-714 (2008).
- 106 H. K. H. Lee, A. M. Telford, J. A. Röhr, M. F. Wyatt, B. Rice, J. Wu, A. de Castro Maciel, S. M. Tuladhar, E. Speller, J. McGettrick, J. R. Searle, S. Pont, T. Watson, T. Kirchartz, J. R. Durrant, W. C. Tsoi, J. Nelson & Z. Li. The role of fullerenes in the environmental stability of polymer:fullerene solar cells. *Energy & Environmental Science* **11**, 417-428 (2018).
- 107 E. T. Hoke, I. T. Sachs-Quintana, M. T. Lloyd, I. Kauvar, W. R. Mateker, A. M. Nardes, C. H. Peters, N. Kopidakis & M. D. McGehee. The Role of Electron Affinity in Determining Whether Fullerenes Catalyze or Inhibit Photooxidation of Polymers for Solar Cells. *Advanced Energy Materials* **2**, 1351-1357 (2012).
- 108 I. V. Martynov, L. N. Inasaridze & P. A. Troshin. Resist or Oxidize: Identifying Molecular Structure–Photostability Relationships for Conjugated Polymers Used in Organic Solar Cells. *ChemSusChem* **15**, e202101336 (2022).
- 109 D. Zhou, J. Wang, Z. Xu, H. Xu, J. Quan, J. Deng, Y. Li, Y. Tong, B. Hu & L. Chen. Recent advances of nonfullerene acceptors in organic solar cells. *Nano Energy* **103**, 107802 (2022).
- 110 G. Zhang, F. R. Lin, F. Qi, T. Heumüller, A. Distler, H.-J. Egelhaaf, N. Li, P. C. Y. Chow, C. J. Brabec, A. K. Y. Jen & H.-L. Yip. Renewed Prospects for Organic Photovoltaics. *Chemical Reviews* **122**, 14180-14274 (2022).
- 111 Z. Wang, Z. Peng, Z. Xiao, D. Seyitliyev, K. Gundogdu, L. Ding & H. Ade. Thermodynamic Properties and Molecular Packing Explain Performance

- and Processing Procedures of Three D18:NFA Organic Solar Cells. *Advanced Materials* **32**, 2005386 (2020).
- 112 C. An & J. Hou. Benzo[1,2-b:4,5-b']dithiophene-Based Conjugated Polymers for Highly Efficient Organic Photovoltaics. *Accounts of Materials Research* **3**, 540-551 (2022).
- 113 M. A. Anderson, A. Hamstra, B. W. Larson & E. L. Ratcliff. Distinguishing photo-induced oxygen attack on alkyl chain versus conjugated backbone for alkylthienyl-benzodithiophene (BDTT)-based push-pull polymers. *Journal of Materials Chemistry A* **11**, 17858-17871 (2023).
- 114 R. Ganesamoorthy, G. Sathiyam & P. Sakthivel. Review: Fullerene based acceptors for efficient bulk heterojunction organic solar cell applications. *Solar Energy Materials and Solar Cells* **161**, 102-148 (2017).
- 115 T. D. Anthopoulos, G. C. Anyfantis, G. C. Papavassiliou & D. M. de Leeuw. Air-stable ambipolar organic transistors. *Applied Physics Letters* **90** (2007).
- 116 V. Blazinic, L. K. E. Ericsson, S. A. Muntean & E. Moons. Photodegradation in air of spin-coated PC60BM and PC70BM films. *Synthetic Metals* **241**, 26-30 (2018).
- 117 A. S. Anselmo, A. Dzwilewski, K. Svensson & E. Moons. Photodegradation of the electronic structure of PCBM and C60 films in air. *Chemical Physics Letters* **652**, 220-224 (2016).
- 118 I. E. Brumboiu, L. K. E. Ericsson, V. Blazinic, R. Hansson, A. Opitz, B. Brena & E. Moons. Photooxidation of PC60BM: new insights from spectroscopy. *Physical Chemistry Chemical Physics* **24**, 25753-25766 (2022).
- 119 T. Heumueller, W. R. Mateker, A. Distler, U. F. Fritze, R. Cheacharoen, W. H. Nguyen, M. Biele, M. Salvador, M. von Delius, H.-J. Egelhaaf, M. D. McGehee & C. J. Brabec. Morphological and electrical control of fullerene dimerization determines organic photovoltaic stability. *Energy & Environmental Science* **9**, 247-256 (2016).
- 120 F. Piersimoni, G. Degutis, S. Bertho, K. Vandewal, D. Spoltore, T. Vangerven, J. Drijkoningen, M. K. Van Bael, A. Hardy, J. D'Haen, W. Maes, D. Vanderzande, M. Nesladek & J. Manca. Influence of fullerene photodimerization on the PCBM crystallization in polymer: Fullerene bulk

- heterojunctions under thermal stress. *Journal of Polymer Science Part B: Polymer Physics* **51**, 1209-1214 (2013).
- 121 J. Zhang, H. S. Tan, X. Guo, A. Facchetti & H. Yan. Material insights and challenges for non-fullerene organic solar cells based on small molecular acceptors. *Nature Energy* **3**, 720-731 (2018).
- 122 S. Li, W. Liu, C.-Z. Li, M. Shi & H. Chen. Efficient Organic Solar Cells with Non-Fullerene Acceptors. *Small* **13**, 1701120 (2017).
- 123 Y. Lin, J. Wang, Z.-G. Zhang, H. Bai, Y. Li, D. Zhu & X. Zhan. An Electron Acceptor Challenging Fullerenes for Efficient Polymer Solar Cells. *Advanced Materials* **27**, 1170-1174 (2015).
- 124 G. Zhang, J. Zhao, P. C. Y. Chow, K. Jiang, J. Zhang, Z. Zhu, J. Zhang, F. Huang & H. Yan. Nonfullerene Acceptor Molecules for Bulk Heterojunction Organic Solar Cells. *Chemical Reviews* **118**, 3447-3507 (2018).
- 125 H. Gao, C. Han, X. Wan & Y. Chen. Recent progress in non-fused ring electron acceptors for high performance organic solar cells. *Industrial Chemistry & Materials* **1**, 60-78 (2023).
- 126 E. M. Speller, A. J. Clarke, N. Aristidou, M. F. Wyatt, L. Francàs, G. Fish, H. Cha, H. K. H. Lee, J. Luke, A. Wadsworth, A. D. Evans, I. McCulloch, J.-S. Kim, S. A. Haque, J. R. Durrant, S. D. Dimitrov, W. C. Tsoi & Z. Li. Toward Improved Environmental Stability of Polymer:Fullerene and Polymer:Nonfullerene Organic Solar Cells: A Common Energetic Origin of Light- and Oxygen-Induced Degradation. *ACS Energy Letters* **4**, 846-852 (2019).
- 127 S. Prasad, C. M. G. Araujo & E. Moons. Role of the donor on the light-induced degradation of Y6 non-fullerene acceptors in PM6:Y6 blend films. *Journal of Materials Chemistry C* (2026).
- 128 L. Ye, M. Gao & J. Hou. Advances and prospective in thermally stable nonfullerene polymer solar cells. *Science China Chemistry* **64**, 1875-1887 (2021).
- 129 K. Zhou, J. Xin & W. Ma. Hierarchical Morphology Stability under Multiple Stresses in Organic Solar Cells. *ACS Energy Letters* **4**, 447-455 (2019).
- 130 M. O. Reese, S. A. Gevorgyan, M. Jørgensen, E. Bundgaard, S. R. Kurtz, D. S. Ginley, D. C. Olson, M. T. Lloyd, P. Morvillo, E. A. Katz, A. Elschner,

- O. Haillant, T. R. Currier, V. Shrotriya, M. Hermenau, M. Riede, K. R. Kirov, G. Trimmel, T. Rath, O. Inganäs, F. Zhang, M. Andersson, K. Tvingstedt, M. Lira-Cantu, D. Laird, C. McGuinness, S. Gowrisanker, M. Pannone, M. Xiao, J. Hauch, R. Steim, D. M. DeLongchamp, R. Rösch, H. Hoppe, N. Espinosa, A. Urbina, G. Yaman-Uzunoglu, J.-B. Bonekamp, A. J. J. M. van Breemen, C. Girotto, E. Voroshazi & F. C. Krebs. Consensus stability testing protocols for organic photovoltaic materials and devices. *Solar Energy Materials and Solar Cells* **95**, 1253-1267 (2011).
- 131 I. T. Sachs-Quintana, T. Heumüller, W. R. Mateker, D. E. Orozco, R. Cheacharoen, S. Sweetnam, C. J. Brabec & M. D. McGehee. Electron Barrier Formation at the Organic-Back Contact Interface is the First Step in Thermal Degradation of Polymer Solar Cells. *Advanced Functional Materials* **24**, 3978-3985 (2014).
- 132 M. Campoy-Quiles, T. Ferenczi, T. Agostinelli, P. G. Etchegoin, Y. Kim, T. D. Anthopoulos, P. N. Stavrinou, D. D. C. Bradley & J. Nelson. Morphology evolution via self-organization and lateral and vertical diffusion in polymer:fullerene solar cell blends. *Nature Materials* **7**, 158-164 (2008).
- 133 F. C. Jamieson, E. B. Domingo, T. McCarthy-Ward, M. Heeney, N. Stingelin & J. R. Durrant. Fullerene crystallisation as a key driver of charge separation in polymer/fullerene bulk heterojunction solar cells. *Chemical Science* **3**, 485-492 (2012).
- 134 S. Li, L. Zhan, F. Liu, J. Ren, M. Shi, C.-Z. Li, T. P. Russell & H. Chen. An Unfused-Core-Based Nonfullerene Acceptor Enables High-Efficiency Organic Solar Cells with Excellent Morphological Stability at High Temperatures. *Advanced Materials* **30**, 1705208 (2018).
- 135 K. An, W. Zhong, F. Peng, W. Deng, Y. Shang, H. Quan, H. Qiu, C. Wang, F. Liu, H. Wu, N. Li, F. Huang & L. Ying. Mastering morphology of non-fullerene acceptors towards long-term stable organic solar cells. *Nature Communications* **14**, 2688 (2023).
- 136 H. Xu, F. Yuan, D. Zhou, X. Liao, L. Chen & Y. Chen. Hole transport layers for organic solar cells: recent progress and prospects. *Journal of Materials Chemistry A* **8**, 11478-11492 (2020).

- 137 A. Al-Ahmad, B. Vaughan, J. Holdsworth, W. Belcher, X. Zhou & P. Dastoor. The Role of the Electron Transport Layer in the Degradation of Organic Photovoltaic Cells. *Coatings* **12**, 1071 (2022).
- 138 B. G. Krishna, D. S. Ghosh & S. Tiwari. Hole and electron transport materials: A review on recent progress in organic charge transport materials for efficient, stable, and scalable perovskite solar cells. *Chemistry of Inorganic Materials* **1**, 100026 (2023).
- 139 J. Geist, A. R. Schaefer, J.-F. Song, Y. H. Wang & E. F. Zalewski. An accurate value for the absorption coefficient of silicon at 633 nm. *Journal of research of the National Institute of Standards and Technology* **95**, 549 (1990).
- 140 Q. Fan, Q. An, Y. Lin, Y. Xia, Q. Li, M. Zhang, W. Su, W. Peng, C. Zhang, F. Liu, L. Hou, W. Zhu, D. Yu, M. Xiao, E. Moons, F. Zhang, T. D. Anthopoulos, O. Inganäs & E. Wang. Over 14% efficiency all-polymer solar cells enabled by a low bandgap polymer acceptor with low energy loss and efficient charge separation. *Energy & Environmental Science* **13**, 5017-5027 (2020).
- 141 M. Knupfer. Exciton binding energies in organic semiconductors. *Applied Physics A* **77**, 623-626 (2003).
- 142 R. Holmes, S. Kéna-Cohen, V. Menon & S. Forrest. Strong coupling and hybridization of Frenkel and Wannier-Mott excitons in an organic-inorganic optical microcavity. *Physical Review B* **74**, 235211 (2006).
- 143 Y. Firdaus, V. M. Le Corre, S. Karuthedath, W. Liu, A. Markina, W. Huang, S. Chattopadhyay, M. M. Nahid, M. I. Nugraha, Y. Lin, A. Seitkhan, A. Basu, W. Zhang, I. McCulloch, H. Ade, J. Labram, F. Laquai, D. Andrienko, L. J. A. Koster & T. D. Anthopoulos. Long-range exciton diffusion in molecular non-fullerene acceptors. *Nature Communications* **11**, 5220 (2020).
- 144 J. Guo, B. Moss & T. M. Clarke. Quantifying triplet formation in conjugated polymer/non-fullerene acceptor blends. *Journal of Materials Chemistry A* **10**, 20874-20885 (2022).
- 145 A. Classen, C. L. Chochos, L. Lüer, V. G. Gregoriou, J. Wortmann, A. Osvet, K. Forberich, I. McCulloch, T. Heumüller & C. J. Brabec. The role

- of exciton lifetime for charge generation in organic solar cells at negligible energy-level offsets. *Nature Energy* **5**, 711-719 (2020).
- 146 P. Peumans, A. Yakimov & S. R. Forrest. Small molecular weight organic thin-film photodetectors and solar cells. *Journal of Applied Physics* **93**, 3693-3723 (2003).
- 147 G. Long, B. Wu, A. Solanki, X. Yang, B. Kan, X. Liu, D. Wu, Z. Xu, W.-R. Wu, U.-S. Jeng, J. Lin, M. Li, Y. Wang, X. Wan, T. C. Sum & Y. Chen. New Insights into the Correlation between Morphology, Excited State Dynamics, and Device Performance of Small Molecule Organic Solar Cells. *Advanced Energy Materials* **6**, 1600961 (2016).
- 148 B. Jung, K. Kim, J. Kim, S. Kim, E. Kim & W. Kim. Inter-diffused ordered bulk heterojunction organic photovoltaics: optimized morphology for efficient exciton dissociation and charge transport. *Solar Energy Materials and Solar Cells* **120**, 675-684 (2014).
- 149 T. M. Clarke & J. R. Durrant. Charge Photogeneration in Organic Solar Cells. *Chemical Reviews* **110**, 6736-6767 (2010).
- 150 G. Dennler, M. C. Scharber & C. J. Brabec. Polymer-Fullerene Bulk-Heterojunction Solar Cells. *Advanced Materials* **21**, 1323-1338 (2009).
- 151 D. Veldman, S. C. J. Meskers & R. A. J. Janssen. The Energy of Charge-Transfer States in Electron Donor–Acceptor Blends: Insight into the Energy Losses in Organic Solar Cells. *Advanced Functional Materials* **19**, 1939-1948 (2009).
- 152 C. Yang, J. Zhang, N. Liang, H. Yao, Z. Wei, C. He, X. Yuan & J. Hou. Effects of energy-level offset between a donor and acceptor on the photovoltaic performance of non-fullerene organic solar cells. *Journal of Materials Chemistry A* **7**, 18889-18897 (2019).
- 153 Y. Tamai, R. Shirouchi, T. Saito, K. Kohzuki & S.-i. Natsuda. Role of the energy offset in the charge photogeneration and voltage loss of nonfullerene acceptor-based organic solar cells. *Journal of Materials Chemistry A* **11**, 17581-17593 (2023).
- 154 X. e. Li, Q. Zhang, J. Yu, Y. Xu, R. Zhang, C. Wang, H. Zhang, S. Fabiano, X. Liu, J. Hou, F. Gao & M. Fahlman. Mapping the energy level alignment

- at donor/acceptor interfaces in non-fullerene organic solar cells. *Nature Communications* **13**, 2046 (2022).
- 155 J. Bertrandie, J. Han, C. S. P. De Castro, E. Yengel, J. Gorenflot, T. Anthopoulos, F. Laquai, A. Sharma & D. Baran. The Energy Level Conundrum of Organic Semiconductors in Solar Cells. *Advanced Materials* **34**, 2202575 (2022).
- 156 C. M. Proctor, M. Kuik & T.-Q. Nguyen. Charge carrier recombination in organic solar cells. *Progress in Polymer Science* **38**, 1941-1960 (2013).
- 157 Y. Zhong, M. Causa', G. J. Moore, P. Krauspe, B. Xiao, F. Günther, J. Kublitski, R. Shivhare, J. Benduhn, E. BarOr, S. Mukherjee, K. M. Yallum, J. Réhault, S. C. B. Mannsfeld, D. Neher, L. J. Richter, D. M. DeLongchamp, F. Ortmann, K. Vandewal, E. Zhou & N. Banerji. Sub-picosecond charge-transfer at near-zero driving force in polymer:non-fullerene acceptor blends and bilayers. *Nature Communications* **11**, 833 (2020).
- 158 K. Vandewal, S. Albrecht, E. T. Hoke, K. R. Graham, J. Widmer, J. D. Douglas, M. Schubert, W. R. Mateker, J. T. Bloking, G. F. Burkhard, A. Sellinger, J. M. J. Fréchet, A. Amassian, M. K. Riede, M. D. McGehee, D. Neher & A. Salleo. Efficient charge generation by relaxed charge-transfer states at organic interfaces. *Nature Materials* **13**, 63-68 (2014).
- 159 P. Hu, X. He & H. Jiang. Greater than $10 \text{ cm}^2 \text{ V}^{-1} \text{ s}^{-1}$: A breakthrough of organic semiconductors for field-effect transistors. *InfoMat* **3**, 613-630 (2021).
- 160 B. Tan, H. Pan, H. Li, M. L. Minus, B. M. Budhlall & M. J. Sobkowicz. Improving Charge Carrier Mobility of Polymer Blend Field Effect Transistors with Majority Insulating Polymer Phase. *The Journal of Physical Chemistry C* **122**, 2918-2930 (2018).
- 161 N. A. Mica, S. A. J. Thomson & I. D. W. Samuel. Electron mobility of non-fullerene acceptors using a time of flight method. *Organic Electronics* **63**, 415-420 (2018).
- 162 S. R. Cowan, N. Banerji, W. L. Leong & A. J. Heeger. Charge Formation, Recombination, and Sweep-Out Dynamics in Organic Solar Cells. *Advanced Functional Materials* **22**, 1116-1128 (2012).

- 163 W. Shockley & W. T. Read. Statistics of the Recombinations of Holes and Electrons. *Physical Review* **87**, 835-842 (1952).
- 164 R. N. Hall. Electron-Hole Recombination in Germanium. *Physical Review* **87**, 387-387 (1952).
- 165 L. Hong & Z. Ge. Single-component organic solar cells with over 11% efficiency. *Chem* **7**, 1987-1989 (2021).
- 166 Y. Li, R. A. Pacalaj, Y. Luo, K. Ai, Y. Hai, S. Liang, K. Fan, A. A. Sergeev, R. Ma, T. A. Dela Peña, J. S. Müller, Z. Jin, P. S. Tuladhar, T. Jia, J. Wang, G. Li, K. S. Wong, W. Li, J. R. Durrant & J. Wu. Molecular Control of the Donor/Acceptor Interface Suppresses Charge Recombination Enabling High-Efficiency Single-Component Organic Solar Cells. *Advanced Materials* **37**, 2409212 (2025).
- 167 S. Liu, R. Duan, Z. Lin, Z. Xiao, M. Liu, Y. Li & Y. Zhao. Single-Component Organic Solar Cells with over 14% Efficiency. *ACS Applied Materials & Interfaces* **16**, 47988-47995 (2024).
- 168 Y. Wang & X. Zhan. Layer-by-Layer Processed Organic Solar Cells. *Advanced Energy Materials* **6**, 1600414 (2016).
- 169 S. Liu, Y. Zhou, Z. Liang, B. Zhao, W. Wang, Z. Xue, K. Ding, Z. Cong, H. Wu, G. Lu & C. Gao. High-Performance Pseudo-Bilayer Organic Solar Cells Enabled by Sequential Deposition of D18/Y6 Chloroform Solution. *ACS Applied Energy Materials* **6**, 5047-5057 (2023).
- 170 Y. Sun, L. Wang, C. Guo, J. Xiao, C. Liu, C. Chen, W. Xia, Z. Gan, J. Cheng, J. Zhou, Z. Chen, J. Zhou, D. Liu, T. Wang & W. Li. π -Extended Nonfullerene Acceptor for Compressed Molecular Packing in Organic Solar Cells To Achieve over 20% Efficiency. *Journal of the American Chemical Society* (2024).
- 171 G. Wu, X. Xu, C. Liao, L. Yu, R. Li & Q. Peng. Improving Cooperative Interactions Between Halogenated Aromatic Additives and Aromatic Side Chain Acceptors for Realizing 19.22% Efficiency Polymer Solar Cells. *Small* **19**, 2302127 (2023).
- 172 M. Deng, X. Xu, Y. Duan, L. Yu, R. Li & Q. Peng. Y-Type Non-Fullerene Acceptors with Outer Branched Side Chains and Inner Cyclohexane Side

- Chains for 19.36% Efficiency Polymer Solar Cells. *Advanced Materials* **35**, 2210760 (2023).
- 173 Q. Chen, J. Wu, M. Gumbo, L. R. Franco, K. Sun, L. Zeng, X. Liu, Y. Wang, D. Yu, L. Öhrström, M. S. Ozório, A. Holmes, C. M. Araujo, E. Olsson, M. Fahlman, R. Yang & E. Wang. Organic Solar Cells with 20.12% Efficiency Enabled by Monosubstituted Carbazole-Based Self-Assembled Monolayers. *ACS Energy Letters* **10**, 5584-5595 (2025).
- 174 S. M. Menke, N. A. Ran, G. C. Bazan & R. H. Friend. Understanding Energy Loss in Organic Solar Cells: Toward a New Efficiency Regime. *Joule* **2**, 25-35 (2018).
- 175 J. Hofinger, C. Putz, F. Mayr, K. Gugujonovic, D. Wielend & M. C. Scharber. Understanding the low voltage losses in high-performance non-fullerene acceptor-based organic solar cells. *Materials Advances* **2**, 4291-4302 (2021).
- 176 B. Qi & J. Wang. Fill factor in organic solar cells. *Physical Chemistry Chemical Physics* **15**, 8972-8982 (2013).
- 177 N. Tokmoldin, J. Vollbrecht, S. M. Hosseini, B. Sun, L. Perdigón-Toro, H. Y. Woo, Y. Zou, D. Neher & S. Shoaee. Explaining the Fill-Factor and Photocurrent Losses of Nonfullerene Acceptor-Based Solar Cells by Probing the Long-Range Charge Carrier Diffusion and Drift Lengths. *Advanced Energy Materials* **11**, 2100804 (2021).
- 178 S. A. Gevorgyan, N. Espinosa, L. Ciammaruchi, B. Roth, F. Livi, S. Tsopanidis, S. Züfle, S. Queirós, A. Gregori, G. A. d. R. Benatto, M. Corazza, M. V. Madsen, M. Hösel, M. J. Beliatis, T. T. Larsen-Olsen, F. Pastorelli, A. Castro, A. Mingorance, V. Lenzi, D. Fluhr, R. Roesch, M. Maria Duarte Ramos, A. Savva, H. Hoppe, L. S. A. Marques, I. Burgués, E. Georgiou, L. Serrano-Luján & F. C. Krebs. Baselines for Lifetime of Organic Solar Cells. *Advanced Energy Materials* **6**, 1600910 (2016).
- 179 Y. Zhang, I. D. W. Samuel, T. Wang & D. G. Lidzey. Current Status of Outdoor Lifetime Testing of Organic Photovoltaics. *Advanced Science* **5**, 1800434 (2018).

- 180 L. Duan, Y. Zhang, M. He, R. Deng, H. Yi, Q. Wei, Y. Zou & A. Uddin. Burn-In Degradation Mechanism Identified for Small Molecular Acceptor-Based High-Efficiency Nonfullerene Organic Solar Cells. *ACS Applied Materials & Interfaces* **12**, 27433-27442 (2020).
- 181 Q. Burlingame, X. Huang, X. Liu, C. Jeong, C. Coburn & S. R. Forrest. Intrinsically stable organic solar cells under high-intensity illumination. *Nature* **573**, 394-397 (2019).
- 182 H. Xu, J. Han, S. Chen, Y. Liu, L. Huerta Hernandez, J. Bertrandie, M. Babics, S. Alam, D. R. Villalva, S. H. K. Paleti, J. Gorenflot, C. Herok, N. Ramos, J. Troughton, A. Sharma, T. B. Marder, B. Engels, J. Martin, S. De Wolf, F. Laquai & D. Baran. Dissecting the structure-stability relationship of Y-series electron acceptors for real-world solar cell applications. *Joule* **7**, 2135-2151 (2023).
- 183 P. Škraba, G. Bratina, S. Igarashi, H. Nohira & K. Hirose. In diffusion and electronic energy structure in polymer layers on In tin oxide. *Thin Solid Films* **519**, 4216-4219 (2011).
- 184 K. W. Wong, H. L. Yip, Y. Luo, K. Y. Wong, W. M. Lau, K. H. Low, H. F. Chow, Z. Q. Gao, W. L. Yeung & C. C. Chang. Blocking reactions between indium-tin oxide and poly (3,4-ethylene dioxythiophene):poly(styrene sulphonate) with a self-assembly monolayer. *Applied Physics Letters* **80**, 2788-2790 (2002).
- 185 W. Tress & O. Inganäs. Simple experimental test to distinguish extraction and injection barriers at the electrodes of (organic) solar cells with S-shaped current–voltage characteristics. *Solar Energy Materials and Solar Cells* **117**, 599-603 (2013).
- 186 S. Trost, K. Zilberberg, A. Behrendt, A. Polywka, P. Görrn, P. Reckers, J. Maibach, T. Mayer & T. Riedl. Overcoming the “Light-Soaking” Issue in Inverted Organic Solar Cells by the Use of Al:ZnO Electron Extraction Layers. *Advanced Energy Materials* **3**, 1437-1444 (2013).
- 187 H. Dahiya, R. Suthar, K. Khandelwal, S. Karak & G. D. Sharma. Recent Advances in Organic and Inorganic Hole and Electron Transport Layers for

- Organic Solar Cells: Basic Concept and Device Performance. *ACS Applied Electronic Materials* **4**, 5119-5143 (2022).
- 188 D. Qian, L. Ye, M. Zhang, Y. Liang, L. Li, Y. Huang, X. Guo, S. Zhang, Z. a. Tan & J. Hou. Design, Application, and Morphology Study of a New Photovoltaic Polymer with Strong Aggregation in Solution State. *Macromolecules* **45**, 9611-9617 (2012).
- 189 Q. Fan, Y. Wang, M. Zhang, B. Wu, X. Guo, Y. Jiang, W. Li, B. Guo, C. Ye, W. Su, J. Fang, X. Ou, F. Liu, Z. Wei, T. C. Sum, T. P. Russell & Y. Li. High-Performance As-Cast Nonfullerene Polymer Solar Cells with Thicker Active Layer and Large Area Exceeding 11% Power Conversion Efficiency. *Advanced Materials* **30**, 1704546 (2018).
- 190 M. Fernández-Castro, J. Truer, M. Espindola-Rodriguez & J. W. Andreasen. Environmentally Friendly and Roll-Processed Flexible Organic Solar Cells Based on PM6:Y6. *Frontiers in Nanotechnology* **4** (2022).
- 191 C. Sun, F. Pan, H. Bin, J. Zhang, L. Xue, B. Qiu, Z. Wei, Z.-G. Zhang & Y. Li. A low cost and high performance polymer donor material for polymer solar cells. *Nature Communications* **9**, 743 (2018).
- 192 J. Yuan, Y. Zhang, L. Zhou, C. Zhang, T.-K. Lau, G. Zhang, X. Lu, H.-L. Yip, S. K. So, S. Beaupré, M. Mainville, P. A. Johnson, M. Leclerc, H. Chen, H. Peng, Y. Li & Y. Zou. Fused Benzothiadiazole: A Building Block for n-Type Organic Acceptor to Achieve High-Performance Organic Solar Cells. *Advanced Materials* **31**, 1807577 (2019).
- 193 G. Li, X. Zhang, L. O. Jones, J. M. Alzola, S. Mukherjee, L.-w. Feng, W. Zhu, C. L. Stern, W. Huang, J. Yu, V. K. Sangwan, D. M. DeLongchamp, K. L. Kohlstedt, M. R. Wasielewski, M. C. Hersam, G. C. Schatz, A. Facchetti & T. J. Marks. Systematic Merging of Nonfullerene Acceptor π -Extension and Tetrafluorination Strategies Affords Polymer Solar Cells with >16% Efficiency. *Journal of the American Chemical Society* **143**, 6123-6139 (2021).
- 194 J. Yuan, Y. Zhang, L. Zhou, G. Zhang, H.-L. Yip, T.-K. Lau, X. Lu, C. Zhu, H. Peng, P. A. Johnson, M. Leclerc, Y. Cao, J. Ulanski, Y. Li & Y. Zou.

- Single-Junction Organic Solar Cell with over 15% Efficiency Using Fused-Ring Acceptor with Electron-Deficient Core. *Joule* **3**, 1140-1151 (2019).
- 195 N. Yao, Q. Fan, Z. Genene, H. Liu, Y. Xia, G. Wen, Y. Yuan, E. Moons, J. van Stam, W. Zhang, X. Lu, E. Wang & F. Zhang. In Situ Study the Dynamics of Blade-Coated All-Polymer Bulk Heterojunction Formation and Impact on Photovoltaic Performance of Solar Cells. *Solar RRL* **7**, 2201134 (2023).
- 196 W. Wang, Q. Wu, R. Sun, J. Guo, Y. Wu, M. Shi, W. Yang, H. Li & J. Min. Controlling Molecular Mass of Low-Band-Gap Polymer Acceptors for High-Performance All-Polymer Solar Cells. *Joule* **4**, 1070-1086 (2020).
- 197 W. Kern. Handbook of semiconductor wafer cleaning technology. *New Jersey: Noyes Publication* **111** (1993).
- 198 D. F. Swinehart. The Beer-Lambert Law. *Journal of Chemical Education* **39**, 333 (1962).
- 199 S. F. Sun. *Physical chemistry of macromolecules: basic principles and issues*. (John Wiley & Sons, 2004).
- 200 L. M. Harwood & T. D. Claridge. Introduction to organic spectroscopy. (1997).
- 201 J. B. Lambert. Introduction to organic spectroscopy. (1987).
- 202 S. Chambon, A. Rivaton, J.-L. Gardette & M. Firon. Photo- and thermal degradation of MDMO-PPV:PCBM blends. *Solar Energy Materials and Solar Cells* **91**, 394-398 (2007).
- 203 U. Dettinger, H.-J. Egelhaaf, C. J. Brabec, F. Latteyer, H. Peisert & T. Chassé. FTIR Study of the Impact of PC[60]BM on the Photodegradation of the Low Band Gap Polymer PCPDTBT under O₂ Environment. *Chemistry of Materials* **27**, 2299-2308 (2015).
- 204 R. García & R. Pérez. Dynamic atomic force microscopy methods. *Surface Science Reports* **47**, 197-301 (2002).
- 205 G. Sternbach & J. Varon. Wilhelm Konrad Roentgen: A new kind of rays. *The Journal of Emergency Medicine* **11**, 743-745 (1993).
- 206 R. Clarke. in *Encyclopedia of Modern Optics* (ed Robert D. Guenther) 217-224 (Elsevier, 2005).

- 207 P. Willmott. *An introduction to synchrotron radiation: techniques and applications*. (John Wiley & Sons, 2019).
- 208 K. Siegbahn. Electron spectroscopy for atoms, molecules, and condensed matter. *Reviews of Modern Physics* **54**, 709 (1982).
- 209 S. Oswald. In *Encyclopedia of Analytical Chemistry*, Wiley, 2013.
- 210 J. Rivnay, S. C. B. Mannsfeld, C. E. Miller, A. Salleo & M. F. Toney. Quantitative Determination of Organic Semiconductor Microstructure from the Molecular to Device Scale. *Chemical Reviews* **112**, 5488-5519 (2012).
- 211 H. Ade & H. Stoll. Near-edge X-ray absorption fine-structure microscopy of organic and magnetic materials. *Nature Materials* **8**, 281-290 (2009).
- 212 M. M. Nahid, E. Gann, L. Thomsen & C. R. McNeill. NEXAFS spectroscopy of conjugated polymers. *European Polymer Journal* **81**, 532-554 (2016).
- 213 E. Gann, C. R. McNeill, M. Szumilo, H. Sirringhaus, M. Sommer, S. Maniam, S. J. Langford & L. Thomsen. Near-edge X-ray absorption fine-structure spectroscopy of naphthalene diimide-thiophene co-polymers. *The Journal of Chemical Physics* **140** (2014).
- 214 Y. Fu, T. H. Lee, Y.-C. Chin, R. A. Pacalaj, C. Labanti, S. Y. Park, Y. Dong, H. W. Cho, J. Y. Kim, D. Minami, J. R. Durrant & J.-S. Kim. Molecular orientation-dependent energetic shifts in solution-processed non-fullerene acceptors and their impact on organic photovoltaic performance. *Nature Communications* **14**, 1870 (2023).
- 215 L. P. Christopholi, Z. Genene, C. F. N. Marchiori, S. A. Muntean, E. Wang & E. Moons. Probing molecular orientation of donors and acceptors in all-polymer blend films by near-edge x-ray absorption fine structure spectroscopy. *Journal of Physics: Materials* **9**, 025001 (2026).
- 216 R. Hansson, L. K. E. Ericsson, N. P. Holmes, J. Rysz, A. Opitz, M. Campoy-Quiles, E. Wang, M. G. Barr, A. L. D. Kilcoyne, X. Zhou, P. Dastoor & E. Moons. Vertical and lateral morphology effects on solar cell performance for a thiophene–quinoxaline copolymer:PC70BM blend. *Journal of Materials Chemistry A* **3**, 6970-6979 (2015).

- 217 X. Guo, D. Li, Y. Zhang, M. Jan, J. Xu, Z. Wang, B. Li, S. Xiong, Y. Li, F. Liu, J. Tang, C. Duan, M. Fahlman & Q. Bao. Understanding the effect of N2200 on performance of J71: ITIC bulk heterojunction in ternary non-fullerene solar cells. *Organic Electronics* **71**, 65-71 (2019).
- 218 C. M. Björström, A. Bernasik, J. Rysz, A. Budkowski, S. Nilsson, M. Svensson, M. R. Andersson, K. O. Magnusson & E. Moons. Multilayer formation in spin-coated thin films of low-bandgap polyfluorene:PCBM blends. *Journal of Physics: Condensed Matter* **17**, L529 (2005).
- 219 S. Y. Heriot & R. A. Jones. An interfacial instability in a transient wetting layer leads to lateral phase separation in thin spin-cast polymer-blend films. *Nature materials* **4**, 782-786 (2005).
- 220 S. Nilsson, A. Bernasik, A. Budkowski & E. Moons. Morphology and Phase Segregation of Spin-Casted Films of Polyfluorene/PCBM Blends. *Macromolecules* **40**, 8291-8301 (2007).



Photodegradation Processes in Active Layer Materials for Organic Solar Cells

Organic solar cells (OSCs) have attracted significant attention due to their lightweight, flexibility, and potential for low-cost solution-based production process. Advances in molecular design and novel charge-transport materials have pushed power conversion efficiencies towards 20%. However, long-term stability, mainly due to materials degradation, remains a challenge for the commercial production of OSCs, making it crucial to understand the photodegradation of the active layer to enhance their long-term performance.

In the first part of this thesis, we investigate how the properties of state-of-the-art active-layer materials are affected by exposure to simulated sunlight in ambient conditions. Spectroscopy and microscopy techniques were employed to unveil changes in molecular structure and composition, as well as film morphology, and identify degradation pathways. In the second part of the thesis, we explore the effect of photodegradation in ambient conditions on the electrical performance of OSCs. The choice of solvent and additives used in OSCs is a crucial factor influencing both device performance and stability. Collectively, these findings provide insights to guide the design of next-generation donor and acceptor materials with superior photostability and strategies to mitigate photodegradation.

ISBN 978-91-7867-684-2 (print)

ISBN 978-91-7867-685-9 (pdf)

ISSN 1403-8099

DOCTORAL THESIS | Karlstad University Studies | 2026:19
